USING SIMPLE MODELS TO IMPROVE UNDERSTANDING OF THE INTERACTIONS BETWEEN COMPONENTS OF THE CLIMATE SYSTEM

A thesis submitted in partial fulfilment of the requirements for the
Degree of Doctor of Philosophy in Physics
at the University of Canterbury

by

ANNA HELENA SÖDERGREN

Department of Physics and Astronomy
College of Science
University of Canterbury

– April 2019 –

Big whirls have little whirls that feed on their velocity,
and little whirls have lesser whirls and so on to viscosity.

— Lewis Fry Richardson

The reasonable man adapts himself to the world; the unreasonable one persists in trying to adapt the world to himself. Therefore, all progress depends on the unreasonable man.

— George Bernard Shaw

ABSTRACT

In this work a hierarchy of simple models are used to gain further understanding of the interaction between atmospheric processes and components, and the impact these processes and components have on the climate system.

A one dimensional energy balance box model is often considered one of the simplest climate models. During this PhD an energy balance model (EBM) of higher complexity, with an atmospheric layer and a surface layer, and a latitudinal resolution of 1°, has been developed, to examine the effects of non-linear interactions between surface albedo, water vapor, cloud cover and cloud albedo (referred to as climate variables) on amplified warming of the polar regions. The EBM is set up so that it is possible to allow one or more climate variables to change with changing temperature or keep them at fixed values from a reference run. Furthermore a method, using a semi-empirical model, for simulating the evolution of the stratospheric ozone layer and its coupling to the climate system was implemented into an existing simple climate model, named Model for Assessment of Greenhouse-gas Induced Climate Change (MAGICC).

For an induced forcing, feedbacks from processes associated with climate variables in the climate system either amplify or damp the warming of the surface temperature. To investigate the non-linear effects feedbacks from surface albedo, water vapour and cloud cover have on the surface temperature the sum of the contributions to surface temperature changes due to any variable considered in isolation is compared to the surface temperature changes from coupled feedback simulations. Our simulations show that the sum of temperature changes is smaller than the temperature changes from coupled feedback simulations, for all simulations. This non-linearity is found to be

strongest when all three climate variables are allowed to interact. Surface albedo appears to be the strongest driver of this non-linear behavior, followed by water vapor and clouds. This is because increases in longwave radiation absorbed by the surface, related to increases in water vapor and clouds, and increases in surface absorbed shortwave radiation caused by a decrease in surface albedo, amplify each other. Furthermore, our results corroborate previous findings that while increases in cloud cover and water vapor, along with the greenhouse effect itself, warm the polar regions, water vapor also significantly warms equatorial regions, which reduces polar amplification. Changes in surface albedo drive large changes in absorption of incoming shortwave radiation, thereby enhancing surface warming. Unlike high latitudes, surface albedo change at low latitudes are more constrained. Interactions between surface albedo, water vapor and clouds drive larger increases in temperatures in the polar regions compared to low latitudes. This is in spite of the fact that, due to a forcing, cloud cover increases at high latitudes and decreases in low latitudes, and that water vapor significantly enhances warming at low latitudes.

The effects from reflectivity of clouds (cloud albedo) on the feedbacks from surface albedo, water vapor and cloud cover (referred to as climate variables), and the impact the interaction between these climate variables has on the surface temperature are also examined. Output from simulations with all possible combinations of climate variables (surface albedo, water vapour, cloud cover and cloud albedo) activated or prescribed with values from a reference run are examined. For a doubling of atmospheric concentration of carbon dioxide, the output from the simulations show that there is an increase in cloud albedo in the low and high latitudes due to an increase in cloud temperature (and therefore an increase in the fraction of water droplets compared to ice crystals), and a very small decrease in cloud albedo in mid latitudes due to a decrease in cloud temperature. Changes in surface albedo greatly affect surface and atmospheric temperatures in the high latitudes, and therefore

also cloud temperatures and cloud albedo. The cloud albedo in this EBM depends on atmospheric temperature and lapse rate, and therfore there is a large impact from cloud albedo on simulations where the surface albedo feedback is fixed with values from a reference simulation. Furthermore, CO_2-induced cloud albedo changes have the greatest effect on simulations where there is little or no interaction between surface albedo, water vapour and cloud cover, because the change in LW radiation emitted from the atmosphere to the surface is then small compared to the change in SW radiation reflected by clouds.

MAGICC is a simple climate model,however of higher complexity than the EBM developed in this PhD project. MAGICC, with the newly implemented stratospheric semi-empirical model, was used to investigate how anthropogenic emissions of greenhouse gases and ozone-depleting substances will continue to affect concentrations of ozone in the stratosphere through the 21^{st} century. While a range of estimates for when stratospheric ozone is expected to return to unperturbed levels is available in the literature, quantification of the spread in results is sparse. Here a first probabilistic study of latitudinally resolved years of return of stratospheric ozone to 1960 levels is presented. Results from the 180-member ensemble, simulated with this newly developed simple climate model, suggest that the spread in return years of ozone is largest around 40° N/S and in the southern high latitudes and decreases with increasing greenhouse gas emissions. The spread in projections of ozone is larger for higher greenhouse gas scenarios and is larger in the polar regions than in the mid-latitudes, while the spread in ozone radiative forcing is smallest in the polar regions.

Deputy Vice-Chancellor's Office
Postgraduate Office

UNIVERSITY OF CANTERBURY
Te Whare Wānanga o Waitaha
CHRISTCHURCH NEW ZEALAND

Co-authorship Form

This form is to accompany the submission of any thesis that contains research reported in co-authored work that has been published, accepted for publication, or submitted for publication. A copy of this form should be included for each co-authored work that is included in the thesis. Completed forms should be included at the front (after the thesis abstract) of each copy of the thesis submitted for examination and library deposit.

Please indicate the chapter/section/pages of this thesis that are extracted from co-authored work and provide details of the publication or submission from which the extract comes:

Chapter 4, An energy balance model exploration of the impacts of interactions between surface albedo, cloud cover and water vapour on polar amplification, published in Climate Dynamics, 2017 (Södergren et al., 2017).

Please detail the nature and extent (%) of contribution by the candidate:

I, Helena Södergren, was the lead author of this article; contribution 85%.

Certification by co-authors:

If there is more than one co-author then a single co-author can sign on behalf of all.

The undersigned certifies that:

- the above statement correctly reflects the nature and extent of the PhD candidate's contribution to this co-authored work;

- in cases where the candidate was the lead author of the co-authored work he or she wrote the text.

Name: ADRIAN MCDONALD Signature: [signature] Date: 22/12/2017

Deputy Vice-Chancellor's Office
Postgraduate Office

Co-authorship Form

This form is to accompany the submission of any thesis that contains research reported in co-authored work that has been published, accepted for publication, or submitted for publication. A copy of this form should be included for each co-authored work that is included in the thesis. Completed forms should be included at the front (after the thesis abstract) of each copy of the thesis submitted for examination and library deposit.

Please indicate the chapter/section/pages of this thesis that are extracted from co-authored work and provide details of the publication or submission from which the extract comes:

Chapter 6, A probabilistic study of the return of stratospheric ozone to 1960 levels, published in Climate Dynamics, 2017 (Södergren et al., 2016).

Please detail the nature and extent (%) of contribution by the candidate:

I, Helena Södergren, was the lead author of this article; contribution 70%.

Certification by co-authors:

If there is more than one co-author then a single co-author can sign on behalf of all.

The undersigned certifies that:

- the above statement correctly reflects the nature and extent of the PhD candidate's contribution to this co-authored work;
- in cases where the candidate was the lead author of the co-authored work he or she wrote the text.

Name:	Signature:	Date:
ADRIAN McDONALD	A. J. M	22/12/2017

ACKNOWLEDGMENT

Firstly, I would like to thank family: my son Isaak and my family on the other side of the Earth, especially my mum, my dad and my sister for being there and being supportive throughout this journey.

I would like to thank my supervisor team Adrian McDonald and Greg Bodeker for endless support, patience and advice. Thank you Adrian for your insights and for your inspiring, encouraging working environment. Thank you Greg for your inspiring ideas and for making me want to work with perfection. Thank both of you for encouraging me to do my very best. I want to thank the whole group at Bodeker scientific in Alexandra, but especially Stephanie Kremser, who has been fantastic support especially during my first PhD year. I want to thank Malte Meinshausen for letting me work with his magic code, and for hosting me for a week of work at University of Melbourne. I also would like to thank the Atmospheric Phyics group, for good laughs and support during my years there. The group of Physics and Astronomy at University of Canterbury and Bodeker Scientific in Alexandra for scholarship.

Thank you all my outdoorsy friends and horses for joining me in the amazing New Zealand nature. Thanks to the mountains and the oceans for giving balance to my life.

CONTENTS

LIST OF FIGURES

LIST OF TABLES

1

INTRODUCTION

1.1 MOTIVATION

The unifying theme for this thesis is the use of simple models, e.g. energy balance models (EBMs), simple climate models (SCMs) and semi-empirical models, to better understand the links between different components of the climate system with a view to improve the quality of climate change projections. Here it is shown how simple models can be useful in order to estimate the uncertainty ranges in stratospheric ozone projections, as well as understand the non-linear interactions between surface albedo, water vapour and clouds in the climate system.

Simulating how the global ozone layer will evolve under different greenhouse gas and ozone depleting substance emissions scenarios is of interest to a wide range of the Earth Sciences community and to policy-makers as ozone is a radiatively active gas whose changes in concentrations affect both surface UV radiation and surface climate. Ideally, chemistry-climate models (CCMs) would be used to generate a large ensemble of simulations for a number of emissions scenarios that would capture model uncertainties and variances arising from internal model variability. However, CCMs are extraordinarily computational expensive. Therefore, to date, it has not been possible to generate the large ensembles of projections of global ozone change required by the Earth Sciences community and policy-makers to adequately incorporate uncertainty in those projections into

projections of surface UV radiation and climate. During the first year of this PhD project, the first ever SCM with an interactive stratosphere, i.e. with a stratosphere that is coupled to the climate system, was developed. The aim was to emulate the behaviour of a set of AOGCMs, in order to investigate the spread in stratospheric ozone abundances during the 21st century.
The focus of this thesis shifted later towards the more simplified range of models, EBMs, in order to gain an improved understanding of the non-linear interactions between surface albedo, water vapour and clouds and their impacts on polar amplification. Climate feedback from polar surface ice have been studied for decades, however effects of feedback caused by water vapour and clouds on polar amplification have been relatively poorly examined. It is well known that clouds and water vapour play a critical role in the energy balance of the Earth's climate system. Water vapour affects the radiative balance of Earth through the greenhouse effect and clouds through the greenhouse effect and through reflection of sunlight. However, water vapour and clouds are some of the least well understood elements of the global climate system (Roads and Vallis, 1984; Held and Soden, 2000; Pierrehumbert, 2002). Clouds and their effects on the climate system have proven difficult both to observe and simulate, and continue to be the main cause of spread in climate sensitivity in climate models (Boucher et al., 2013). In particular the shortwave effects from clouds seem to cause large biases (Kay et al., 2014), and the intention with the EBM developed here, was to gain some understanding in how the shortwave radiation effects from clouds are altered by the interaction between surface albedo, water vapour and cloud cover in the atmosphere, and the impact shortwave radiative effects from clouds have on the climate system. It is well known that water vapour and lapse rate feedbacks are closely related, and in the EBM presented in this thesis a simple representation of the lapse rate is included.

1.2 THESIS OUTLINE

This thesis is broad in focus with the concept of using simple models to improve understanding of components of the climate system. However the project does clearly follow a track in terms of using simple models of different complexity. MAGICC is a relatively complex simple model, and once the implementation of the stratospheric module was finished, it was natural to take "one step back" and gain understanding of the core of all climate models: the energy balance of Earth, in terms of EBMs.

A summary of the current literature is presented in Chapters 2 and 3, along with explanation and description of physical processes relevant to the subject. Chapter 2 focuses on key process governing the climate system. The fundamentals and earlier published research of the energy balance of Earth and feedbacks from the key climate variables surface albedo, water vapour, clouds and stratospheric ozone are discussed. The concept of polar amplification and outcome from published research on the topic is presented. In Chapter 3 climate models with two different levels of complexity, EBMs and SCMs as used in this PhD project, are presented. Discussions of EBMs with surface albedo, water vapour and clouds, and a description of the simple climate model MAGICC is provided.

The research in this thesis is presented in Chapters 4, 5 and 6. In Chapter 4, the EBM that was developed during this PhD project is described in detail. The outcome of the work presented in Chapter 4 shows that the interactions between surface albedo, water vapour and cloud cover have non-linear effects on the surface temperature and are important for the strength of climate sensitivity and polar amplification. The work presented in Chapter 4 has been peer reviewed and accepted for publication in the scientific journal Climate Dynamics.

The biases introduced by uncertainties in shortwave radiation reflected by clouds is a well known issue in climate modelling. A natural step in developing the EBM presented in this thesis

was to implement albedo of clouds that changes with changing cloud temperature. The output from the extended version of the EBM is presented in Chapter 5, and is also aimed to be submitted to a scientific journal.

The simple climate model MAGICC is more complex than the EBM developed in this thesis. Stratospheric ozone abundances were statistically simulated within MAGICC with a method similar to the method used to simulate cloud cover and cloud temperatures in the EBM described in Chapters 4 and 5. The output is presented in Chapter 6. The work in Chapter 6 has been peer reviewed and published in Geophysical Research Letters, as Södergren et al. (2016).

Finally, Chapter 7 provides a summary of this PhD work, and suggestions of some future work.

2

THE CLIMATE SYSTEM OF EARTH

This chapter discusses key physics and fundamentals of the climate system of the Earth, related to the work presented in later chapters. Fundamentals of the energy balance of the Earth's climate system, and definitions about climate feedbacks and difficulties related to feedback notations and estimations are explained and discussed. Finally the of reasons why the surface warms faster in the polar regions compared to the rest of the globe are discussed, and a review of this phenomenon generally referred to as polar amplification is provided.

2.1 ENERGY BALANCE OF EARTH - SOME FUNDAMENTALS

The energy budget of Earth can be explained as a balance between radiative fluxes and transport of heat. Essentially all energy entering the Earth climate system comes from the sun. The incoming energy from the sun is mostly in the form of radiation in the visible, near-ultraviolet and near-infrared spectra, with fluxes approximately in the 0.2 μm to 3.0 μm range, from now on defined as shortwave (SW) radiation. Some of the incoming radiation is reflected off clouds, some of it is absorbed by components in the atmosphere, mainly by water vapour, and some of it passes through the atmosphere and down to the Earth's surface. Some of the SW radiation that reaches the Earth's surface is absorbed by the surface, and some of it is reflected back into the atmosphere. Some surface types on Earth reflect the incoming SW radiation better than others. The reflecting power

of a surface is often measured as the ratio of the reflected radiation from the surface to incident radiation upon it, called albedo (Latin "whiteness"). For example fresh snow is an efficient reflector of the incoming radiation and has an albedo of as much as 0.90 while bare soil that is an efficient absorber has an albedo of around 0.17.

Since the axis of the Earth is tilted, more SW radiation is absorbed by the surface per unit area per year in the equatorial region than in the polar regions. This equator/pole difference in SW radiation absorbed by the Earth give rise to a meridional temperature gradient, with significantly higher temperatures in the equatorial regions compared to the polar regions. The poleward increase in reflectivity of the Earth due to increasing cloud cover and snow/ice cover, and it's corresponding cooling effect on the surface, increases this meridional temperature gradient further (compared to what it would be like without e.g. polar ice-caps and cloud albedo that increase with increasing latitude). The imbalance in the energy distribution is the driver of the temperature gradient and the reason that meridional energy transport is required, to maintain the energy balance of the Earth. As a consequence of the equator to pole temperature gradient and the resulting imbalance in energy distribution winds and ocean currents carry energy poleward, with different processes (such as ice/snow covered surface, clouds or water vapour), within the climate system tending to increase or decrease the strength of the gradient. Generally the energy carried from equator to poles is defined as the net energy transport integrated across longitude-height sections. The meridional heat transport is further described in sections 3.1.1.

The radiation emitted from the surface and atmosphere of Earth is approximately in the 4.0 μm to 100 μm range of the emission spectrum, usually referred to as terrestrial infrared, or longwave (LW) radiation. At the top of the atmosphere (TOA), on a global scale, the SW radiation that is absorbed by Earth's atmosphere or surface is balanced by emitted, outgoing LW radiation. This is usually not the case on a regional or local scale

(see Fig. 2.1). Due to the tilt of the Earth and therefore the differences in SW radiation absorbed in the equatorial and polar regions, and the resulting meridional transport of heat, the incoming flux of SW radiation will be greater then the outgoing flux of LW radiation in the equatorial regions, while the opposite applies in the polar regions. Seen from the TOA, a basic energy budget for the total energy content Q for latitude zone ϕ of the Earth can be written as follows,

$$\frac{\partial Q_\phi}{\partial \phi} = RF_\phi^{TOA} - \frac{1}{2\pi a^2 cos(\phi)} \frac{\partial H}{\partial \phi} \tag{2.1}$$

where RF_ϕ^{TOA} is the net radiative energy balance, e.g. SW plus LW, with downward flux defined as positive, and a is the radius of Earth. The second term on the right-hand side of Eq. 2.1 represents the convergence of the heat transport. On a global scale $\frac{\partial H}{\partial \phi}$ is zero.

When the global mean flux of LW radiation emitted by Earth equals the global mean net flux of SW radiation absorbed by Earth, i.e. when RF_{TOA} on a global scale is zero, the climate system is said to be in radiative balance, or in an equilibrium state. If an external forcing, e.g. increased GHGs or solar variability, is applied to the climate system, this balance is perturbed and the system responds by altering the radiative fluxes. In a transient state the flux of outgoing LW radiation will no longer equal the net flux of incoming SW radiation. Once the climate system reaches a new equilibrium state, the global mean net flux at the TOA will again be zero. The radiative imbalance, usually at TOA or at the tropopause, has become a widely used measure of the state of the climate system. Current estimates suggest that Earth has a net energy imbalance of around 0.6 Wm^{-2} (Wild et al., 2015). This means that there is more SW radiation absorbed by the Earth than LW radiation emitted, which has a warming effect on the surface temperature. By analysing output from climate models, it can also provide estimates of the climate impact on individual climatic processes, natural or anthropogenic, and is sometimes referred to as radiative forcing (RF).

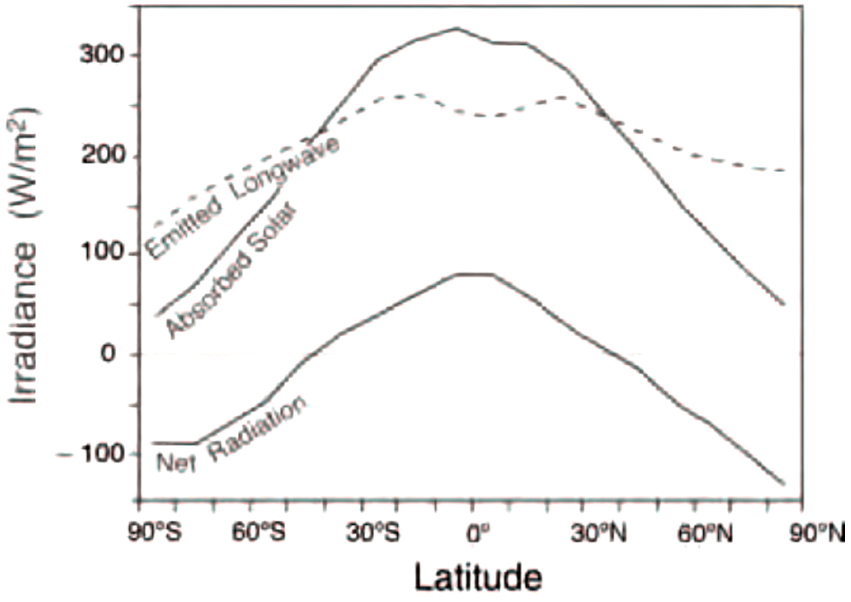

Figure 2.1: Longwave emitted and shortwave absorbed by Earth, as well as net radiative fluxes (longwave + shortwave). The figure is from source Marshall and Plumb (2007).

The energy balance of Earth depends not only on the amount of SW radiation from the sun reaching the TOA, but also on internal climate processes such as cloud amount, reflectivity of clouds and surface, and the abundances of GHGs, mainly carbon dioxide (CO_2), water vapour and also ozone in the atmosphere. The global mean radiative effect from stratospheric ozone on the surface temperature is relatively small. In the latest IPCC assessment report -0.05 [-0.15 to +0.05] Wm^{-2} is attributed to RF from stratospheric ozone (Myhre et al., 2013a). However, ozone is a radiatively active gas whose changes in concentrations affect both surface ultra-violet radiation and surface climate, and therefore simulating how the ozone layer will evolve under different GHG and ozone depleting substance (ODS) emissions scenarios is of interest to a wide range of the Earth Sciences community and to policy-makers.

The above discussion about perturbations of the radiative balance naturally leads us into the next section about climate feedbacks. The balance of stratospheric ozone abundances and the

effects of changes in stratospheric ozone on surface climate are discussed in Sec. 2.3.

2.2 CLIMATE FEEDBACKS - DEFINITIONS AND DISCUSSIONS

First a few notations about climate feedbacks, forcings and climate sensitivity: In general, a *feedback* is a process in which changing one quantity changes a second quantity, while the change in the second quantity changes the first. Most often a positive feedback is defined as a feedback that amplifies the effect from the change in the first quantity, while a negative feedback is defined as a feedback that reduces it. *Climate sensitivity* (CS) is a metric determined by a set of feedback mechanisms, that can be used for analysis of the climate system's temperature response to a perturbation, i.e. a *forcing*, F, externally imposed by e.g. GHGs, solar variability, etc. (Collins et al. (2013); Gregory and Webb (2007); Gregory et al. (2004)). It may be a bit confusing that the radiative response of the climate system to an external forcing, is sometimes referred to as *radiative forcing* (see Sec. 2.1). Radiative forcing is not really a forcing in that sense, but rather a response to a forcing. CS is usually defined as the change in surface temperature following a doubling of atmospheric CO_2 concentrations, after the climate system has readjusted to an equilibrium state. The concept of CS allows comparison of

- the sizes of temperature changes and
- strenghts of climate feedback responses

between models and due to different forcings. The difficulties in calculating CS are illustrated by the spread, ranging from 1.5 to 4.5°C, as reported in the latest IPCC report (Bindoff et al. (2013)). This range has not narrowed since the Charney Report (1979).

It has been shown that when an external forcing is applied to the climate system, there is a linear relation between the radiative response, or RF, at the TOA and the associated surface temperature change. A climate feedback parameter with respect to climatic variable i, λ_i, can then be defined as (Colman, 2003; Roe, 2009),

$$\lambda_i = \Delta RF_i^{TOA} / \Delta T_i^s \tag{2.2}$$

where ΔRF_i^{TOA} is the perturbation in the TOA radiative flux due to a change in climatic variable i, and ΔT_i^s is the corresponding change in surface temperature. The change in surface temperature, with all feedbacks considered in the climate system expressed as a sum, can be written as follows (Roe, 2009),

$$\Delta T^s = \frac{\Delta T_0^s}{1 - K \sum_i \lambda_i} \tag{2.3}$$

where

$$K = \left(\frac{RF_0^{TOA}}{\Delta T_0^s} \right)^{-1} \tag{2.4}$$

and where RF_0^{TOA} is the TOA radiative flux perturbation when all feedbacks are supressed, i.e. the perturbation associated with the Planck feedback, and ΔT_0^s is the corresponding response in surface temperature. Setting K to 0.3 KWm^{-2}, as stated in the work of Colman (2003), allows calculation of λ_i (Eq. 2.3).
Climate sensitivity and the climate feedback parameter can be calculated in different ways. Two of the most common methods are that climate sensitivity and λ are calculated according to Eq. 2.3 from an equilibrium state or from a transient state. Estimates of CS and λ obtained from equilibrium states are rare, since the GCMs, due to the long responding time scales in the deep ocean, needs to be run for hundreds to thousands of years to reach full equilibrium (Li (2012)). To get around the requirement of having to run the model to equilibrium, model output for evolving transient conditions are sometimes used to estimate CS. The climate response parameter is then determined by regressing $RF_i^{TOA}(t)$ against $T_i^s(t)$ where t is the timestep

from the initial perturbation (Gregory et al. (2004)). The slope is the effective climate response parameter, and the intercept with RF_i^{TOA} is F, i.e. the effect from the instantaneous forcing, before the climate system has responded. Then the net downward heat flux at the TOA, N, describing the rate of increase in heat stored in the climate system, can be written

$$N(t) = F - \lambda_i \Delta T_i^s(t) \tag{2.5}$$

In an equilibrium state $N = 0$ which means that the heat storage does not change.

Independent of the choice of method to simulate CO_2-induced changes in temperature after the climate system has readjusted to a new equilibrium state, estimation of λ is associated with difficulties and uncertainties. The climate feedback parameter, λ, depends on the time scales at which feedbacks respond to the forcing. Responses from clouds usually happen on very short timescales, which means that there will be a great change in temperature during the time of the readjustment of clouds. Other feedbacks, such as e.g. the surface albedo feedback, occur over thousands of years. Gregory et al. (2004) showed that in a simulation where a GCM is run to equilibrium, the temperature change slows down while approaching equilibrium state, when the ocean heat uptake is the major contributor to the change in temperature. The assumption that λ is linear is therefore probably not completely true on longer timescales (Gregory et al. (2004)). Also the climate sensitivity obtained from equilibrium states is unambiguous, since λ is likely to change with time. One reason why the linear approximation is still widely used is its simplicity, convenience and lack of alternatives (Knutti and Rugenstein (2015)).

Most climate models impose similar values of RF^{TOA}, which suggest that the spread in CS (i.e. ΔT^s for a doubling of CO_2) is associated with λ (see Eq. 2.3), especially with λ associated with clouds (Cess and Potter, 1991; Cess et al., 1996; Senior and Mitchell, 1993; Ho et al., 1998).

2.2.1 *Surface albedo feedbacks*

Ice and snow have high albedos compared to snow- and ice-free surfaces (Thackeray and Fletcher, 2016). This has a cooling effect on surface temperatures, by reflecting a significant part of the incoming SW solar radiation. Fluctuations in temperatures alter the surface albedo through gain or loss of snow and ice cover. A warming climate contributes to melting snow and ice cover, and thereby reveals a darker surface with lower albedo, i.e. a surface that reflects less and absorbs more SW radiation (Ingram, Wilson, and Mitchell, 1989; Cess and Potter, 1991; Thackeray and Fletcher, 2016). When atmospheric CO_2 concentration increases, the troposphere warms as it absorbs more upwelling terrestrial LW radiation. The downward LW component, i.e, the LW radiation that is emitted from the atmosphere down to the surface, warms the surface which further enhances melting of ice cover. This positive feedback is known as the surface albedo feedback. On a regional scale, especially in the Northern Hemisphere high latitudes, the surface albedo feedback is known to contribute significantly to increasing temperatures (Thackeray and Fletcher, 2016). Surface albedo feedback has long been suggested to be the feedback that contributes the most to a warming climate (Lian and Cess, 1977; Manabe and Stouffer, 1980). However later research has pointed towards the importance of other feedbacks, such as water vapour and clouds, and their impacts on temperature changes in the climate system (see e.g. Mitchell et al. (1989); Randall et al. (2007a)). Figure 2.2 (from Bony et al. (2006)) shows simulated feedback parameters, or climate feedback strengths, for water vapor, clouds, surface albedo and lapse rate, and demonstrates the importance of the coupling between feedbacks, and also that water vapor feedbacks contributes most to the surface warming, followed by clouds and surface albedo. It also shows the large spread among models, especially for the cloud feedback, that even shows different sign of feedback for different models.

2.2.2 *Water vapour feedbacks*

The effect water in the atmosphere has on the climate system depends on its phase, i.e. if it is in gas phase, liquid phase (as water droplets in liquid water clouds) or solid phase (in the form of ice crystals in clouds). On a molecule-to-molecule basis, water in liquid or solid form in the atmosphere are around 1000 times stronger absorbers of LW radiation compared to water in gaseous form (Stephens, 2005). However, water in gaseous form is the primary absorber of SW radiation in the atmosphere while both water in liquid form and solid form are poor absorbers but efficient reflectors of SW radiation. There are several factors other than the absorbing and reflecting effects that are relevant to the feedbacks of water in clouds, and they are discussed in Sec. 2.2.3 below. Observations and GCM outputs show that water vapour in the atmosphere, just like surface albedo, has a global net positive feedback effect on the climate (Bony et al., 2006; Soden and Held, 2006), and is considered the GHG with the greatest contribution to the greenhouse effect (Randall et al., 2007a), due to its strong feedback effects. Globally, water vapour is known to approximately double the warming effect from CO_2 (see Fig. 2.2).

The amount of water vapour is strongly dependent on the temperature in the atmosphere, through Clausius-Clapeyron's relation, which gives the rate of change of saturation vapour pressure with changing temperature (see e.g. O'Gorman and Muller (2010)). Column integrated water, also referred to as total column water vapour or precipitable water, is dominated by the lower troposphere, where the temperature is usually higher compared to the upper troposphere. Due to the low concentrations of water vapour in the upper troposphere compared to the lower troposphere, for a uniform warming, the relative change in water vapour is larger in the upper troposphere. Thereby the largest contribution to the LW water vapour feedback occurs in the upper troposphere, especially in the tropical regions. This has been suggested by GCMs (Schneider et al., 1999), observations (Randall et al., 2007a) and simple models

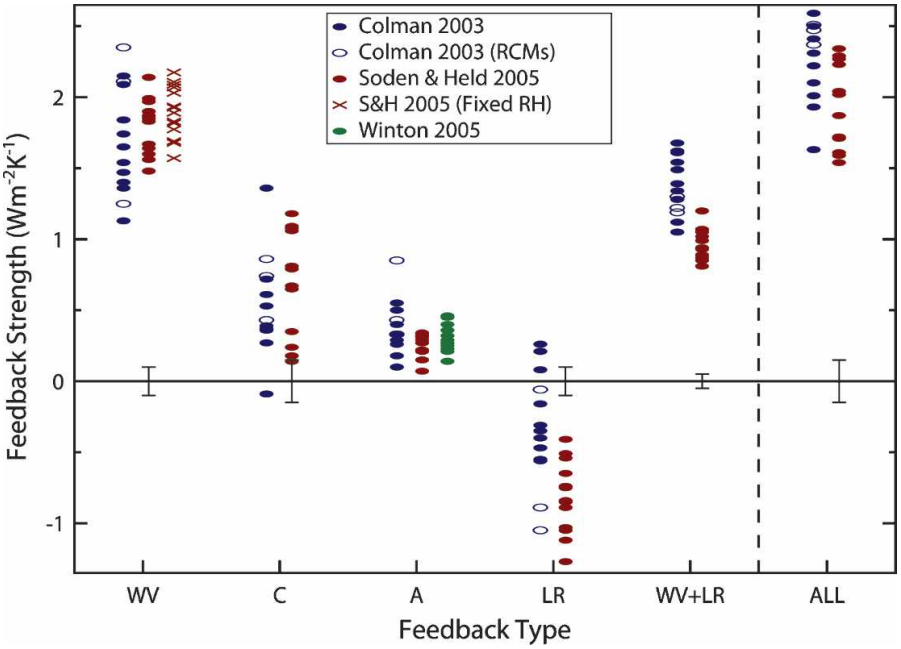

Figure 2.2: GCM climate feedback strengths for water vapour (WV), cloud (C), surface albedo (A), lapse rate (LR), the combined WV + LR and the sum of all feedbacks (ALL). The figure is from source Bony et al. (2006), and shows the results from Colman (2003); Soden and Held (2006); Winton (2006).

(Payne et al., 2015). Furthermore, enhanced warming in the tropical upper troposphere, due to changes in lapse rate has been found in GCM output. Since emission of LW radiation depends on the temperature, more LW radiation will escape to space, contributing to a cooling of the Earth (a negative feedback, see Fig. 2.2). A warmer upper troposphere further increases water vapour concentration (which contributes with a strong positive feedback), but it also partially offsets the radiative response from temperature increase by emitting more LW radiation out to space. Because of this strong link, the lapse rate and water vapour feedbacks are often considered together (Randall et al., 2007a), and so they are treated together in this work as well.

2.2.3 *Cloud feedbacks*

There is a consensus among GCMs and observations that water in gaseous form provides a positive feedback, i.e. amplifies the surface temperature warming induced by CO_2 forcing. The effects on the energy balance of Earth from water in other forms than gaseous in the atmosphere are more complex and difficult to understand. Water in the form of droplets or ice in clouds affect the radiation budget via a number of different properties, e.g. cloud amount, cloud height, vertical profile, optical depth, liquid and ice water content and sizes of particles. Changes in the albedo and absorption efficiency of clouds strongly affect both SW and LW radiation fluxes, and occur through changes in cloud optical depth, which in turn depends on thickness and/or changes in particle size, water and ice contents, liquid water content etc (Stephens, 2005). Whether clouds have a warming or cooling effect on the atmospheric temperatures depends on their vertical structure. High, cold clouds tend to warm the atmosphere relative to clear skies, especially at low latitudes, while low clouds seem to cool the atmosphere, especially in high latitudes (Slingo and Slingo, 1988).

Water in the form of droplets or ice crystals efficiently reflect SW radiation that is coming in from the sun, and thereby contribute to cooling of the climate system, i.e. a negative feedback. When viewing from the TOA, this reflective (cooling) effect from water in clouds, unlike water vapour, strongly offsets the absorbing (warming) effect. This offset of SW and LW processes, and the relatively small net effect on TOA radiative fluxes, does however not mean that the cloud feedback is negligible. Already in the 1970's changes in cloudiness was recognized as an important factor for surface temperature changes (e.g. Schneider (1972)). However, coupling between cloud feedbacks and the climate system is important. That cloud feedbacks are likely to have impacts on other feedbacks than just cloud-climate feedbacks has been suggested by e.g. Choi et al. (2014), as well as the outcome of this PhD project (see Chapter 4 and Södergren et al. (2016)). This implies that the way cloud

properties are parametrized and represented in climate models will affect the climate sensitivity of that model. Choi et al. (2014) showed that the relative roles of major climate feedbacks can be altered by cloud parametrization. They found that the smallest effect is on water vapour, and that surface albedo is greatly affected by altered cloud properties in the high latitudes. Lately, a major focus has been on the effect clouds have on the SW radiation, especially over the Southern Ocean (Kay et al. (2014, 2016)), which causes biases in radiative effects, and therefore CS, in climate models (Trenberth and Fasullo (2010)). These biases are believed to be related to the phase of water, and therefore the efficiency of reflecting or absorbing SW radiation, in clouds. Both models and observations suggest that supercooled water in clouds strongly influences cloud radiative effects (Kay et al. (2016); Forbes and Ahlgrimm (2014)). Kay et al. (2016) found that a too small amount of supercooled water in low-level clouds over the Southern Ocean causes excessive absorbed SW radiation in the Community Earth System Model (CESM), and that these biases are reduced when more supercooled water is included. Furthermore, cloud feedbacks act over a wide range of time and space scales, which adds complexity to the understanding and estimation of climate sensitivity in GCMs. The difficulties in simulating feedback from clouds is demonstrated by the wide range of output from GCMs, as shown in Fig. 2.2. A critical review of clouds and their feedbacks can be found in the review article of Stephens (2005).

2.3 STRATOSPHERIC OZONE ABUNDANCES AND RADIATIVE RESPONSES

Naturally, ozone is created and destroyed through a series of reactions involving oxygen. This cycle is known as the Chapman cycle:

1. **Creation of an ozone molecule**: An oxygen molecule is photolyzed by ultra-violet light, into two oxygen atoms:

$$O_2 + h\nu \rightarrow 2O\bullet \tag{2.6}$$

Each oxygen atom combines with an oxygen molecule to form an ozone molecule:

$$O\bullet + O_2 \rightarrow O_3 \tag{2.7}$$

2. **The ozone-oxygen cycle**: The ozone molecule created above absorbs ultra-violet light, and is split into an oxygen molecule and an oxygen atom:

$$O_3 + h\nu \rightarrow O_2 + O\bullet \tag{2.8}$$

Ozone is reformed when the oxygen atom quickly reacts with another oxygen molecule:

$$O\bullet + O_2 \rightarrow O_3 + M \tag{2.9}$$

where M is the excess energy of the reaction. The two reactions above constitute the ozone-oxygen cycle, which is a major source of heat in the atmosphere due to the release of kinetic energy (the other major source being the kinetic energy released when an oxygen molecule is photolyzed into two oxygen atoms).

3. **Removal of an ozone molecule**: If an ozone molecule and an oxygen atom collide, they will create two oxygen molecules:

$$O_3 + O\bullet \rightarrow 2O_2 \tag{2.10}$$

The abundances and distribution of stratospheric ozone are however affected both by dynamical and chemical mechanisms. Stratospheric ozone is created through photochemical processes, via the Chapman cycle and ozone-oxygen cycle as described above, but is also transported to the stratosphere through upwelling from the troposphere, especially in the tropics. Stratospheric ozone losses occur through chemical reactions via the

Chapman cycle and the ozone-oxygen cycle, but also through down-welling to the troposphere.
It is well established that man-made ODSs, in particular chlorine and bromine containing substances, whose concentrations peaked in the late 1990's, and now, thanks to the Montreal Protocol are declining (Yang et al. (2008); Carpenter et al. (2014)), are the main cause of the observed depletion of the stratospheric ozone layer. Due to their stability, human produced chlorofluorocarbons (CFCs), are able to travel from the surface up to the stratosphere, where they are bombarded with high-energy ultra-violet light from the sun. The CFC compound breaks down and releases chlorine atoms. A free chlorine atom easily react with an ozone molecule, takes one oxygen atom to form chlorine monoxide, and leaves an oxygen molecule,

$$Cl + O_3 \rightarrow ClO + O_2 \tag{2.11}$$

When the chlorine monoxide molecule collides with an oxygen atom, the oxygen atom from chlorine monoxide is transferred to the free oxygen atom, creating an oxygen molecule and leaves the chlorine atom free to destroy more ozone,

$$ClO + O\bullet \rightarrow Cl + O_2 \tag{2.12}$$

This reaction happens over and over again. The chlorine atom acts as a catalyst and is capable of destroying thousands of ozone molecules. Similar reactions involving oxygen occur for bromine, nitrogen and hydrogen (Jonsson (2004)).
Equivalent effective stratospheric chlorine (EESC) has become a useful metric to account for the factors that influence the fraction of active chlorine and bromine from the ODSs to destroy stratospheric ozone. EESC is the sum of the time-dependent chlorine and bromine derived from tropospheric abundances of ODSs, weighted to reflect their potential influence on stratospheric ozone (Meinshausen (2001); Carpenter et al. (2014)). The effectiveness of bromine is around sixty times that of chlorine (on a per-atom basis) for destroying stratospheric ozone. However, ODS are not the only factor that controls the anthropogenic fluctuations in ozone abundances. If the levels of

ODSs in the atmosphere was the only factor to affect stratospheric ozone levels, stratospheric ozone would be expected to return to pre-industrial levels with declining ODS burden, around 2040 in the tropical lower stratosphere, and likely not before 2100 in the upper stratosphere (Eyring et al. (2010a)). In this thesis pre-industrial levels are defined as those observed before 1960.
Changes in atmospheric GHG concentrations affect the stratospheric ozone both through changes in transport and through chemical reactions that alter the stratospheric temperatures. Increasing concentrations of GHGs alter the abundances of stratospheric ozone through decreases in stratospheric temperatures which in turn affect temperature dependent chemical reactions, e.g. slowing of the $O_3 + O\bullet \rightarrow O_2$ reaction (Eq. 2.10), through changes in hydrogen and nitrogen oxide chemistry (e.g. Prather et al. (1990); Jonsson (2004)). Thereby the stratospheric ozone levels are increased, especially in the upper stratosphere (Jonsson (2004); Eyring et al. (2010a)).

Climate models consistently project acceleration of the global mass circulation of tropospheric air through the troposphere, a circulation known as the Brewer-Dobson circulation (BDC) (Butchart (2014)), due to GHG-induced climate change. Within the BDC, tropospheric air rises into the stratosphere in the low latitudes, moves poleward and descends in the middle and high latitudes. BDC is a pathway of ozone, ozone precursors (nitrogen oxides, carbon monoxide and volatile organic compounds) and ODSs to the stratosphere, and also globally redistributes ozone produced primarily in the tropical upper stratosphere. GCMs projections suggest that, due to strengthening of the BDC with increasing GHG gases, ozone will not return to pre-industrial levels before 2100 (Eyring et al. (2010a)). However, in the midlatitudes the evoloution differs from that in the lowlatitudes, and a steady increase in stratospheric ozone throughout the 21^{st} century has been suggested by GCMs.

In this project we use EESC to represent the changes in ozone from ODSs and CO_2 as a proxy for stratospheric temperatures.

As ozone absorbs in the ultra-violet, visible and infrared parts of the spectrum it affects the radiative budget of the atmosphere through complicated interactions with incoming ultra-violet and visible SW radiation and emitted outgoing thermal infrared LW radiation.

Ozone depletion in the stratosphere, especially in the upper stratosphere, would increase the incoming SW radiation reaching the troposphere, increase the surface temperature and therefore also contribute to a more positive RF. However, RF from a decrease in stratospheric ozone is partly offset by a corresponding decrease in LW radiation emitted from stratospheric ozone towards the surface, contributing to a negative RF and a cooler surface. RF is strongly dependent on the vertical distribution of ozone. Changes in ozone in the upper stratosphere tend to have a larger impact on the SW component of the RF, while changes in ozone closer to the troposphere seem to have a larger impact on the LW component (Lacis et al. (1990); Hansen et al. (1997); Forster and Shine (1997)). The net RF from stratospheric ozone is small, only -0.05 [-0.15 to +0.05] Wm^{-2} according to the latest IPCC report (Myhre et al. (2013a)), as mentioned earlier.

2.4 POLAR AMPLIFICATION

Changes in surface temperatures due to an external forcing are spatially non-uniform due to local feedbacks related to amplified or damped radiative responses or changes in transport of heat or in circulation patterns. It has been reported that the warming over land in the higher latitudes is more than double the warming of the rest of the Earth (Manabe and Wetherald (1975); Manabe and Stouffer (1980); Serreze and Francis (2006); Bindoff et al. (2013)). This is referred to as polar amplification (PA): an effect where an increase in energy into the climate system has a stronger warming impact in the polar regions compared to other regions of the Earth, i.e. the poles are more sensitive to perturbations of the climate system compared to lower latitudes (see e.g. Manabe and Wetherald (1975);

Trenberth et al. (2007)). Polar amplification is a robust feature of externally forced climate model simulations (Manabe and Stouffer (1980); Rind (1987); Meehl et al. (2007a); Lu and Cai (2010); Cai and Tung (2012); Knutson et al. (2013)) and is considered an inherent characteristic of the climate system. For decades the major focus has been on the role of surface albedo feedback in temperature changes at high latitudes (Manabe and Wetherald (1975); Manabe and Stouffer (1980); Serreze and Francis (2006)). However, PA has also been found in simulations where the surface albedo has been suppressed, pointing towards the importance of other feedbacks in amplified warming of the higher latitudes (Alexeev and Jackson (2013); Graversen and Wang (2009)). Atmospheric feedbacks altering the LW radiation, such as changes in water vapour, often considered in combination with lapse rate changes (Randall et al. (2007a)), and clouds, are also believed to have important impacts on the surface temperature (Colman (2003); Holland and Bitz (2003); Winton (2006); Graversen and Wang (2009); Serreze and Barry (2011)). By locking, and thereby supressing, the surface albedo in a coupled climate model, Graversen and Wang (2009) found that water vapour and cloud cover changes lead to a greenhouse effect which is larger in the Arctic than at lower latitudes. Pithan and Mauritsen (2014) suggested that the largest contributions to Arctic amplification comes from temperature feedbacks. Analysing climate model simulations from the CMIP5 archive, they found that as the surface warms, more radiation is emitted back to space in low latitudes compared to the Arctic. They attribute this effect both to difference in changes in the vertical structure of the atmosphere (lapse rate feedback) in low and high latitudes, and a smaller increase in emitted black body radiation per unit warming in high latitudes, due to colder temperatures. Flannery (1984) was one of the first to show the importance of atmospheric heat transport on PA, using a latitudinally resolved EBM. Thereafter the contribution from heat transport on PA has been presented in a number of publications, including the work from Schneider et al. (1997); Alexeev et al. (2005); Cai (2005) and Alexeev and Jackson (2013).

Even though PA is expected in both hemispheres in the future, in recent time the Arctic has been warming faster compared to Antarctica. A temperature increase of 2.9° (since the beginning of the 20th century) over land north of 60°N was recently reported by Jeffries et al. (2015). The temperature trend over Antarctica is not as clear, and also more uncertain due to limited observations before 1950 and sparse coverage of measurements (Bindoff et al. (2013)). According to the CMIP5 coupled climate models output presented in IPCC AR5 WG1, the Arctic is expected to have warmed 4.2±1.6 K (compared to pre-industrial temperatures) by the years 2080-2100, when simulated under the RCP4.5 GHG emissions scenario (Collins et al. (2013)), while the expected warming in Antarctic during the same time period and under the same scenarios is 1.5±0.7 K. The warming in the tropical regions is expected to be 1.6±0.4 K.

Reasons for the slower warming in Antarctica have been suggested to be a weaker surface albedo feedback in Antarctica, efficient ocean heat uptake in Southern Ocean, Antarctic ozone depletion and differences in topography between the Arctic and the Antarctic regions (Salzmann (2017)). The mixed-layer depths in the Southern ocean exceeds several hundreds meters and are therefore capable of taking up large amounts of heat (Gille (2008)) that would otherwise stay in the atmosphere, in contrast to the Arctic Ocean which is in parts highly stratisfied. Furthermore, ozone depletion causes strong cooling in the lower stratosphere over Antarctica, especially in the austral spring, and this cooling acts to strengthen and shift the Southern Hemisphere tropospheric midlatitude jet, i.e. the band of strong westerly winds centred at around 50°S, poleward. It also drives an increase in the Southern Annular Mode (SAM) index, which corresponds to decreases in sea level pressure over high latitudes and increases over low midlatitudes. It has been observed that the warming of the Antarctic peninsula and the simultaneous cooling over the rest of the continental Antarctica during the austral summer are largely correlated with the positive trend in SAM, which indicates that ozone depletion has contrib-

uted to these trends (Arblaster et al. (2014)), showing a slower net warming over the Antarctic region compared to the Arctic. The surface height, or the topography, is expected to affect the transport of heat from the lower latitudes to the poles (Salzmann (2017)). The average surface height of Antarctica exceeds 2 km, and is expected to reduce the heat transport, and therefore the polar amplification. Furthermore, the high altitudes implies lower temperatures and therefore less melting of ice and snow.

Due to considerable costs of running climate models to their equilibrium, research on equilibrium climate responses to increased CO_2 concentrations is sparse. Li (2012) ran an AOGCM to equilibrium under an atmospheric CO_2 quadrupling. Their model reached equilibrium global mean surface temperature after 1200 years, while the deep ocean equilibriated within about 5000 years. When coupled to a deep ocean their model showed an equilibrium global mean temperature change of 10.8 K, and when coupled to a slab ocean model, the equilibrium global mean temperature was 0.3 K higher, 11.1 K. Furthermore, their model gave a strong warming of both the Northern and Southern polar regions, with local temperature changes as large as ~20 K (in both hemispheres). The warming in the Southern hemisphere high latitudes were however delayed, mainly due to the large uptake of heat in the Southern Ocean. In this PhD thesis we always run the model to an equilibrium and can therefore assume symmetric amplification in the polar regions.

3

CLIMATE MODELS

The climate models developed in these PhD projects have been used in work that have been published in scientific journals. The EBM used in this thesis is described in detail in chapters 4 and 5. MAGICC is not described in detail in the work that is published under Ref. Södergren et al. (2016) (on which Ch. 6 is based), and is therefore described in detail in this chapter. A broad description of the basics as well as a review of the development of the type of EBMs used in this thesis, i.e. EBMs with ice albedo, cloud and water vapour feedbacks, is provided. The content of this chapter is to complement the descriptions, broaden the understanding and provide a general background of the models presented in Chapters 4, 5 and 6.

3.1 ENERGY BALANCE MODELS - A REVIEW

That the main source of energy on Earth is the sun has been known for a long time. One of the earliest papers on the energy balance of Earth was probably the work by Fourier (1827), who concluded that Earth is much warmer than it would be if the only heat source was the incoming radiation from the sun. He suggested that the Earth's atmosphere was trapping heat, and prevented it from escaping out to space, acting as an insulator. His work may be considered the first formulation of the greenhouse effect. How Earth loses energy out to space was however not understood until the 20^{th} century, and the introduction of quantum theory and Planck's law. Based on the

notion that radiation comes in quanta, Planck could explain Stefan-Boltzmann's law, which states that

$$Q = \sigma T^4 \tag{3.1}$$

where Q is the energy emitted from a black body at temperature T, and σ is Stefan-Boltzmann constant (5.67×10^{-8}). Planck described the spectral density of electromagnetic radiation at wavelength ν, emitted by a black body with the following expression,

$$B_\nu(T) = \frac{2\pi h_p}{c^2} \frac{1}{\nu a^3 (exp(h_p/(kT\nu)) - 1)} \tag{3.2}$$

where c is the speed of light (3×10^8 ms^{-1}), k is Boltzmann's thermodynamic constant ($1.38 \times 10^{-23} m^2 s^{-2} K^{-2}$), h_p is Planck's constant ($6.62 \times 10^{-34} m^2 kg s^{-}1$), and T is the temperature of a black body. By integrating B_ν (which is the energy emitted per unit area and time over the wavelength interval $[\nu, \nu + d\nu]$) the black-body radiation law is obtained (see Fig. 3.1). Furthermore, Wien's law states that the black body radiation curve for different temperatures peaks at wavelengths inversely proportional to the temperature of the body (see Fig. 3.1),

$$\nu_{max} = \frac{b}{T} \tag{3.3}$$

where b is Wien's displacement constant (2.898×10^{-3} mK).

The first approach on determine Earth's energy balance may have been the work by Dines (1917). Dines (1917) concluded that the actual amount of energy recieved by Earth in a year must equal the amount lost, and that it must be possible to write down a set of linear equations desscribing the quantities involved. One of the simplest EBMs is a zero-dimensional box model, where the entire planet is given one temperature, T. The simple one-equation can be written

$$a^2 \pi s_0 (1 - \alpha) = 4a^2 \pi \sigma T^4 \tag{3.4}$$

where s_0 is the radiation flux coming in from the sun (1370 Wm^{-2}) averaged over time, a is Earth radius (6371 m) and

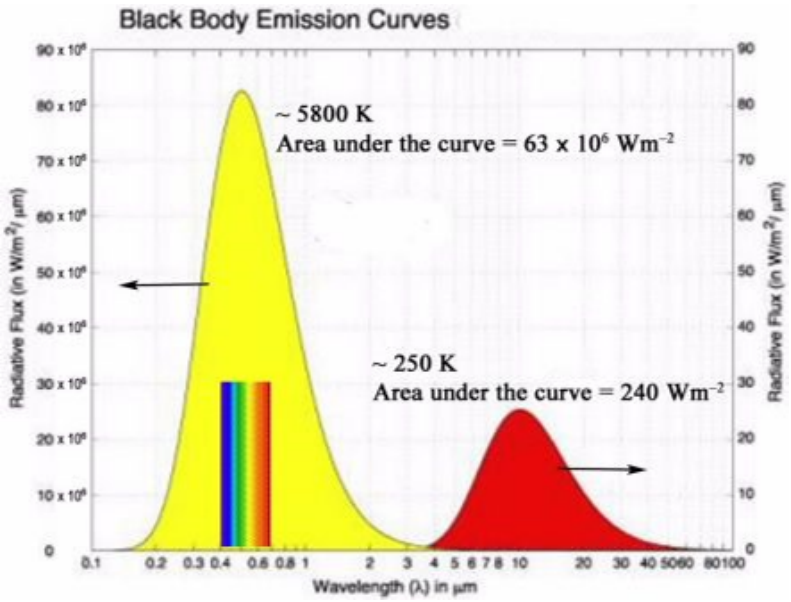

Figure 3.1: Black body curves for a black body with temperature similar to that of the sun, and to that of the Earth. The figure is from source Bell (2013).

α is the planetary albedo. On average, α is around 0.3, averaged over albedos of surface, clouds and atmosphere. This would give a T of around 255 K, which is much colder than the global average temperature of Earth. However, Earth is not a perfect black body. The atmosphere is not totally opaque, and emits temperature as a grey body rather than a perfect black body. This has to be taken into account when building a more realistic EBM. By adding an emissivity, ε, of 0.61 to our zero-dimensional model, so that our grey body emits radiation as $4a^2\pi\varepsilon\sigma T^4$, we obtain a temperature of 288 K, which is very close to the observed global surface temperature of Earth.

3.1.1 *Energy balance models and ice albedo*

EBMs can provide a useful tool to complement complex GCMs and have proven useful in understanding isolated processes in the climate system (Randall et al. (2007a)). In order to investig-

ate isolated processes in the climate system, more complicated EBMs than the zero-dimensional box model are often required. The simple one-dimensional EBMs developed by Budyko (1968) and Sellers (1969) in the late 1960's laid the ground for the use of dynamical EBMs in studies of changes in the climate system. The EBMs by Budyko (1968) and Sellers (1969) had latitudinal resolutions and a variable ice edge location, in order to study the sensitivity of ice albedo on the state of the climate system. Budyko and Sellers developed their EBMs independently, and even though the functional forms of the simple representation of the climate system differed between the two, they both predicted a high sensitivity to changes in the solar constant. Only a few percent decrease in the solar constant would expand the ice caps until the globe became completely covered in ice. This high sensitivity in temperature changes is associated with a bifurcation, often referred to as a "tipping point", where the Earth's climate becomes unstable and undergoes a shift to another climate equilibrium. In other words, it is a state where a very small perturbation within the climate system leads to large changes in temperatures. This new state of equilibrium of the climate system is known as the snowball Earth. Furthermore, EBMs have shown to be unstable for small ice caps (less than approximately 20 degrees in extent). An increase in temperature leading to further retreat of the ice caps results in the other extreme state of equilibrium - the totally ice-free Earth.

Furthermore, EBMs show non-linear behaviour in the sense that in a changing climate, it is faster for the climate of Earth to reach the tipping point for an ice-free state than a tipping point where ice-sheets start to develop. This means that the tipping point in a warming climate (i.e. going from Earth with the poles covered in ice to a complete ice-free Earth) occur at a cooler temperature compared to a tipping point in a cooling climate (going from a complete ice-free Earth to a state with ice covered poles).

It has later been argued if bifurcations related to changes in ice cover are realistic or if they are flaws often seen in EBMs

due to the discrete "jump"in albedos, from a low albedo for an ice-free surface to a high albedo for ice-covered surface. For example Wagner and Eisenman (2015) showed that the addition of variable sea-ice thickness added further non-linearities to their simple EBM that had a variable ice edge and that already showed non-linear behaviour due to the discrete jump in albedo. On the other hand, they also showed that by adding meridional heat transport and a seasonal cycle to their EBM, the stability of the ice cover was vastly increased. However, the stability also depends on the values of the parameters. Instability occurred in their model when the two parameters were reduced by at least a factor of 3. Rose and Marshall (2009) found additional bifurcations when using a more complex representation of energy transport in their EBM. In contrast to EBMs, bifurcations have been reported to be insignificant in GCMs (Armour et al. (2011)). GCMs include more feedbacks and processes compared to EBMs and simple models and therefore non-linearities are more pronounced. However Knutson et al. (2013) recently reported forced regional abrupt changes in the ocean, sea ice, snow cover, permafrost and terrestrial biosphere arising after a global temperature increase in a group of GCMs, although with little consistency among the models.

Since the pioneering work of Budyko (1968) and Sellers (1969), important contributions to the theory of EBMs include the work of e.g. Held and Suarez (1974), North (1975a,b), Flannery (1984) and Bendtsen (2002). A thorough review of the early literature of these classic EBMs was presented by North et al. (1981).

The heat transport in the EBM presented in this thesis is represented by a diffusive process directed down the mean temperature gradient, similar to the heat transport presented by Sellers (1969). The classic one-dimensional diffusive EBM can be expressed as a differential equation and is often written as follows (e.g. Rose and Marshall (2009)),

$$C\frac{\partial T}{\partial t} = D_\phi(CK\frac{\partial T}{\partial \phi}) + (1-\alpha)s - B_{out}T - A_{out} \tag{3.5}$$

where ϕ is the latitude zone, T is the surface temperature, α is the planetary albedo, C is the heat capacity for the atmospheric column, K is a large-scale diffusivity, $A_{out} + B_{out}T$ is the outgoing LW radiation and D_ϕ is an operator representing the meridional divergence, i.e.

$$D_\phi \propto \frac{d}{d\phi} \tag{3.6}$$

The parameters A and B in Eq. 3.5 are usually based on semi-empirical values. During this thesis a more complex two-dimensional EBM has been developed, with a latitudinal resolution of 1°, with an atmospheric and a surface layer, and with ice cover, water vapour concentration, cloud cover and cloud properties that depend on the state of the climate system. To be able to asses these three climate variables, viz. surface albedo, water vapour and clouds, independently, the radiative components of Eq. 3.5, i.e. $(1-\alpha)s + A_{out} + B_{out}T$, needs to be represented in more detail. The EBM developed in this thesis is presented in detail in Ch. 4, *v.i.*

3.1.2 *Energy balance models with water vapour and cloud feedbacks*

While the impacts from changes in surface albedo on surface temperature have been studied extensively, there have been fewer studies in which EBMs incorporate water vapour feedback. Due to the complexity of the processes involved in the formation of clouds, and the difficulties in their parametrization, there are also only a handful of EBMs that include cloud feedback. Here follows a brief overview of EBMs with water as vapour or in the form of clouds.

Van den Dool (1980) added a thin cloud cover to their simple EBM, which they used to study the influence of cloud amount of the earth's climate. They found that with reduced cloud amount, the sensitivity of the global mean temperature to changes in solar constant is increased because the snow- and ice feedback is active due to larger cloud-free areas. With an increase in cloud cover the model became less sensitive to changes in solar

constant. In their study they used prescribed cloud amount, i.e. dynamic feedbacks were not considered.
One of the first work on EBMs with explicit treatment of clouds was published by Roads and Vallis (1984). Their model was an extension of the Budyko-Sellers model, with water parameters calculated separately, and temperature feedbacks from water vapour not considered. However they included feedback clouds in their EBM, and found that cloud changes tend to be small, except in high latitudes where surface inversion effect causes an increase in cloud cover with increasing temperature. They found that the net global feedback by the cloud field is negative but small. Their simple EBM did not calculate vertical velocity explicitly, and the mechanisms were based on changes in adiabatic heating, surface evaporation and precipitation. They found that changes in lapse rate contribute the most to changes in cloud cover.
Jentch (1991) was one of the first to add a whole (simplified) hydrological cycle into an EBM with variable ice edge. In their two-layered ocean and atmosphere EBM, surface humidity was added as a function of temperature. They included evaporation at the surface layer, advection of water vapour, condensation into clouds and precipitation in their EBM. Thereby they incorporated both water vapour and cloud feedbacks in their EBM. They also included some structure of the atmospheric circulation, by differentiating between the dynamics of a low latitude zone and that of a high latitude zone. It was found that cloud albedo is the most sensitive radiation parameter, and that their EBM is relatively little affected by parameters associated with horizontal and vertical transport of heat.
More recently, Payne et al. (2015) showed with a conceptual model that the water vapour feedback is stronger in the low latitudes than in the polar regions, and therefore masks the amplifying effect in the polar regions. They also isolated the lapse rate feedback and showed its latitude dependence. For an increased GHG forcing, the lapse rate increases in the high latitudes, lead to a positive feedback, while decreasing in the low latitudes, lead to a negative feedback. They stress that the inclusion of cloud feedback in their idealized model would likely

alter their results.
Bates (2016) explored the climate sensitivity using a simple two-zone EBM, with a very simple parametrization of heat transport. They suggest that a two-zone EBM should be considered in effective climate sensitivity calculations, rather than a zero-dimensional box EBM. They report that meridional heat transport and varying radiative response can strongly influence climate sensitivity estimates. The model presented by Bates (2016) lack diffusive heat transport as well as representation of clouds.

3.2 THE SIMPLE CLIMATE MODEL MAGICC

Originally, SCMs were developed as climate models in their own rights, however lately the use of SCMs as fast emulators of more complex models based on a set of parameters describing the climate system has increased. SCMs can be very useful to complete simulations for a wide range of emissions scenarios or parameter settings, in order to estimate e.g. uncertainty ranges.

3.2.1 *MAGICC- model description*

One of the aims of this PhD project was to incorporate an interactive stratospheric ozone module into the existing Model for the Assessment of Greenhouse-Gas Induced Climate Change (MAGICC). In this section a brief description of MAGICC is provided. Figure 3.2 provides an overview of the key steps within MAGICC. These key steps are input in form of emissions, calculation of atmospheric concentration, calculation of RF and climate response to the forcing.

MAGICC is a SCM where an up-welling-diffusion ocean model is coupled to an atmospheric layer and a carbon cycle model (Hulme et al. (1995); Meinshausen et al. (2011b,a)). MAGICC evolved from the pure-diffusion ocean model introduced by Hoffert et al. (1980) and was originally developed by Wigley and Raper in the late 1980's (Wigley and Raper (1987, 1992)),

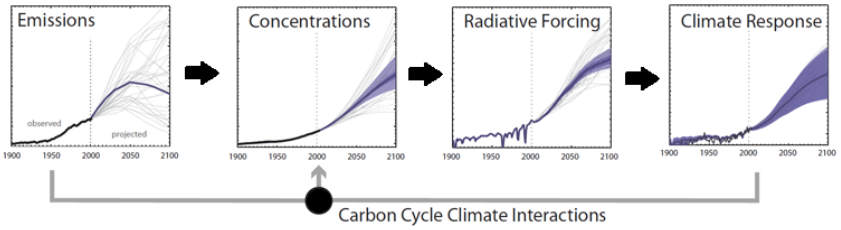

Figure 3.2: Schematic overview of the key steps in MAGICC, from emissions to concentrations to radiative responses and finally to climate responses. The figure is from source Meinshausen et al. (2011b).

and has been developed and updated continuously since then (see for example Refs. Raper (1996); Wigley and Raper (2001); Wigley et al. (2009)). The global energy balance equation in MAGICC, for a perturbed climate system, can be expressed as

$$\Delta Q_G = \lambda_G \Delta T_G + \frac{dF^o}{dt} \tag{3.7}$$

where ΔQ_G is the global mean RF at the troposphere, $\frac{dF^o}{dt}$ is the change in outgoing energy flux and heat content in the ocean, λ_G is the global-mean feedback factor and ΔT_G is the global mean surface temperature perturbation.

MAGICC was first developed as a one-box model, but is now a four-box model with the globe divided into land and ocean 'boxes' in the northern and southern hemispheres, in order to account for different thermal inertias and climate sensitivities over land and ocean, and over Northern and Southern hemispheres. The upwelling-diffusion ocean module within MAGICC has 40 layers with inter-hemisphere heat exchange in the mixed layer for both hemispheres (see Fig. 3.3).

MAGICC includes a series of gas-cycle models for GHGs such as CO_2, CH_4 and N_2O as well as halocarbons and chloroflourocarbons (CFCs), to be able to run different emissions scenarios. The terrestrial carbon cycle in MAGICC is a global box model, similar to the one in the work published by Harvey (1989) and Wigley (1993). In the carbon-cycle module within MAGICC, changes in atmospheric CO_2 concentrations are determined by

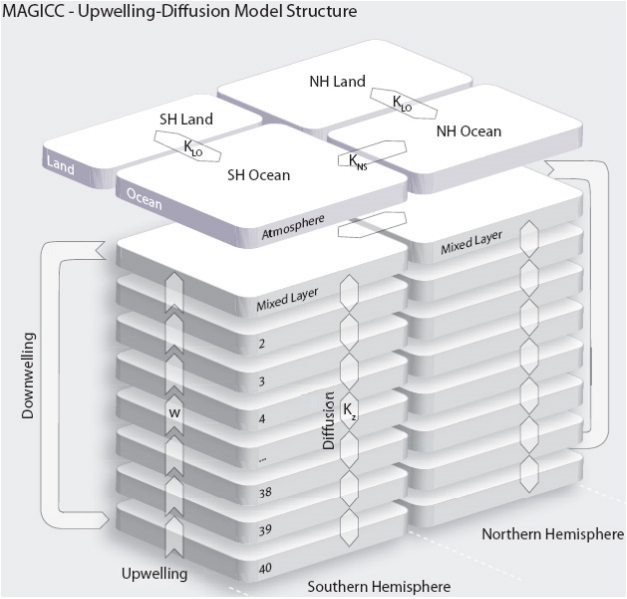

Figure 3.3: Structure of MAGICC's upwelling-diffusion energy balance module with land and ocean boxes in the Northern and the Southern hemispheres. The figure is from source Meinshausen et al. (2011b).

CO_2 emissions from fossil and industrial sources, other directly human-induced CO_2 emissions or removals to the terrestrial biosphere, contribution from oxidized methane of fossil fuel origin, flux due to ocean carbon uptake, net carbon uptake or release by the terrestrial biosphere due to CO_2 fertilization. The carbon-cycle module has three boxes (see Fig. 3.4), a living plant box, and two dead biomass boxes- one detritus and one for organic matter in soil. For details see Ref. Meinshausen et al. (2011b).

3.2.2 *Radiative forcing in MAGICC*

The radiative forcing in MAGICC is the radiative imbalance at tropopause level after stratospheric temperatures have adjusted. The RF from CO_2 in MAGICC is represented by the following expression, first presented by Shine et al. (1990),

$$\Delta Q_{CO_2} = \alpha_{CO_2} \ln \frac{C}{C_0} \tag{3.8}$$

where ΔQ_{CO_2} is the RF by CO_2 for a CO_2 concentration C above the initial C_0 concentration (set to 278 ppm). The scaling parameter α_{CO_2} is currently set to 5.35 Wm^{-2} ($= \frac{3.71}{\ln(2)}$ Wm^{-2}) (see Ref. Myhre et al. (1998)). However α_{CO_2} can also be calculated as follows, for a specific AOGCM,

$$\alpha_{CO_2} = \frac{\Delta Q_{2x}}{\ln(2)} \tag{3.9}$$

where ΔQ_{2x} is the radiative perturbation for a doubling of CO_2 for that particular AOGCM. Before the implementation of the new stratospheric module in MAGICC (i.e. the module that was developed during this PhD project), the RF from stratospheric ozone depended solely on EESC concentrations, and was expressed as

$$\Delta Q_{SCO} = \eta_1 (\eta_2 \times \Delta EESC)^{\eta_3} \tag{3.10}$$

where η_1 is a sensitivity scaling factor (set to -4.49×10^{-4} Wm^{-2}), η_2 is set to $\frac{1}{100}$ ppb^{-1}, η_3 is the sensitivity exponent (1.7), $\Delta EESC$

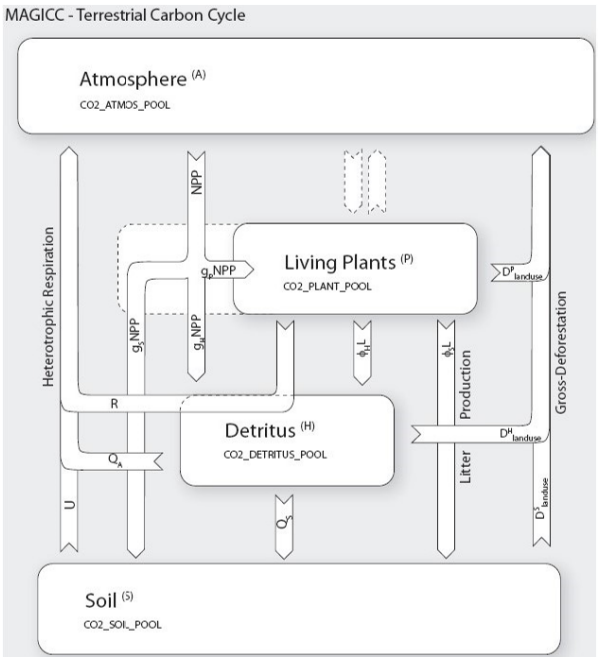

Figure 3.4: The terrestrial carbon cycle components in MAGICC. GPP is the gross primary product, NPP is the net primary product, g is the partitioning, Q_A is the non-land use related oxidation, $\phi_H L$ is the litter production, D^H_{lu} is sink due to land use, Q_S is sink to the soil, D^P_{gross} is gross deforestation. For details see the source of the figure in Ref. Meinshausen et al. (2011b).

is the change in EESC concentrations relative pre-industrial levels. EESC concentrations are calculated from the modelled concentrations of a number of Montreal Protocol controlled ODSs, within MAGICC. Their respective chlorine and bromine atoms, fractional release factors as well as bromine versus chlorine ozone depleting efficiency are taken into account (Daniel et al. (1999)). The newly implemented stratospheric ozone module within MAGICC is described in detail in Ch. 6 below, *v.i.*

In MAGICC the overlapping bands of methane and nitrous oxide are taken into account in the RF calculations, so that higher concentrations of one gas reduces the absorption of the other gas and vice versa. In this thesis the focus is not on methane, nitrous oxide, tropospheric ozone, tropospheric aerosol or halogenated gases, also taken into account in MAGICC, and the reader is referred to Ref. Meinshausen et al. (2011b) for more details.

In MAGICC there are different feedback parameters λ over land and ocean. At equilibrium the heat uptake of the ocean is zero, and Eq. 3.7 can be written

$$\Delta Q_G = \lambda_G \Delta T_G = f_L \lambda_L \Delta T_L + f_O \lambda_O \Delta T_O \tag{3.11}$$

where ΔQ_G, λ_G and ΔT_G are the global mean RF, feedback factor and temperature changes, f_L and f_O are the area fractions for land (L) and ocean (O), λ_L and λ_O are the climate feedback factors for land and ocean and ΔT_L and ΔT_O are the temperature changes for land and ocean. Equation 3.11 is further partitioned into Northern and Southern hemispheres. The following expression represents the Northern hemisphere ocean,

$$\begin{aligned} f_{NO} \lambda_O \Delta T_{NO} = f_{NO} \Delta Q_{NO} + k_{LO} (\Delta T_{NL} - \mu \Delta T_{NO}) \\ + k_{NS} \alpha (\Delta T_{SO} - \Delta T_{NO}) \end{aligned} \tag{3.12}$$

where the term on the left-hand side of Eq. 3.12 is the outgoing LW radiation, the first term on the right-hand side of Eq. 3.12 is the RF, the second term represents the land-ocean heat exchange and the last term is the hemispheric heat exchange. The

land-ocean heat exchange coefficient is represented by k_{LO}, μ is a factor that allows asymmetric land-ocean heat exchange, k_{NS} is the hemispheric heat exchange coefficient in the mixed layer and α is a sea-ice related adjustment factor that relates upper ocean temperature change to surface air temperature change. The corresponding equations for Southern hemisphere ocean, Northern hemisphere land and Southern hemisphere land are also included in MAGICC but not shown here. The reader is referred to Ref. Meinshausen et al. (2011b) for further details.

3.2.3 *Calibration of MAGICC- a brief overview*

Currently MAGICC is tuned to 19 of the 23 AOGCMs that was included in The World Climate Research Programmes (WCRPs) Coupled Model Intercomparison Project phase 3 (CMIP3) and 10 of the 11 different carbon cycle models included in the Coupled Climate Carbon Cycle Model Intercomparison Project C^4MIP Friedlingstein et al. (2006). The calibration of MAGICC is outside the scope of this thesis and the reader is referred to Ref. Meinshausen et al. (2011b) for a more detailed description.

Output from MAGICC is used in the optimization procedure, and fitted to agree with AOGCMs. The fitted output include global mean surface temperature change, global mean heat uptake, global mean RF, climate sensitivity and land/ocean warming. The AOGCM parameters used in the calibration are the climate sensitivity parameter, land-ocean warming ratio at equilibrium, the vertical diffusitivity in ocean (has a large influence on the ocean heat uptake efficiency), sensitivity of feedback factors (see Appendix A4.3 in Ref. Meinshausen et al. (2011b)), sensitivity of vertical diffusivity at mixed layer boundary to global-mean surface temperatures (*i.e.* thermal stratification)) (see Appendix A4.7 in Ref. Meinshausen et al. (2011b)), heat exchange between the hemispheres, land-ocean heat exchange coefficient ($Wm^{-2}K^{-1}$), see Eq. A50 in Ref. Meinshausen et al. (2011b) and amplification factor for the ocean to land heat exhange (time-dependent, allows the emulation of increasing ef-

fective sensitivities under global warming) (see Appendix A4.2 in Ref. Meinshausen et al. (2011b)).

Furthermore, another set of parameters in MAGICC are tuned to fit the output from MAGICC with output from from C^4MIP carbon cycle models. The output that is used in the tuning include terrestrial carbon uptake, oceanic carbon uptake, gross primary production, terrestrial living plant carbon pool, terrestrial dead plant carbon pool, total respiration and CO_2 concentrations.

The optimized parameters in the MAGICC calibration of the ocean carbon cycle were CO_2 gas exchange rate between the atmosphere and the upper mixed ocean layer (see Eq. A22 in Ref. Meinshausen et al. (2011b)), temperature sensitivity to the sea surface partial pressure (see Eq. A27 in Ref. Meinshausen et al. (2011b)) and a scaling factor to scale the impulse response function for the inorganic carbon perturbation in the mixed layer.

Calibrated terrestrial carbon cycle model parameters that determine the flux partitioning within MAGICC include the fraction of the plant box flux going to the detritus box, the fraction of the detritus box outbound flux going to the soil box, three different fertilization parameters and temperature feedback parameters of the heterotrophic respiration (see Fig. A2 in Ref. Meinshausen et al. (2011b)).

3.3 LIMITATIONS IN SIMPLE CLIMATE MODELS

A simple model provides a conceptual picture of the climate system, and assuming that one wisely chooses parameters that describe the processes involved, it may be a useful complement to more complex models. With a simple model a broad range of parametrizations can be investigated and contribute to a more complete understanding of possible system behaviour. However it is important to be aware that some of their limitations lie in the lack of some processes and feedbacks, or in the lack of

details in processes and feedbacks. Typically an EBM or SCM does not attempt to resolve the dynamics of the climate system, for example winds, atmospheric or oceanic circulations or convective motions in the atmosphere and ocean. The vertical profile of the atmosphere in an EBM or SCM is usually considered rigid, not allowing variations in lapse rate for example.

4

AN ENERGY BALANCE MODEL EXPLORATION OF THE IMPACTS OF INTERACTIONS BETWEEN SURFACE ALBEDO, CLOUD COVER AND WATER VAPOUR ON POLAR AMPLIFICATION

4.1 ABSTRACT

We examine the effects of non-linear interactions between surface albedo, water vapor and cloud cover (referred to as climate variables) on amplified warming of the polar regions, using a new energy balance model (EBM). Our simulations show that the sum of the contributions to surface temperature changes due to any variable considered in isolation is smaller than the temperature changes from coupled feedback simulations. This non-linearity is strongest when all three climate variables are allowed to interact. Surface albedo appears to be the strongest driver of this non-linear behaviour, followed by water vapor and clouds. This is because increases in longwave radiation absorbed by the surface, related to increases in water vapor and clouds, and increases in surface absorbed shortwave radiation caused by a decrease in surface albedo, amplify each other. Furthermore, our results corroborate previous findings that while increases in cloud cover and water vapor, along with the greenhouse effect itself, warm the polar regions, water vapor also significantly warms equatorial regions, which reduces polar amplification. Changes in surface albedo drive large changes in absorption of incoming shortwave radiation, thereby enhancing

surface warming. Unlike high latitudes, surface albedo change at low latitudes are more constrained, due to lack of retreat/ expansion of ice sheets. Interactions between surface albedo, water vapor and clouds drive larger increases in temperatures in the polar regions compared to low latitudes since the amplification of the longwave radiation emitted from the atmosphere down to the surface is larger in the high latitudes. This is in spite of the fact that, due to a forcing, cloud cover increases at high latitudes and decreases in low latitudes, and that water vapor significantly enhances warming at low latitudes. Changes in cloud cover depend on changes in lapse rate. Our simulations show that there is a decrease in lapse rate in lower latitudes, due to a strong increase in surface temperature, and this leads to a decrease in cloud cover in lower latitudes. Also the warm air in the tropics holds more water vapor, and therefore there is a greater increase in water vapor in the low latitudes.

4.2 INTRODUCTION

The surface air temperature response to greenhouse gas (GHG) induced radiative forcing of the climate system is larger in the polar regions than elsewhere. This is generally referred to as polar amplification (PA) (see e.g. Manabe and Wetherald (1975) and Trenberth et al. (2007)). The observed warming over land north of 65 °N has been reported to be more than double the warming of the rest of the globe over the last century (Trenberth et al., 2007; Bindoff et al., 2013). Polar amplification is also apparent in all climate model simulations from the World Climate Research Programme Coupled Model Intercomparison Project phases 3 (CMIP3) and 5 (CMIP5), although the magnitude of the warming differs between models (Meehl et al., 2007a; Knutson, Zeng, and Wittenberg, 2013). In CMIP5 projections of 21st century climate change, PA is stronger in the Arctic compared to the Antarctic, while equilibrium response simulations display strong PA in both hemispheres (Collins et al., 2013). The warming over Antarctica has been weaker, but also more uncertain due to limited observations before 1950 and sparse cover-

age of measurements (Bindoff et al., 2013). The lack of transient amplified warming response in high southern hemisphere latitudes has been associated with for example deep ocean mixing, ocean heat uptake, a vast ice sheet and high altitude due to the topography. Research on equilibrium climate responses to increased carbon dioxide (CO_2) concentrations is sparse because of the considerable cost of running climate models to their equilibrium state. Li (2012) presented results from an atmosphere ocean general circulation model (AOGCM) simulation that showed strong warming of the polar regions, with local temperature changes as large as 20 °C for a quadrupling of CO_2.

Changes in surface albedo, and its role in the amplified climate response at the poles, have received much attention over the past few decades. Ice and snow have high albedos compared to snow- and ice-free surfaces (Thackeray and Fletcher, 2016). This has a cooling effect on surface temperatures, since these surfaces reflect a significant fraction of the incoming shortwave (SW) solar radiation. When atmospheric CO_2 concentration increases, the troposphere warms as it absorbs more upwelling terrestrial longwave (LW) radiation. The downward component of the infrared radiation emitted by the warmer troposphere then warms the surface which enhances melting of ice cover. In the energy balance model (EBM) presented in this work the melting of ice cover is represented by decreasing surface albedo. Reduced surface albedo in turn increases the SW radiation absorbed and further warming of the surface. While this positive surface albedo feedback is known to be a significant contributor to PA, the effects that other climate feedbacks have on PA is still a matter of debate (Randall et al., 2007a; Manabe and Wetherald, 1975; Manabe and Stouffer, 1980; Colman, 2003; Winton, 2006; Graversen and Wang, 2009; Screen and Simmonds, 2010; Crook and Foster, 2014). Feedbacks associated with LW radiation, such as changes in water vapor, often considered in combination with lapse rate changes (Randall et al., 2007b), and clouds, are also believed to have important impacts on the surface temperature (Colman, 2003; Winton, 2006). Graversen and

Wang (2009) also suggested that water vapor and cloud cover changes lead to a greenhouse effect which is larger in the Arctic than at lower latitudes.

Projections of temperature changes associated with anthropogenic climate forcings require models with a high level of detail, in the form of multiple interacting processes, resolved at high spatial and temporal resolution. This complexity makes it difficult to unravel cause and effect linkages or to isolate effects of single feedbacks. Energy balance models (EBMs) can provide a useful tool to complement complex General Circulation Models (GCMs) and have proven to be useful in understanding isolated processes in the climate system (Randall et al., 2007b). EBMs have also been widely used to investigate the ice albedo feedback (Flannery, 1984; North, 1975a; Bendtsen, 2002; Rose and Marshall, 2009) building on the pioneering work of Budyko (1968) and Sellers (1969). There have been fewer studies in which EBMs incorporate a hydrological cycle (Vallis, 1982; Jentch, 1991). Due to the complexity of the processes involved in the formation of clouds, and the difficulties in their parametrization, there are also only a handful of EBMs that include cloud feedbacks (Weare and Snell, 1974; Sellers, 1976; Vallis, 1982; Roads and Vallis, 1984; Jentch, 1991; Paltridge et al., 2007). Observations and GCM outputs show that water vapor in the atmosphere has a global net positive feedback effect on the climate (Bony et al., 2006; Soden and Held, 2006), and is considered the GHG with the greatest contribution to the greenhouse effect (Randall et al., 2007b). The largest contribution to the water vapor feedback occurs in the tropical upper troposphere. This has been suggested by GCMs (Schneider et al., 1999), observations (Randall et al., 2007b) and simple models (Payne et al., 2015). Payne et al. (2015) used a conceptual model to show that the water vapor feedback is stronger over lower latitudes than in the polar regions, and therefore masks the polar amplification effect. They also isolated the lapse rate feedback and showed its latitude dependence. For an increased GHG forcing, the lapse rate increases in the high latitudes, leading to a positive feedback, while decreasing in the low latitudes,

leading to a negative feedback. These effects have also been observed in GCM output (Pithan and Mauritsen, 2014; Graversen and Wang, 2009).

Clouds have a cooling effect on the surface by enhancing the planetary albedo and thereby reducing the incoming SW radiation reaching the surface, but also contribute to a warming of the surface by absorbing and re-radiating LW radiation. It is uncertain if clouds have a net cooling or net warming effect on Earth (Myhre et al., 2013b) because there are difficulties in taking account of clouds in observations and simulations (Stubenrauch et al., 2013). The fifth Intergovernmental Panel on Climate Change assessment report also stated that the main cause of the spread in GCM-modelled climate sensitivities is cloud feedbacks (Flato et al., 2013). The importance of cloud feedbacks on PA was shown by Vavrus (2004), who analyzed GCM runs with and without changes in three-dimensional cloud fraction, and suggested that changes in clouds account for one third of the global warming signal, and 40% of the warming in the Antarctic. Shell et al. (2008) found that water vapor, temperature and surface albedo changes contribute significantly to cloud radiative forcing which was used as a diagnostic of cloud feedback strength. The importance of the effect of lapse rate on cloud feedback was identified in the early 1980s from an EBM analysis detailed in Roads and Vallis (1984).

One of the advantages of a simple EBM is that it is relatively straightforward to add or remove feedbacks by letting parameters, such as surface albedo, vary or static at prescribed values. This allows their impacts on the climate system to be isolated in a simple modelling framework. Here we present a newly developed EBM that is used to investigate the non-linear interactions between surface albedo (α_s), water vapor (WV) and cloud cover fraction (f^c) feedbacks, and the effect these feedbacks have on changes in temperatures and PA.

4.3 THE MODEL

Our EBM has a surface level (averaged over ocean covered surface and land covered surface) with an overlying atmospheric layer. The nominal level associated with this atmospheric layer is at 650 hPa. The EBM is resolved latitudinally at a resolution of 1°, and averaged over the hemispheres. The EBM includes transport of heat across latitudes and a simple radiation scheme that takes into account the feedbacks from surface albedo, water vapor concentration, and cloud cover fraction. Following the work of Jentch (1991), the meridional transport of heat in the atmosphere is split into a diffusive term, representing the poleward transport of heat caused by turbulent eddy flow, and an advection term, to account for the equatorward flow of heat within the Hadley cell. The meridional transport of heat at the surface is approximated by eddy diffusion. The core of the EBM developed and presented here is based on the formulations of Budyko (1968); Sellers (1969); Held and Suarez (1974); Rose and Marshall (2009).

The time evolution of the atmospheric temperature T^a and surface temperature T^s are calculated by solving the following coupled differential equations, for each latitude Φ (see e.g. Rose and Marshall (2009)) (see Table 4.1 for a list of variables simulated within the model),

$$C^a \frac{\partial T^a}{\partial t} = -\frac{1}{2\pi r^2}\frac{\partial H^a}{\partial \phi} + SW^a + LW^a + F^l + F^s \tag{4.1a}$$

$$C^s \frac{\partial T^s}{\partial t} = -\frac{1}{2\pi r^2}\frac{\partial H^s}{\partial \phi} + SW^s + LW^s - F^l - F^s \tag{4.1b}$$

where the superscripts a and s refer to the atmosphere and surface respectively, and r is the radius of Earth (see list of parameter values in Table 4.2). The first terms on the right-hand sides of Eqs. 4.1a and 4.1b are the meridional fluxes of heat in the atmosphere and at the surface from the equator to the poles and C^a and C^s are the heat capacity of the atmosphere and the surface, respectively. SW^a and SW^s are the shortwave radiation absorbed in the atmosphere and by the surface, and

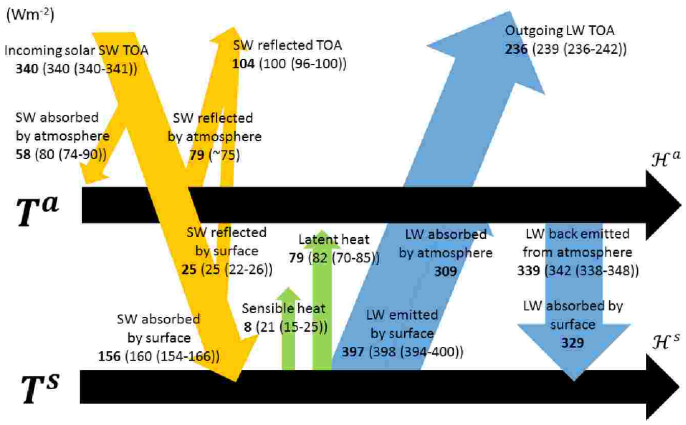

Figure 4.1: Schematic figure over the EBM. Values shown in bold text are output from our EBM while values shown in brackets are from Wild et al. (2015). All values are in Wm^{-2}. TOA is the top of the atmosphere.

LW^a and LW^s are the net LW fluxes (absorbed minus emitted). F^l and F^s represent the flux of latent and sensible heat, respectively, from the surface to the atmosphere. In this study, the model is always run to an equilibrium state. To solve Eqs. 4.1a and 4.1b, we use a forward difference scheme, starting from a specified initial state (a previous steady state), and step Eqs. 4.1a and 4.1b forward in time until the sum of the fluxes are zero. To clarify the various components in the model, Fig. 4.1 shows a schematic of the main components of the EBM with indicative values of the fluxes. Each flux value in Fig. 4.1 is the global mean from a reference run simulated by our EBM. The numbers in parentheses in Fig. 4.1 are radiative fluxes, with uncertainties, from the work published by Wild et al. (2015). The exact values of some of the parameters used within EBMs are not well known, and therefore it is usual to tune these parameters (see e.g. Barker and Ross (1999); Shell and Sommerville (2005)). The EBM presented in this work is tuned to give T^a and

Table 4.1: Global mean variables from the reference run simulated with 380 ppm and 760 ppm CO_2 ($1\times CO_2$ and $2\times CO_2$). [a]Global mean 1979-2015 mean values from ERA-I (Dee et al., 2011), [b]Global mean ISCCP values.

Variable	Description	$1\times CO_2$	$2\times CO_2$	Unit
γ_{LW}^{clear}	Abs. frac. for LW GHG atmos.	0.35	0.38	-
γ_{LW}^{tot}	Abs. frac. for LW GHG + clouds	0.77	0.81	-
γ_{SW}	Abs. frac. for SW atmos.	0.23	0.24	-
f^c	Cloud cover frac.	69 (62[a],67[b])	69	%
ϕ_{ice}	Ice edge latitude	61	90	°S/N
T^s	Temperature at sea level	288.3 (288.1[a])	292.9	K
T^a	Temperature at 650 hPa	269.7 (270.4[a])	272.4	K
h	Total column water vapor	2.31 (2.44[a])	2.74	cm

T^s, total column water vapor (h), lapse rate (Γ), F^l and f^c that are of the same magnitude as ERA-Interim (ERA-I) reanalyzes (Dee et al., 2011), and H^a and H^s that agree with values from National Center for Environmental Prediction (NCEP) (Fasullo and Trenberth, 2008), and at the same time give radiative fluxes that agree with those presented by Wild et al. (2015). The parameters that are used to tune the model are printed in bold in Table 4.2.

4.3.1 *Meridional transport of heat*

In the EBM presented here, we assume the following form of heat transport in the atmosphere and the surface layer,

$$H^a = -2\pi C^a K^a_{eff} \tag{4.2a}$$

$$H^s = C^s(\upsilon^s T^s - 2\pi K^s_{eff}) \tag{4.2b}$$

The right-hand side of Eq. 4.2a and the last term on the right-hand side of Eq. 4.2b represent the diffusive meridional flux,

driven by the turbulent eddy flow, which in turn depends on the baroclinicity, and therefore the meridional temperature gradient. We follow the work of Jentch (1991); Shell and Sommerville (2005); Rose and Marshall (2009) and let the latitude dependent diffusivities K^a_{eff} and K^s_{eff} be simple functions of the temperature gradients,

$$K^a_{eff} = K^a \frac{\partial T^a}{\partial \phi} \tag{4.3a}$$

$$K^s_{eff} = K^s \frac{\partial T^s}{\partial \phi} \tag{4.3b}$$

where K^a and K^s are latitude independent large scale diffusive constants (see Table 4.2). In Eq. 4.2b, an extra term is included for the surface heat flux at low latitudes to represent the surface flow resulting from the Hadley cell in the atmosphere above the surface (Jentch, 1991). This term is a function of T^s and the equatorward effective meridional velocity v^s. Advective flow of heat is significant only at lower latitudes where the Rossby number and Coriolis forces are small, i.e. where the effects from the rotating Earth on the climate system are small. Therefore, outside the Hadley cell region defined, advection is not considered and v^s is set to zero. This approximation is not expected to significantly affect the results since at higher latitudes the meridional temperature gradient lies above the critical gradient for baroclinic instability (Stone, 1978), and the diffusive processes, occurring from baroclinic activity of unstable weather systems, become dominant. The equatorward effective meridional velocity v^s in Eq. 4.2b can be expressed as follows (Jentch, 1991),

$$v^s = \begin{cases} -v^s_0 (1 - (\frac{x}{x_H})^2) \frac{\partial T^s}{\partial \phi} & \phi \leqslant \phi_H \\ 0 & \phi > \phi_H \end{cases} \tag{4.4}$$

assuming that the Hadley cell extends to latitude ϕ_H, with $x = \sin\phi$ and $x_H = \sin\phi_H$. In this model, $\phi_H = 35^\circ$ and, unlike behavior exhibited by AOGCMs (Seidel, 2016), does not change with long-term climate warming. This approximation is consistent with the complexity of the rest of the model.

4.3.2 *Shortwave radiative fluxes*

The terms representing the 650 hPa and surface SW net radiation fluxes, SW^a and SW^s respectively, in Eqs. 4.1a and 4.1b depend on the absorption and reflection of the incoming SW solar radiation:

$$SW^a = s\gamma_{SW}(1 - f^c\alpha_c) + s\gamma_{SW}(1 - \gamma_{SW})(1 - f^c\alpha_c)\alpha_s \tag{4.5a}$$

$$SW^b = s(1 - \gamma_{SW})(1 - f^c\alpha_c)(1 - \alpha_s) \tag{4.5b}$$

where s is the top of the atmosphere SW solar radiation which is a function of latitude (Chýlek and Coakley, 1975; North, 1975a). The fraction of s that is absorbed by the atmosphere, γ_{SW} is calculated as (Lacis and Hansen, 1975):

$$\gamma_{SW} = 0.11 + 2.9\frac{h}{(1 + 141.5h)^{0.635} + 5.925h} \tag{4.6}$$

with total column water vapor (h) and an additional constant 0.11 representing the absorbing effects of the remaining components that affect absorption of SW radiation in the atmosphere, tuned to give values of SW radiation absorbed by the atmosphere that agree reasonably well with the values in the work by Wild et al. (2015). The cloud cover fraction $f^c = 0\,\%$ for clear skies and $f^c = 100\,\%$ for total cloud cover. The cloud albedo, α_c, is set constant at 0.45. The surface albedo α_s, is set to 0.10 when T^s is above a critical temperature T^{crit}, here set to $-2°C$, representing an ice-free surface, and to 0.58 for an ice-covered surface when T^s is below or equal to T^{crit}. The last term of the right-hand side of Eq. 4.5a represents the SW radiation that is not absorbed by the surface, but is reflected back to the atmosphere. The total column water vapor h in Eq. 4.6 is expressed as follows:

$$h = \frac{m_{H_2O} R_H e_s H_{H_2O}}{k T^s \rho_l} \tag{4.7}$$

where m_{H_2O} is the mass of a water molecule, R_H is the relative humidity, k is Boltzmanns constant, ρ_l is the density of liquid

water and H_{H_2O} is the scale height of water vapor, which is itself a function of T^s. The saturation pressure for water vapor, e_s, is calculated from the Magnus approximation of the Clausius-Clapeyron relation (Alduchov and Eskridge, 1995):

$$e_s = Ae^{\frac{BT^s}{C+T^s}} \tag{4.8}$$

with the coefficients A, B and C depending on whether the surface is ice covered or not (see Table 4.2) (Alduchov and Eskridge, 1995). Studies suggest that relative humidity (R_H) does not vary significantly with changing temperature (Held and Soden, 2000), and here zonal mean RH from ERA-I is prescribed and kept constant throughout the simulations.

4.3.3 *Longwave radiative fluxes*

In the model presented, the LW fluxes are described in terms of Stefan-Boltzmann's radiation law and are represented by the following set of equations:

$$LW^a = \varepsilon_a(\sigma(\varepsilon_s T^{s4} - T^{down4} - T^{up4}) + (1-\varepsilon_s)\varepsilon_a \sigma T^{down4}) \tag{4.9a}$$

$$LW^s = \varepsilon_s \sigma(\varepsilon_a T^{down4} - T^{s4}) \tag{4.9b}$$

where σ is Stefan-Boltzmann's constant, T^{down} is the air temperature at the effective altitude at which the atmosphere emits LW radiation back to the surface, and T^{up} is the air temperature at the altitude at which the atmosphere emits LW radiation out to space. The longwave emissivity of the surface, ε_s, is set to 0.97, and the longwave emissivity of the atmosphere is expressed as

$$\varepsilon_a = f^c \gamma^c_{LW} + \gamma^{GHG}_{LW} \tag{4.10}$$

where γ^c_{LW} is the fraction absorbed by clouds, set to 0.65, which is a constant for all latitudes. The fraction (0-1) of the LW radiation that is absorbed by tropospheric water vapor and CO_2 is

based on the simplified analysis completed by Barker and Ross (1999) and calculated as:

$$\gamma_{LW}^{GHG} = 1 - e^{(0.082-(2.38e_s H_{H_2O})R_H+40.3f_{CO_2})^{0.294}} \tag{4.11}$$

The Earth is not a perfect black-body emitter, and absorbs and emits LW radiation with emissivity ε_s. The last term on the right-hand side of Eq. 4.9a represents the LW radiation that is not absorbed by the surface, but reflected back and absorbed by the atmosphere.

The amount of LW radiation emitted back to the surface, or out to space, by the atmosphere is highly dependent on the emission altitude, and therefore temperature. When integrated over the bulk of the atmosphere, the LW radiation emitted from the atmosphere to space is smaller than the radiation emitted back down to the surface since the emission altitude is higher for emission to space, and the temperature is usually lower at such high altitudes. However, because the LW radiation emitted from the atmosphere has contributions from multiple altitudes, it depends on the vertical temperature structure of the atmosphere. There is no radiative transfer code, to our knowledge, simple enough to capture these nuances in LW atmospheric emission in an EBM. Therefore, the emission altitudes, z^{up} and z^{down}, and the corresponding temperatures, T^{up} and T^{down}, in this model have been tuned so that the LW radiation emitted back to the surface and out to space from the atmosphere agrees with the values from Wild et al. (2015). The emission temperatures are calculated as,

$$T^{up} = T^a - \Gamma z^{up} \tag{4.12a}$$

$$T^{down} = T^a + \Gamma z^{down} \tag{4.12b}$$

with the lapse rate Γ calculated as follows within the model,

$$\Gamma = -\frac{T^s - T^a}{z^s - z^a} \tag{4.13}$$

with z^s set to zero and z^a the altitude at 650 hPa, estimated with the hydrostatic approximation. While the altitudes in Eqs. 4.12a

and 4.12b, z^{up} and z^{down} are kept constant, the corresponding emission temperatures T^{up} and T^{down} change with varying T^a and Γ. In reality we expect z^{up} and z^{down} to change with changing LW absorbers, i.e. CO_2 and WV concentrations, and therefore alter T^{up} and T^{down}, and subsequently also the LW radiation fluxes emitted by the atmosphere. Implementation of emission altitudes, z^{up} and z^{down} that change with changing LW absorbers and changing climate in the model could be a useful extension of the model in future analyses, but was not considered to be central to the aims of this study.

4.3.4 *Surface heat fluxes*

The fluxes of heat between the surface and the atmosphere are complicated to measure and to simulate, and errors are often large (Wild et al., 2015). This EBM does not have any representation of the boundary layer, and therefore the simulation of heat fluxes between the surface and the atmosphere must be heavily parameterized. Simulations of sensible heat fluxes in the polar regions, where inversions of the boundary layer can cause a downward net flux of heat are a particular problem. The turbulent fluxes in Eqs. 4.1a and 4.1b, F^l and F_s, are in this EBM simulated with expressions based on the bulk equations used by Shell and Sommerville (2005),

$$F^l = \rho_{air} C_D w_{uv} L \frac{0.622[e_s(T^s) - R_H e_s(T^a)]}{p^s} \tag{4.14a}$$

$$F^s = f_{F_s} \rho_{air} C_D w_{uv} C_p (T^s - T^a) \tag{4.14b}$$

where ρ is the air density, C_D the drag coefficient, L is the latent heat of vaporization and C_p is the specific heat capacity (see 4.2. Because the observed values of turbulent heat fluxes are uncertain (Wild et al., 2015), when used in Eqs. 4.1a and 4.1b, F^s is scaled by f_{F_s} (a constant, see Table 4.2) so that T^a and T^s from our EBM agree with ERA-I reanalyzes, and the radiative flux components agree with (Wild et al., 2015) for the reference conditions. Due to the difficulties in accurately simulating F^s, especially changes in F^s with changing forcings, and

particularly in the polar regions, F^s is prescribed with values from a reference run and therefore does not change when the CO_2 concentration is increased. The zonal mean surface wind, w_{uv}, in Eqs. 4.14a and 4.14b is obtained from the ERA-I reanalysis surface horizontal 10-m wind.

4.3.5 *Representation of cloud cover fraction*

In this work, a simple but robust method has been used to statistically model the dependence of f^c key processes impacting cloud formation. Very simplified, the amount of clouds that are formed depends on the humidity in the air, the static stability of the atmosphere and processes which cause vertical motion. In the EBM presented in this work, the following variables are included, relative humidity, R_H, to represent the moisture in the atmosphere, lapse rate, Γ, to represent the vertical temperature profile and its impact on stability and latent heat flux F^l to represent the vertical velocity due to thermal advection. A least squares regression model, fitted to ERA-I output, is used to capture the functional dependence of zonal mean f^c on zonal mean R_H, Γ and F^l,

$$f^c = \alpha R_H + \beta\Gamma + \delta F^l + \varepsilon \tag{4.15}$$

where ε is the residual of the fit. To assess the importance of vertical velocity due to baroclinic eddies and absolute vorticity advection in our model, the meridional temperature gradient, T^s_γ, was initially included as a predictor in the regression in Eq. 4.15. However, analysis (not shown) indicated that T^s_γ does not play a significant role in the simulation of f^c, as represented in our model, which is consistent with the sensitivity test presented in the work of Roads and Vallis (1984).

The coefficients obtained from the regression model fit (Eq. 4.15), suggest that R_H is the largest contributor to the change in f^c, followed by Γ and F^l. Furthermore, α and β are positive and δ negative, indicating that f^c increases with increasing R_H and Γ and decreases with increasing F^l. Since R_H is prescribed from

ERA-I, changes in Γ are the main driver of changes in f^c in our model which is consistent with the approach used in Roads and Vallis (1984).

4.3.6 *Tuning the model*

Considering the simplicity of the model, the simulated global mean radiative fluxes, after tuning, agree extremely well with the global mean values reported by Wild et al. (2015) (Fig. 4.1). Our EBM simulates global mean values of the radiative fluxes within the uncertainty ranges reported by Wild et al. (2015), except for a smaller value of SW radiation absorbed by the atmosphere and a larger value of SW reflected by the atmosphere than these bounds. The geographical distribution of the SW and LW radiative fluxes simulated with our EBM are shown in Fig. 4.2, and agree reasonably well with the geographical distribution of the multi-model means from 43 CMIP5 models, as presented in Fig. 4 and Fig. 9 in the work of Wild et al. (2015). Our EBM simulated SW fluxes at the TOA agree well with ERA-I (see panel (e) in Fig. 4.2), while our EBM simulated LW fluxes at the TOA are smaller than ERA-I in the low latitudes and larger in the high latitudes, likely because of a lack of latitude dependent cloud properties in our EBM. The outgoing LW at the TOA in panel (e) in Fig. 4.2 is calculated with cloud top temperature from the International Satellite Cloud Climatology Project (ISCCP) (Rossow and Schiffer, 1999).

The main purpose of this EBM is however not to reproduce output that is in perfect agreement with observed or analyzed data, or with output from complex GCMs, but rather to investigate the relative effects of different feedbacks and combinations of those feedbacks. That said, our EBM simulates global mean T^s and T^a that are very close to ERA-I (Table 4.1). However, in the equatorial and polar regions, T^s and T^a are slightly higher compared to ERA-Interim (panel (a) in Fig. 4.3), while close to the ice-edge, T^s is slightly lower compared to ERA-I. In the polar regions, our EBM simulated T^s is 4°C warmer compared to the

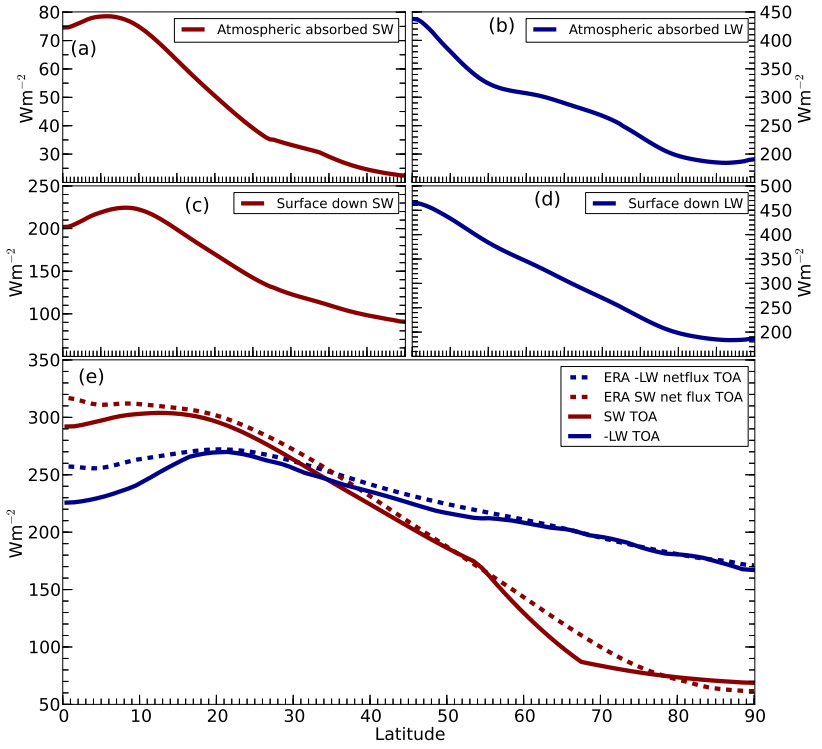

Figure 4.2: EBM simulated zonal mean radiative fluxes. **(a)** SW fluxes absorbed by the atmosphere. **(b)** LW fluxes absorbed by the atmosphere. **(c)** SW fluxes down to surface. **(d)** LW fluxes backemitted to the surface from the atmosphere. **(e)** TOA SW and LW fluxes, compared to ERA-I. Downward fluxes are positive and upward fluxes are negative. Here the negative TOA LW fluxes are shown, for easier comparison with the SW fluxes.

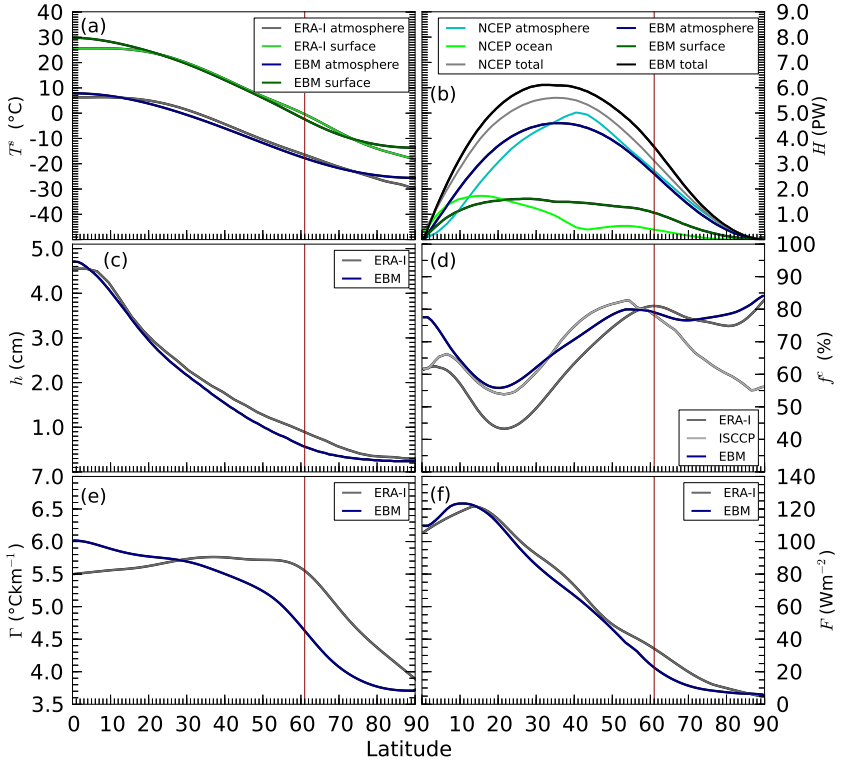

Figure 4.3: Zonal mean output from the reference run simulated with 380 ppm CO_2, and compared to zonal mean 1979-2015 mean ERA-I, 1985-1989 NCEP and 1983-2009 ISCCP data. **(a)** Surface and atmospheric temperatures. **(b)** Ocean, atmospheric and total heat transport. **(c)** Total column water vapor. **(d)** Cloud cover fraction. **(e)** Lapse rate (averaged from surface to 650 hPa). **(f)** Latent heat flux.

ERA-I T^s, which is considerably closer than that in Shell and Sommerville (2005), their T^s being 15°C warmer compared to observed temperatures in the Antarctic. Our relatively low T^s around the ice-edge results in a Γ that is too small in the middle to higher latitudes, especially around the ice-edge (panel (e) in Fig. 4.3) which in turn affects f^c, which is sensitive to the magnitude of Γ. Our EBM simulated F^l is slightly smaller than the ERA-I reanalysis value at latitudes poleward of 15° S/N, and, due to the negative correlation between f^c and F^l, this counterbalances the effect of the small Γ. Around the equator, Γ is higher compared to ERA-I due to the relatively high T^s, which results in a large f^c. Our EBM simulated f^c is in good agreement with both the ERA-I and cloud cover fraction from ISCCP (Rossow and Schiffer, 1999), even though the simulated global mean f^c is slightly larger than both ERA-I and ISCCP (Table 4.1). Our EBM simulated h also agrees well with the ERA-I data (panel (c) in Fig. 4.1 and Table 4.1), even though our simulated h is slightly larger close to the equator, due to the higher T^s, and lower around the location of the ice-edge, due to lower T^s. The red, vertical lines in panels (a) - (f) in Fig. 4.3 show the location of the ice edge for the reference run.

The annual mean atmospheric heat transport from NCEP is 5 PW at its peak around 40° S/N (panel (b) in Fig. 4.3). The annual mean ocean H is 1.5 PW and peaks at around 15° S/N. Our EBM simulated H^a and H^s, 4.6 PW and 1.5 PW, agree well with the values from NCEP, even though our simulated H^s is largest around 25° S/N (panel (b) in Fig. 4.3). The H^a and H^s simulated within our EBM are highly dependent on the latitudinal profile of T^a and T^s (Eqs. 4.2a and 4.2b) and also on the diffusion constants K^a and K^s, which are used as tuning parameters. In this work the values of K^a and K^s are taken from Rose and Marshall (2009), and then tuned so that H^a, H^s, T^a and T^s approximately fit data from NCEP and ERA-I. Our EBM does not include representation of wind-driven gyres, and this is likely to contribute to the difference in our EBM calculated H^a and H^s from NCEP. Furthermore, the poleward shift in the peak in H^s seen in the output from our model, is likely

due to an underestimation of the Hadley cells impact.

In our model, when a feedback is active, the corresponding variable changes with changing temperatures. The altered process feeds back to the climate system by either amplifying or damping the warming. When a feedback is disabled, the corresponding variable is fixed from the reference run where the CO_2 concentration is set at 380 ppm CO_2. The reference simulation in this work refers to the simulation where all processes, viz. α_s, f^c and WV are prescribed with values from the full-feedback simulation, i.e. the simulation where all processes are active (simulation #1).

4.3.7 *Planck feedback*

The Planck feedback is the warming associated with an increase in the direct greenhouse warming response due to the increase in LW radiation absorbed, and reemitted, by the atmosphere with an increased CO_2 burden. The Planck feedback is included in all our EBM simulations. Therefore, the change in temperature due to an increase in CO_2 is affected by both the Planck feedback and the feedbacks from the processes that are active in that particular simulation (see e.g. Roe (2009)),

$$\Delta T = \Delta T_0 + \sum_m k_n \Delta T \tag{4.16}$$

where ΔT is the total temperature change, ΔT_0 is the temperature change associated with the Planck feedback, m is the number of activated feedbacks included in the simulation, $k_n \Delta T$ is the contribution from the n^{th} feedback to the temperature change, and k_n is a constant. The lapse rate feedback is included in all simulations since both the atmospheric and the surface temperatures are allowed to change.

Table 4.2: Parameters used in the model. All parameters are global means, and surface is averaged over land and ocean. Parameters shown in bold style are parameters used to tune the model.

Par.	Description	Value	Unit
α_s	Albedo for ice free surf.	0.10	-
α_s	Albedo for ice covered surf.	0.58	-
α_c	Albedo for clouds	0.45	-
A	Magnus const. (sat. pres.,ice free surf.)	17.625	-
A_i	Magnus const. for sat. pres. over ice	22.587	-
B	Magnus const. (sat. pres.,ice free surf.)	243.04	°C
B_i	Magnus const. (sat. pres. over ice)	273.864	°C
C	Magnus const. (sat. pres.,ice free surf.)	6.1094	hPa
C_i	Magnus const. (sat. pres. over ice)	6.1121	hPa
K	Boltzmann's const.	1.38×10^{-23}	$m^2kgs^{-2}K^{-1}$
T^{crit}	Critical temp. for ice edge latitude	-2	°C
ρ^l	Density of liquid water	1000	kgm^{-3}
K^a	Diffusive const. for atm.	4.40×10^6	m^2s^{-1}
K^s	Diffusive const. for surf.	8.84×10^5	m^2s^{-1}
C_D	Drag coefficient	0.0042	-
ε_s	Emissivity of surf.	0.97	-
G	Gravitational const.	9.81	ms^{-2}
ϕ_H	Hadley cell latitude	35	° N/S
C_a	Heat capacity of atm.	6.0×10^6	$Wsm^{-2}°C$
C_s	Heat capacity of surf. (land/ocean)	1.0×10^7	$Wsm^{-2}°C$
L	Latent heat of vaporization	2.5×10^6	$Wskg^{-1}$
m_{wv}	Mass of water molecule	3.0×10^{-26}	kg
v_0^s	Meridional veloc. within Hadley cell	7.58×10^{-2}	$ms^{-1}°C$
M_a	Molar mass of air	28.9644	$gmol^{-1}$
p^a	Pressure at EBM level	650.00	hPa
p^s	Pressure at surface level	1013.25	hPa
$\gamma_{sw,0}$	SW absorp. frac. from other than water	0.11	-
σ	Stefan-Boltzmann rad. const.	5.67×10^{-8}	$Wm^{-2}K^{-4}$
R	Universal gas constant	8.31447	$Wsmo^{-1}K^{-1}$
f_{F^s}	Tuning const. for sens. heat flux	0.3	-
r	Radius of Earth	6371000	m

4.3.8 *Polar amplification*

We define PA as the ratio of the annual rate of surface warming over the polar regions (zonal mean latitudes poleward of 60°) to the surface warming over equatorial regions (zonal mean latitudes equatorward of 30°), from an increase in CO_2 concentration. To assess the effects from different feedbacks on PA, a PA factor was calculated as follows,

$$f_{PA} = \frac{\Delta_p^s}{\Delta_{eq}^s} \tag{4.17}$$

where Δ_p^s is the change in surface temperature in the polar regions and Δ_p^{eq} is the change in surface temperature in the equatorial regions. To understand PA, it is useful to first look at the impacts from different feedbacks on polar and equatorial warming, separately.

4.4 TEMPERATURE RESPONSES FOR A DOUBLING OF CO_2

4.4.1 *Impacts from isolated feedbacks on polar surface temperatures*

The EBM was run with 380 and 760 ppm CO_2 and with different feedbacks activated or disabled by prescribing the associated model variables. To compare the temperature responses from different feedbacks and different combinations of feedbacks a gain factor, G, denoted as G_p^s and G_{eq}^s for the surface air in the polar and equatorial regions, and G_p^a and G_{eq}^a for the atmosphere in the polar and equatorial regions, is introduced. The gain factor is calculated for each of the eight combinations of different processes, for the surface air and atmosphere in the polar and equatorial regions, as

$$G = \frac{\Delta T_{sim\#i}}{\Delta T_{sim\#8}} \tag{4.18}$$

where $\Delta T_{sim\#i}$ is the temperature change for an increase in CO_2 concentration for simulation #i (i is 1 to 8), and $\Delta T_{sim\#8}$

Table 4.3: Changes in surface temperatures in the equatorial and polar regions (ΔT^s_{eq} and ΔT^s_p) for a doubling of CO_2 for eight possible simulations with α_s, *WV* and f^c feedbacks active or inactive. The f_{PA} and the gain factors G^s_{eq}, G^s_p and $G^s_{f_{PA}}$ are also listed.

Sim.#	α_s	*WV*	f^c	ΔT^s_{eq}(°C)	G^s_{eq}	ΔT^s_p(°C)	G^s_p	f_{PA}	$G_{f^s_{PA}}$
1	On	On	On	2.05	2.41	11.51	4.94	5.61	2.04
2	On	On	Off	1.79	2.11	9.19	3.94	5.13	1.87
3	On	Off	On	1.17	1.38	8.37	3.59	7.15	2.61
4	On	Off	Off	1.00	1.18	5.01	2.15	5.01	1.83
5	Off	On	On	1.50	1.76	4.70	2.02	3.13	1.14
6	Off	On	Off	1.34	1.58	3.01	1.29	2.25	0.82
7	Off	Off	On	0.92	1.08	3.56	1.53	3.87	1.41
8	Off	Off	Off	0.85	1.00	2.33	1.00	2.74	1.00

is the temperature change for an increase in CO_2 for the simulation where all processes are prescribed (#8). The CO_2-induced warming in the polar regions in the simulation when all three processes are prescribed is 2.33°C and is associated with the Planck feedback, and also the meridional transport of heat (see Table 4.3).

When the α_s feedback is active, with the *WV* and f^c feedbacks disabled, ΔT^s_p is 5.0°C with a G^s_p of 2.2 (simulation #4 in panel (a) in 4.4 and 4.3), i.e. ΔT^s_p is 2.2 times larger compared to ΔT^s_p for the Planck-feedback simulation (simulation #8). We find that changes in the surface albedo are the single largest contributor to the warming of the surface in the polar regions (Δ^s_p), followed by f^c, with a G^s_p of 1.5, then *WV*, with a G^s_p of 1.3. There is a significant reduction in warming in the high latitudes when α_s is prescribed (simulations #5, 6, 7 and 8 in panel (a) in 4.4 and 4.3), compared to when all three processes are

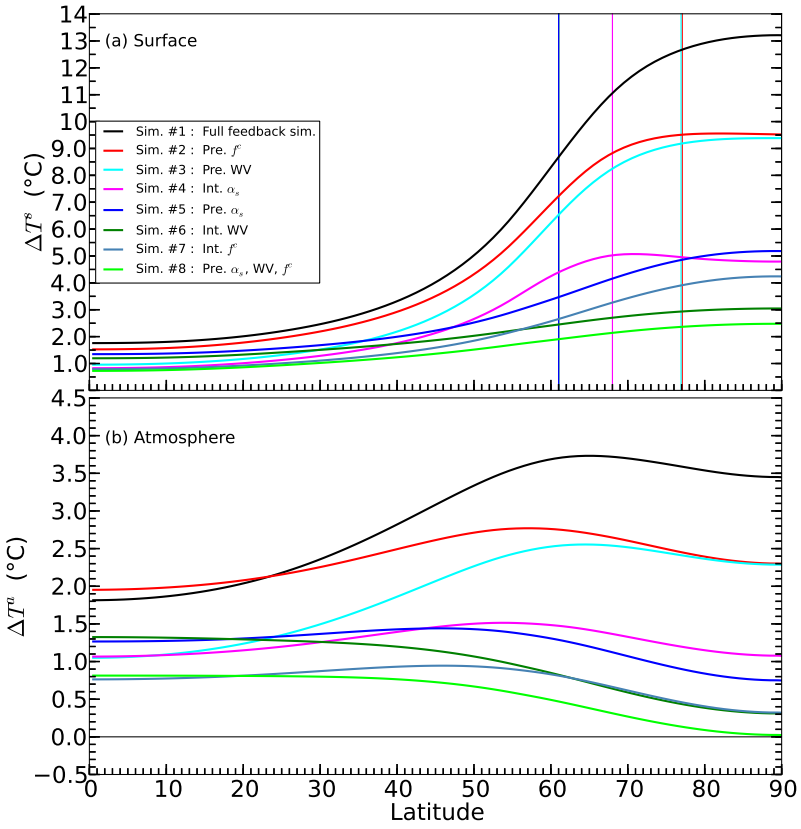

Figure 4.4: Zonal mean surface and atmospheric temperature differences between simulations with 380 and 760 ppm CO_2. All eight possible simulations are shown. The vertical lines show the location of the ice edge for each simulation. Only four lines are visible since the ice edge is constant at 61° for simulations with prescribed surface albedo. **(a)** Surface temperature changes. **(b)** Atmospheric temperature changes.

active. This also suggests that the α_s feedback is the most important contributor to warming in these regions (Winton, 2006; Graversen and Wang, 2009; Randall et al., 2007a).

When f^c interacts with the climate system and α_s and *WV* are prescribed (simulation #7, i.e. the f^c feedback is isolated from the α_s and *WV* feedbacks), ΔT_p^s is smaller than in the isolated α_s simulation (3.6°C compared to 5.0°C), and a factor of 1.5 larger than the Planck-feedback simulation (#8). This suggests that the impact on polar warming by the f^c feedback alone is less than the impact from the α_s feedback alone. On a global scale, the change in f^c, and therefore the amount of SW radiation reflected by the atmosphere (not shown), is small. However, in the polar regions, a large increase in f^c, with a concomitant increase in SW radiation reflected by the atmosphere and a decrease in SW radiation absorbed by the atmosphere and surface, has a cooling effect on T_p^s. This increase in f^c also enhances the greenhouse effect by increasing the emission of LW radiation from the atmosphere with a resultant increase in LW flux at the surface. This enhanced greenhouse effect is larger for the single isolated f^c feedback simulation compared to the isolated α_s feedback simulation (not shown). However, in the isolated α_s simulation, the major cause of the large ΔT_p^s is the strong decrease in reflected SW radiation, and the resultant increase in SW radiation absorbed at the surface due to decreasing surface albedo.

When isolated from the α_s and f^c feedbacks by using prescribed values from the 380 ppm CO_2 reference run, the feedback from *WV* alone gives a ΔT_p^s of 3.0°C (simulation #6) with a G_p^s of 1.3. This is lower than G_p^s for both the simulation when the α_s feedback is isolated (simulation #4, 2.2), and the simulation when the f^c feedback is isolated (simulation #7, 1.5). Increasing *WV* mainly affects the LW radiation absorbed and emitted from the atmosphere, with a slight increase in the amount of SW radiation absorbed by the atmosphere.

For a doubling of CO_2, of the eight possible combinations of interacting processes, the strongest warming in the polar re-

gions, 11.5°C, was found when all three processes are allowed to interact (simulation #1 in panel (a) in Fig. 4.4 and Table 4.3). This is a factor of 5.6 larger than the simulation where all three feedbacks are inactivated (simulation #8).

To investigate the non-linearities in surface temperature response to different combinations of the interactions of the three climate variables, the sum of ΔT_p^s for each variable considered in isolation is compared to ΔT_p^s for the corresponding coupled feedback simulation. When all three variables are kept constant (simulation #8), ΔT_p^s is 2.33°C. When the surface albedo is not prescribed and is allowed to interact, ΔT_p^s increases by 2.68°C to 5.01°C. When the cloud cover is not prescribed and is allowed to interact, ΔT_p^s increases by 1.23°C to 3.56°C, and when water vapor is not prescribed and is allowed to interact ΔT_p^s increases by 0.68°C to 3.01°C. The total effect when all three contributions are added is an extra 4.59°C of warming bringing the total to 6.92°C. However, this value is significantly smaller than the 11.5°C of warming when all three climate variables are fully coupled, i.e. when considered in isolation only 60 % of the warming is simulated. This highlights the non-linear nature of the temperature responses to changes in α_s, f^c and WV and implies that the impact from a combination of feedbacks is not simply the sum of the responses. The feedbacks mutually amplify or dampen each other's impact on the climate system. To gain further understanding of the interactions, we now examine simulations where we add feedbacks to the simulations with isolated feedbacks, so that one single feedback is removed, and the other two are allowed to vary.

4.4.2 *Impacts of coupled feedbacks on polar surface temperatures*

In the polar regions, the amplifying effects of surface albedo and water vapor feedbacks on the surface temperature are strongly enhanced when combined. When adding the WV feedback to the α_s feedback, so that α_s and WV interact with each other and with the climate system, and holding f^c fixed, the polar

surface temperature ΔT_p^s, increases from 5.0°C for the isolated α_s feedback simulation, to 9.2°C (simulation #2 in panel (a) in Fig. 4.4 and Table 4.3). This gives a G_p^s of 3.9, significantly larger than G_p^s for the isolated α_s feedback simulation (#4, 2.2). The linear combination of ΔT_p^s from the isolated α_s feedback simulation and ΔT_p^s from the isolated *WV* simulation is smaller than ΔT_p^s for the coupled α_s -*WV* feedback simulation (5.7°C, or 62% of 9.2°C for the coupled α_s -*WV* feedback simulation) which shows that the interaction between α_s and *WV* strongly enhances polar warming. The main reason for the large ΔT_p^s for the coupled α_s and *WV* feedback run seems to be the absence of changes in SW radiation linked to clouds, and the amplified LW response.

Even though the interaction between α_s and *WV* is important for polar warming, the impact from interacting α_s and f^c is almost as strong. Activating the f^c feedback so that α_s and f^c interact and *WV* is held fixed (simulation #3), gives a ΔT_p^s of 8.4°C, a factor of 3.6 larger than the Planck-feedback simulation (#8). This is slightly less than the contribution from the coupled α_s and *WV* feedback simulation (simulation #2, 9.2°C and with a G_p^s of 3.9). The non-linearity associated with the α_s and f^c feedbacks is also smaller than those for the α_s and *WV* feedbacks. The sum of ΔT_p^s for the isolated α_s simulation and ΔT_p^s for the isolated f^c run is 6.3°C, which is 75% of ΔT_p^s for the coupled α_s -f^c feedback simulation (8.4°C). For the coupled α_s and f^c feedback simulation, the increase in f^c in the high latitudes dampens the warming by reflecting more of the incoming SW radiation back to space partially counteracting the surface albedo change.

Running the EBM with interacting cloud cover fraction and water vapor and with prescribed surface albedo, by fixing the location of the ice-edge and thereby the surface albedo, gives a polar surface warming of only 4.7°C (simulation #5, Table 4.3 and panel (a) in Fig. 4.4), a factor of 2.0 larger than Δ_p^s for the Planck-feedback simulation (#8). This is significantly smaller than Δ_p^s for the simulations with coupled α_s -*WV* and coupled

α_s -f^c feedbacks (9.2°C and 8.8°C, respectively), and also smaller than the isolated α_s simulation (simulation #4, 5.0°C), which, again, shows the importance of the α_s feedback on polar surface warming. The change in polar surface temperature associated with the linear combination of the two individual feedbacks is 4.2°C, 90% of the simulation with coupled f^c -*WV* feedbacks (4.7°C) displaying the most linear response of the three combinations. Output from our EBM shows that there is an increase in the amount of LW radiation emitted from the atmosphere to the surface, due to the increasing amount of LW radiation absorbed by *WV* and f^c. Despite this strengthening of the greenhouse effect, the warming response for the simulation where *WV* and f^c interact and with α_s prescribed (simulation #5) is weak. This is likely because of the lack of increase in SW radiation absorbed by the surface (since there is no change in ice cover), and also the higher quantity of SW radiation reflected to space due to increasing f^c. The peaks in ΔT^s around the location of the ice edge seen for simulation #4 in panel (a) in Fig. 4.4, when f^c and *WV* are prescribed and the α_s feedback is active, occur because of the masking effect from f^cover ice-covered land. In particular, there is a peak in f^c around the ice edge (panel (d) in Fig. 4.3) and therefore less SW radiation is transferred through the atmosphere to the surface. The increase in SW radiation absorbed by the surface due to albedo changes therefore becomes more important in this region. There is no increase in cloud cover fraction since it is prescribed, and therefore there is no change in SW radiation reflected by the atmosphere, which results in a larger ΔT^s in this region. This effect is weaker in simulation #2 because of the warming effect from the *WV* feedback, where the *WV* and α_s feedbacks are active and the f^c feedback is inactive. The interaction between *WV* and α_s enhances the surface warming and shifts the location of the ice-edge towards the poles. More SW radiation is therefore absorbed at higher latitudes, and the peak seen in simulation #4 (see panel (a) in Fig. 4.4) is less pronounced in simulation #2. The peaks in Δh in Fig. 4.5 (panel a) are associated with the peaks in ΔT^s. With a doubling of CO_2, the location of the ice edge on reaching equilibrium (shown as vertical lines in panel

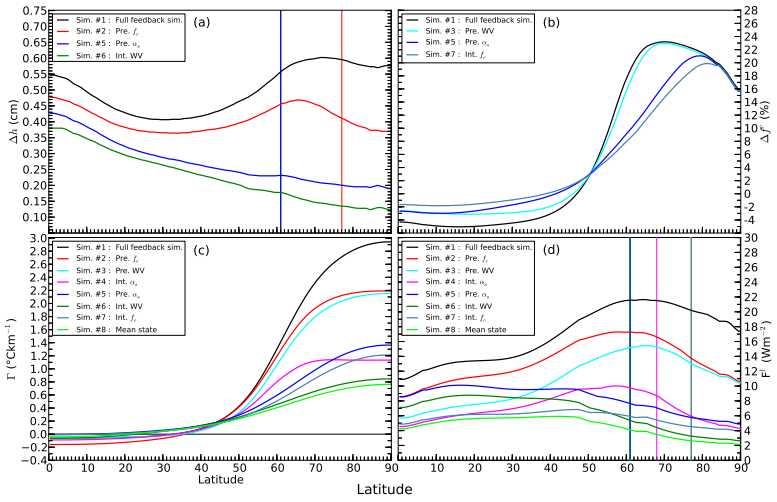

Figure 4.5: Differences between simulations with 380 and 760 ppm CO_2. **(a)** Changes in zonal mean total column water vapor. The vertical lines show the location of the ice edge for each simulation. Simulations with prescribed water vapor are not shown. **(b)** Changes in zonal mean cloud cover fraction. Simulations with prescribed cloud cover fraction are not shown. **(c)** Changes in zonal mean lapse rate. All eight possible simulations are shown. **(d)** Changes in latent heat flux. All eight possible simulations are shown.

(a) in Fig. 4.4) shifts poleward from 62° for the reference run to 68° for the simulation with active α_s feedback (#4), to 77° for the simulation with prescribed f^c (#2), 77° for the simulation with prescribed *WV* (#3) to a completely ice-free Earth for the simulation where all feedbacks interact (simulation #1).

4.4.3 *Impacts from isolated feedbacks on equatorial temperatures*

For a doubling of CO_2, the full feedback run gives a change in surface temperature in the equatorial regions, ΔT^s_{eq}, of 2.0°C. In contrast to the polar regions, in the equatorial regions both changes in surface albedo and cloud cover fraction have small effects on the surface temperature, while the effect from water vapor is significant. There is no change in SW radiation reflected by the surface in the equatorial regions due to changes in α_s, and the increases in LW radiation fluxes emitted by the surface, absorbed by the atmosphere and back-emitted to the surface are small, which results in a small ΔT^s_{eq}. For the isolated α_s feedback simulation (#4), ΔT^s_{eq} is 1.0°C (a G^s_{eq} of 1.2, compared to a G^s_p of 2.2 in the polar regions).

The surface temperature change in the equatorial regions from the isolated f^c feedback simulation is smaller than the ΔT^s_{eq} from the isolated α_s feedback simulation, 0.9°C (a G^s_{eq} of 1.1, compared to a G^s_p 1.5 in the polar regions), due to a reduction of cloud cover fraction, and therefore a weaker greenhouse effect in the equatorial regions. With decreasing f^c, the SW radiation reflected by clouds is also reduced, and the cooling effect becomes less significant. The weakening of the greenhouse effect related to a reduction in f^c is dominant, and therefore a smaller increase in temperature is seen in the equatorial regions compared to the polar regions.

Of the isolated feedback simulations, the largest ΔT^s_{eq} (1.3°C, with a G^s_{eq} of 1.6 compared to only 1.3 in the polar regions) is found for the isolated *WV* feedback case (simulation #6 in Table 4.3 and panel (a) in Fig. 4.4), and is associated with an

increase in LW radiation absorbed by the atmosphere and back-emitted to the surface. A very small decrease in H^s and an increase in H^a over the equatorial regions also contribute (see Fig. 4.6). The decrease in H^s found for all simulations is associated with warming of the polar regions, and therefore a smaller meridional temperature gradient (panel (a) in Fig. 4.6). In the atmosphere, the heat transport, H^a, increases only for the simulation with isolated *WV* feedback (simulation #6), and the simulation where all climate variables are prescribed (simulation #8, panel (b) in Fig. 4.6). These increases in H^a are due to stronger warming in the equatorial regions compared to the polar regions, which result in a larger meridional temperature gradient. The non-linear nature of the α_s, f^c and *WV* interactions and their responses to changes in CO_2 concentration is also clear in the equatorial regions, but is not as prominent as in the polar regions. In the equatorial regions, ΔT^s for the full feedback simulation (simulation #1, 2.1°C) is a factor of 1.3 larger than the linear combination of ΔT^s_{eq} for the isolated feedback simulations (simulations #4, #6 and #7), while in the polar regions, the corresponding factor is 1.8. The sum of Δ^s_{eq} from the isolated α_s, f^c and *WV* simulations is 1.6°C, 76% of the surface temperature change for the coupled full feedback simulation (2.1°C, simulation #1). This suggests an amplifying effect from the coupled feedbacks on the surface temperature in the equatorial regions, just as in the polar regions.

4.4.4 *Impacts from coupled feedbacks on equatorial temperatures*

There is a significant increase in equatorial surface temperature, ΔT^s_{eq}, from 1.0°C to 1.8°C when surface albedo is allowed to interact with water vapor (cloud cover fraction is prescribed, simulation #2), which is a factor of 2.1 larger compared than the Planck-feedback simulation (#8). The increase in ΔT^s_{eq} is mainly associated with the increased absorption of outgoing LW radiation by *WV* in the atmosphere. In the equatorial regions, the feedback effects from α_s and *WV* are amplified when simultaneously active compared to when they occur in isolation. The

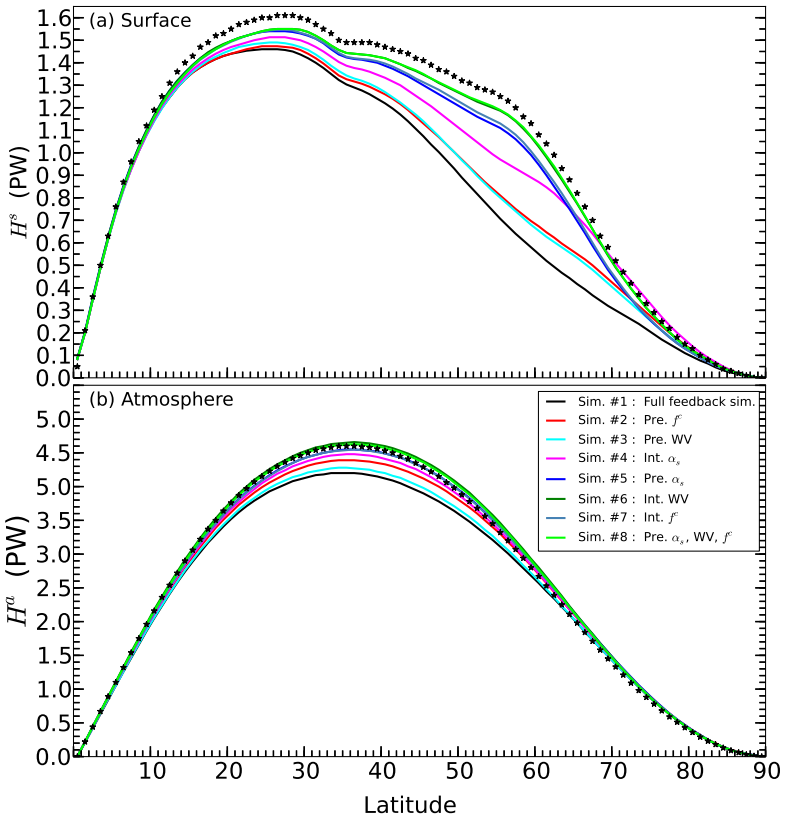

Figure 4.6: Zonal mean heat transport for simulations with 760 ppm CO_2 compared to the reference run (black stars). **(a)** Surface. **(b)** Atmosphere.

sum of ΔT^s_{eq} for the isolated α_s and *WV* feedbacks is 1.5°C, 83% of ΔT^s_{eq} from the coupled α_s and *WV* feedback simulation (#2), compared to 62% for the polar regions.

When instead the α_s and f^c feedbacks are simultaneously active and the *WV* feedback is inactive (simulation #3), ΔT^s_{eq} increases significantly less, to 1.2°C, with a G^s_{eq} of 1.4 (compared to 3.6 in the polar regions). In this case, the decrease in meridional transport of heat is large in the coupled α_s and f^c feedback simulation, which increases ΔT^s_{eq}. However, decreasing ΔT^s_{eq} associated with the weakening of the greenhouse effect from the exclusion of *WV* changes dampens the warming. The equatorial surface temperature change from the linear combination of the individual feedbacks is 1.0°C, 91% of the coupled feedback simulation (#3), compared to 75% in the polar regions, suggesting stronger non-linear effects on temperature responses from coupled α_s and f^c feedbacks in the polar regions than the equatorial regions.

The surface temperature change in the equatorial regions from the coupled *WV* -f^c feedback simulation, with α_s prescribed (simulation #5), is smaller, 1.5°C (a G^s_{eq} of 1.8) than the coupled α_s -*WV* feedback simulation (#2, 1.8°C with a G^s_{eq} of 2.1), due to changes in SW and LW radiation, as well as in meridional heat transport. In the equatorial regions, in the coupled *WV* -f^c feedback simulation, there is a large increase in LW radiation and a small increase in SW radiation absorbed by the atmosphere due to increasing h. Absorption of SW radiation in the atmosphere warms the atmosphere, and since a warmer atmosphere emits more LW radiation, it also warms the surface. However, the reduction in SW radiation reaching the surface roughly cancels this impact. There is also a small decrease in SW radiation reflected by clouds, due to the reduction in f^c, which has a warming effect on T^s_{eq}. However, the smaller ΔT^s_{eq} for the coupled *WV* -f^c feedback simulation (#5) compared to the coupled α_s -*WV* feedback simulation (#2) is associated with a weakening of the greenhouse effect due to reduced f^c and greater meridional heat transport (see Fig. 4.6). The surface temperature change

in the equatorial regions from the coupled *WV* and f^c feedback simulation and with prescribed α_s (#5) is larger than the coupled α_s -f^c feedback run (#3), because of the strong amplifying effect of *WV* variations on ΔT^s_{eq}. Interestingly the *WV* and f^c feedbacks show almost linear behavior, with the sum of ΔT^s_{eq} from the simulations with isolated feedbacks adding up to 1.4°C, 94% of ΔT^s_{eq} for the coupled *WV* -f^c feedback simulation (1.5°C).

4.4.5 *Impacts from different feedbacks on atmospheric temperatures*

Responses in the atmosphere to a doubling of CO_2 can be quite different when compared to responses at the surface (see panel (b) in Fig. 4.4 and Table 4.4). All simulations show warming across all latitudes. The four simulations with interactive *WV* feedback (simulations #1, 2, 5 and 6) show stronger warming in the equatorial regions compared to the simulations with *WV* prescribed (panel (b) in Fig. 4.4 and Table 4.4), due to the increased fraction of LW radiation absorbed by the increased *WV* in the atmosphere. The largest change in T^a in the equatorial regions (ΔT^a_{eq}), 2.2°C is found for the simulation where all three feedbacks are active, i.e. simulation #1. The change in atmospheric temperatures found for the simulation where values are prescribed (simulation #8, 0.9°C in the equatorial regions) are, just as for the surface temperatures, related to the direct effect from increasing CO_2 as well as changes in meridional heat transport.

The single, isolated α_s feedback simulation (#4) gives a ΔT^a_{eq} of 1.1°C, larger by a factor of 1.3 than the simulation when all feedbacks are inactive (simulation #8). This is slightly larger than ΔT^a_{eq} for the single isolated f^c feedback simulation (1.1°C), due to a larger decrease in H^a along with an increased amount of SW radiation absorbed by the atmosphere, caused by a reduction of f^c in the equatorial regions. The atmospheric temperature in the equatorial regions, ΔT^a_{eq}, for the isolated *WV* feedback simulation (1.5°C, with a G^a_{eq} of 1.7) is larger than

Table 4.4: Changes in atmospheric temperatures in the equatorial and polar regions (ΔT^a_{eq} and ΔT^a_p) for a doubling of CO_2 for eight possible simulations with α_s, *WV* and f^c feedbacks active or inactive. The f_{PA} and the gaining factors G^a_{eq} and G^a_p are also listed.

Sim.#	α_s	*WV*	f^c	ΔT^a_{eq}(°C)	G^a_{eq}	ΔT^a_p(°C)	G^a_p	f_{PA}	$G_{f^a_{PA}}$
1	On	On	On	2.15	2.39	3.80	15.83	1.77	2.04
2	On	On	Off	2.00	2.22	2.67	11.13	1.34	1.87
3	On	Off	On	1.27	1.41	2.61	10.88	2.06	2.61
4	On	Off	Off	1.14	1.27	1.33	5.54	1.17	1.83
5	Off	On	On	1.65	1.83	1.17	4.88	0.71	1.14
6	Off	On	Off	1.53	1.70	0.57	2.38	0.37	0.82
7	Off	Off	On	1.03	1.14	0.70	2.92	0.68	0.27
8	Off	Off	Off	0.90	1.00	0.24	1.00	2.74	1.00

Table 4.5: Changes in f^c (%), Γ ($^\circ Ckm^{-1}$), F^l (Wm^{-2}) and h (cm) for eight simulations for a doubling of CO_2 with α_s, WV and f^c feedbacks switched on or off.

				Equatorial region (0°-30° S/N)				Polar region (60°-90° S/N)			
Sim.#	α_s	WV	f^c	Δf^c_{eq}	$\Delta\Gamma_{eq}$	ΔF^l_{eq}	Δh_{eq}	Δf^c_p	$\Delta\Gamma_p$	ΔF^l_p	Δh_p
1	On	On	On	-5.0	-0.052	13.33	0.43	22.9	2.24	21.53	0.55
2	On	On	Off	-	-0.140	10.93	0.37	-	1.83	15.78	0.39
3	On	Off	On	-3.1	-0.047	7.32	-	22.1	1.72	14.81	-
4	On	Off	Off	-	-0.070	6.04	-	-	1.06	7.99	-
5	Off	On	On	-2.7	-0.015	10.01	0.31	16.3	0.98	6.89	0.17
6	Off	On	Off	-	-0.029	8.60	0.28	-	0.65	4.22	0.10
7	Off	Off	On	-1.7	0.009	6.04	-	14.6	0.86	5.33	-
8	Off	Off	Off	-	-0.012	5.41	-	-	0.58	3.33	-

both ΔT^a_{eq} for the isolated α_s and isolated f^c feedback simulations due to changes in the fraction of LW absorbed caused by increasing h.

The largest variations linked to the WV feedback in the equatorial regions are associated with changes in h. When the α_s feedback is inactive, changes in h in the equatorial regions are larger than the corresponding changes in h in the polar regions (panel (a) in Fig. 4.5 and Table 4.5). When the α_s feedback is active, even though the changes in h are large in the equatorial regions, the largest changes are observed around the location of the ice edge (panel (a) in Fig. 4.5 and Table 4.5), followed by the polar regions.

The changes in T^a in the polar regions (ΔT^a_{eq}) are greatest when α_s is active (simulations #1, 2, 3 and 4 in panel (b) in Fig. 4.4 and Table 4.4). This is associated with an increase in LW radiation emitted from the surface and absorbed by the atmosphere

in regions where the surface albedo has changed, representing ice melt. The largest ΔT_p^a is found for the simulation when all three feedbacks interact (simulation #1, 3.8°C). When the α_s is fixed, there is less warming of the polar surface, and therefore less LW radiation emitted to the atmosphere. As a result, the polar atmosphere warms less, the meridional temperature gradient also changes less and the decrease in H^a is correspondingly smaller, which means less heat is distributed from lower latitudes towards the pole.

4.4.6 *Underlying processes affecting different feedbacks*

According to our simulations, for a doubling of CO_2, there is no change in cloud cover fraction averaged over the globe for the simulation when all three feedbacks are active (Table 4.1). However, there are variations at different latitudes which cancel globally. While reductions in f^c are observed in lower latitudes, equatorward of 40-45°, there are increases at higher latitudes for all simulations (panel (b) in Fig. 4.5 and Table 4.5), in agreement with earlier studies (e.g. Roads and Vallis (1984) or Trenberth and Fasullo (2010)).

In the polar regions, the cloud cover fraction increases for all simulations, with the largest changes found for the full feedback run (#1, 23%), followed by the coupled α_s -f^c feedback simulation with the *WV* feedback prescribed (simulation #3, 22%), and the f^c -*WV* feedback simulation with prescribed α_s (#5, 16%), while the smallest change is found for the isolated f^c feedback only simulation (#7, 15%). This suggests that other processes interact in such a way that the cloud fraction varies more strongly when those other feedbacks are active. The magnitude of changes in the cloud cover fraction are related to changes in the lapse rate, latent heat flux and total column water vapor, denoted $\Delta\Gamma_{eq}$, ΔF^l_{eq} and Δh_{eq} in the equatorial regions, and $\Delta\Gamma_p$, ΔF^l_p and Δh_p in the polar regions.

The lapse rate is positively correlated with the cloud cover frac-

tion, and the positive Δf^c in the polar regions (Δf^c_p) is controlled by the positive $\Delta\Gamma_p$. The largest change in Γ_p ($2.2^\circ\,Ckm^{-1}$) occurs for the full feedback simulation (#1). This large change in Γ_p indicates that the air in the polar regions become more unstable with CO_2-induced warming. The smallest change in Γ_p (0.7° C km-1) occurs for the isolated f^c feedback simulation (of the simulations with active cloud cover feedback). The largest changes in cloud cover fraction are also found for simulations with the largest changes in latent heat flux in the polar regions. Due to the negative correlation between cloud cover fraction and latent heat flux, as stated in Eq. 4.15, there is therefore a competing effect between ΔF^l_p and $\Delta\Gamma_p$. However, the impact of increasing lapse rate is greater, and a net increase in cloud cover fraction is found for all simulations in the polar regions.

In contrast to the polar regions, changes in f^c in the equatorial regions (Δf^c_{eq}) are negative for all simulations. The most negative Δf^c_{eq} is found for the case where all three feedbacks are active (-5.0%, simulations #1), followed by the simulation when α_s and f^c interact (-3.1%, simulation #3), the simulation when f^c and WV interact (-2.7%, simulation #5), and is least negative for the isolated f^c feedback simulation (-1.7%, simulation #7). The simulation with the most negative Δf^c_{eq}, i.e. the full feedback simulation (#1, panel (b) Fig. 4.5 and Table 4.5), has the most negative $\Delta\Gamma_{eq}$ ($-0.052^\circ\,Ckm^{-1}$, panel (c) in Fig. 4.5 and Table 4.5), the largest ΔF^l_{eq} ($13.3\,Wm^{-2}$, panel (d) in Fig. 4.5 and Table 4.5) and the largest Δh_{eq} (panel (a) in Fig. 4.5 and Table 4.5) of the simulations when the f^c feedback is active.

The difference in $\Delta\Gamma_{eq}$ between the isolated f^c feedback simulation (#7) and the simulation where surface albedo and clouds interact and the WV is held constant (simulation #3) suggests that the α_s feedback affects f^c not only in the polar regions, but also in the lower latitudes, due to larger transport of heat for the isolated f^c feedback simulation (#7), especially in the atmosphere (Fig. 4.6), which contributes to a reduction in T^a_{eq} and an increase in $\Delta\Gamma_{eq}$.

In the polar regions, the magnitude of the change in latent heat flux appears to depend on the activation of the surface albedo feedback, with the largest ΔF_p^l ($21.5\,Wm^{-2}$) found for the full feedback simulation. The change in h is smaller in the polar region compared to the equatorial regions for simulations where α_s is prescribed (simulations 5 and 6 in Fig. 5a and Table 5). As a result, the absorption of LW radiation in the polar atmosphere declines, and the impact from *WV* on T_p^a and T_p^s and therefore F_p^l and Γ_p becomes less significant. For simulations with active α_s feedback, the polar surface temperature rises more than the atmospheric temperature, which increases the changes in latent heat flux and lapse rate.

Changes in cloud cover fraction from the full feedback simulation (#1) and the simulation where α_s and f^c interact (#3, *WV* feedback is inactive), as well as the simulation where *WV* and f^c interact (#5, α_s prescribed) and the isolated f^c feedback simulation (#7) are very similar for the highest latitudes, because the cloud cover fraction saturates in these regions for doubling CO_2 concentrations (Table 4.5 and panel (b) in Fig. 4.5).

The main driver of changes in latent heat flux in the equatorial regions is the effect from changes in total column water vapor, h (panel (a) in Fig. 4.5 and Table 4.5), which act to increase the atmospheric temperature, T_{eq}^a, mainly through increasing the absorption of LW radiation. The warmer atmosphere emits more LW radiation to the surface which increases the surface temperature and thereby also the latent heat flux, as well as the total column water vapor. A larger latent heat flux transports more heat from the surface to the atmosphere, enhancing the warming of the atmosphere, but also contributes a cooling effect to the surface. In the equatorial regions, the largest ΔF^l are found for simulations with the *WV* feedback activated (see simulations #1, #2, #5 and #6). The isolated α_s and isolated f^c feedback simulations give similar latent heat fluxes in the equatorial regions, ΔF_{eq}^l,($6.0\,Wm^{-2}$, simulations #4 and #7).

4.4.7 *Polar amplification for a doubling of CO_2*

The Planck feedback associated with increased CO_2 concentrations causes a polar amplification even when all three processes are prescribed (simulation #8), with a f_{PA} of 2.7. This is because water vapor is a smaller component of the greenhouse effect at the poles, where *WV* is sparse because of low temperatures, than at the equator.

Our model shows that CO_2-induced changes in surface albedo, especially when interacting with clouds, play an important role in PA. For a doubling of CO_2, the largest polar amplification factors, f_{PA}, are found for simulations when the α_s feedback is active (simulations #1, 2, 3 and 4 in Table 4.3). This is expected since changes in surface albedo increase the surface temperature in the equatorial regions, T^s_{eq}, only indirectly through a small decrease in transport of heat from the equator to the poles. The polar amplification factor for the simulation where the α_s feedback is active and isolated from the other two feedbacks is 5.0 (simulation #4), a factor (denoted $G^s_{f_{PA}}$ in Table 4.3) of 1.8 larger compared to the simulation with all feedbacks inactive (simulation #8, Table 4.3), mainly due to a stronger warming in the polar regions caused by melting ice, and therefore increased SW radiation absorbed by the surface.

The impact from the isolated f^c feedback on PA is significantly less compared to the impact from the isolated α_s feedback with a f_{PA} of 3.9 (rather than 5.0 for the isolated α_s simulation). The smaller contribution from the isolated f^c feedback to PA is related to the smaller ΔT^s_p (3.9° C compared to 5.0° C for the isolated α_s feedback simulation).

In contrast to the α_s and f^c feedbacks, the *WV* feedback has a strong warming effect in the equatorial regions, which dampens the polar amplification. The strongest polar amplification is found when *WV* is prescribed, and α_s is allowed to interact with f^c, with a polar amplification factor of 7.2 (simulation #3 in Table 4.3). This is a factor of 1.3 larger than f_{PA} for the full

feedback run (#1, 5.6), because of the removal of the strong warming effect from *WV* at the equator, in combination with the strong warming effect from the α_s-f^c interaction at the pole. For the simulation with an isolated *WV* feedback (simulation #6), the relatively small ΔT_p^s and larger ΔT_{eq}^s results in a f_{PA} that is significantly less than the f_{PA} for the isolated α_s and f^c feedback simulations (2.3 compared to 5.0 and 3.9). The polar amplification factor is larger for the Planck feedback simulation (#8, 2.7) compared to the isolated *WV* simulation, indicating that *WV* does not contribute to PA as defined in Eq. 4.17. Even though *WV* alone (simulation #6) has an amplifying effect on the warming of the poles, *WV* appears to reduce the effects from α_s and f^con f_{PA}. When the *WV* feedback is coupled to the f^c feedback, and α_s is prescribed (simulation #5), f_{PA} decreases significantly to 3.1 relative to the isolated f^c feedback simulation (3.9), despite a relatively large ΔT_p^s.

4.5 POLAR AMPLIFICATION FOR A QUADRUPLING OF CO_2

Additional simulations were performed with a quadrupling of CO_2 (from now on referred to as $4\times CO_2$ runs) to test the linearity of the polar amplification response to increases in CO_2 concentration. While the polar surface temperature is larger for the $4\times CO_2$ simulations compared to the $2\times CO_2$ simulations as expected, the polar amplification factor, f_{PA}, is reduced in all cases (Table 4.6). This is due to large increases in equatorial surface temperatures, ΔT_{eq}^s. For the $4\times CO_2$ runs, simulations with active α_s feedback are again found to give the largest polar amplification factors, due to large changes in T^s in the polar regions. Interestingly, polar amplification for the simulation when α_s and *WV* interact (simulation #2, f^c prescribed), the simulation when α_s and f^c interact (simulation #3, *WV* is inactivated) and the isolated α_s feedback simulation (#4) have larger values of f_{PA} than the full feedback simulation (#1). For the $2\times CO_2$ runs, only the coupled α_s-f^c simulation (#3, *WV* is inactivated) had a larger f_{PA} than the full feedback run (#1). This points to non-linearities in our simulation, in particular

the amplifying warming effect from the *WV* feedback becomes more important when the temperature increases, and therefore $G^s_{f_{PA}}$ is larger for the $4\times CO_2$ compared to the $2\times CO_2$ runs when the *WV* feedback is active (simulations #1, #2, #5 and #6, Table 4.6, and is smaller when the *WV* feedback is inactive (simulations #3, #4, #7, and #8).

To estimate the relative nonlinearities for the three feedbacks, the percentage change (compared to the $2\times CO_2$ simulations) in f_{PA} for each simulation is presented in Table 4.6.

Table 4.6: Changes in surface temperatures in the equatorial and polar regions (ΔT^s_{eq} and ΔT^s_p) for a quadrupling of CO_2 for eight possible simulations with α_s, *WV* and f^c feedbacks switched on or off. The f_{PA}, the gaining factors G^s_{eq} and G^s_p, as well as fractional changes in f_{PA} with respect to f_{PA} for a doubling of CO_2 ($2\times CO_2$) (from Table 4.3) are listed.

Sim.#	α_s	*WV*	f^c	$\Delta T^s_{eq}(^\circ C)$	G^s_{eq}	$\Delta T^s_{eq}(^\circ C)$	G^s_p	f_{PA}	$G^s_{f_{PA}}$	f_{PA}% of $2\times CO_2$
1	On	On	On	4.01	1.74	14.41	2.72	3.59	1.56	64.0
2	On	On	Off	3.75	1.63	13.75	2.60	3.67	1.60	71.5
3	On	Off	On	2.71	1.18	12.73	2.41	4.70	2.04	65.7
4	On	Off	Off	2.58	1.12	11.76	2.22	4.56	1.98	91.0
5	Off	On	On	3.57	1.55	7.93	1.50	2.22	0.97	71.9
6	Off	On	Off	3.30	1.43	6.27	1.19	1.90	0.83	84.4
7	Off	Off	On	2.45	1.07	6.82	1.29	2.79	1.21	72.1
8	Off	Off	Off	2.30	1.00	5.29	1.00	2.30	1.00	83.9

The full feedback simulation shows the largest change in f_{PA} (64% of simulation #1 for the $2\times CO_2$ run, see Table 4.6, followed by the simulation with coupled α_s-f^c feedbacks (#3) (66% of simulation #3 for the $2\times CO_2$ run). A large change in f_{PA} com-

pared to the corresponding 2×CO_2 simulation indicates strong non-linear behaviour with increasing CO_2 concentrations. The smallest change in f_{PA} is found for the isolated α_s simulation (#4, 91% of simulation #4 under the 2×CO_2 run), which suggest that this case is the most linear of the eight simulations. This means that interactions between feedbacks likely become more important with increasing CO_2 concentrations.

4.6 DISCUSSION AND CONCLUSION

Output from our newly developed EBM which incorporates surface albedo, water vapor and cloud feedbacks suggest that changes in α_s is the main contributor to polar warming as might be expected, and its effect is enhanced when interacting with either *WV* and/or f^c. The feedbacks from interacting f^c and *WV* are also important, but weaker compared to when the α_s feedback is activated. For a doubling of CO_2, the temperature change in the polar regions from our EBM simulations reaches 11.5° C when run to equilibrium when all feedbacks are active. Graversen et al. (2014) reported a temperature change of ~6° C in the Arctic (>60° N) and slightly less in the Antarctic (>60° S), for a doubling of CO_2 simulated with a AOGCM model, when run to equilibrium, and including all feedbacks. They also reported an approximate halving of the temperature increase, 3° C in the Arctic and 3.5° C in the Antarctic, for a simulation when they locked the surface albedo. The locked albedo simulation presented in the work of Graversen et al. (2014), is comparable to our coupled *WV*-f^c feedback simulation, with α_s prescribed, which gives a change in polar surface temperature of 4.7° C, also approximately half of the full model simulation (11.5° C). The temperature changes calculated with our EBM are larger than those in Graversen et al. (2014), but in good agreement with the output from the moist aqua planet EBM developed by Roe et al. (2015). For a doubling of CO_2, Roe et al. (2015) reported that the high latitude surface temperature increase reduced from ~9 to 11° C for their full model run, to ~4 - 7° C with suppressed surface albedo, consistent with the

output from our EBM. One of the differences between an aqua planet model and a model with both land and ocean lie the heat transport and diffusion processes. A model with representation of both land and ocean would transport more heat to the poles and therefore the warming of higher latitudes would be greater. In our EBM there is no distinction between land and ocean, and the surface heat transport is represented by transport of heat in the ocean, and can therefore be compared to the aqua planet model presented by Roe et al. (2015).

According to the output from our EBM, α_s alone, with f^c and *WV* held fixed, warms the polar regions by 5.0° C. The warming from f^c as an isolated feedback, is 3.6° C, while *WV* alone contributes 3.0° C. These changes are larger than the changes published by Pithan and Mauritsen (2014). Pithan and Mauritsen (2014) examined output from CMIP5 models to find that the α_s feedback is the major contributor to Arctic warming, changing polar surface temperature by ~2° C, followed by clouds (1° C change) and *WV* (~0.5° C change) feedbacks. The CMIP5 simulations studied in the work of Pithan and Mauritsen (2014) are transient states, and our equilibrium runs would be expected to be larger as observed.

The contribution from cloud cover fraction, as the difference between a full feedback run and a locked cloud cover fraction run, to polar warming was reported by Vavrus (2004) to be ~40%. According to the output from our EBM, the impact from f^c on polar warming in the locked-f^c case is small, roughly 9% of the full feedback simulation. The impact from changing f^c, when considered in isolation, on warming of the polar surface in our EBM, is on the other hand larger (~69% of the full feedback run).

The non-linear nature of the temperature responses to increasing CO_2 burden was highlighted by comparing the sums of changes in surface temperature from individual feedbacks, to changes in surface temperature from the coupled feedbacks. It has been suggested that the discrete "jump" from albedo for

ice-free surface to albedo for ice-covered surface is responsible for the non-linearities in temperature responses seen in EBMs. These non-linearities have been shown to increase when feedbacks are added (Wagner and Eisenman, 2015), which is in line with what our EBM produces. According to the output from our EBM, the sum of the contributions to surface temperature changes is found to be smaller than the surface temperature change from the coupled feedback simulation for all combinations of feedbacks. The α_s feedback has the strongest non-linear behavior followed by the *WV* and f^c feedbacks. The non-linearities are stronger in the polar regions compared to the equatorial regions, since the effect from changing surface albedo on the surface temperature is greater in the high latitudes. At high latitudes, the linear combination of temperature changes from the individual α_s and f^c feedbacks is only ~75% of the temperature change from the coupled α_s -f^c feedback simulation. At low latitudes this value is 91%, and closer to linear (where linear is 100%). These numbers are reduced, which implies stronger non-linearities, when the *WV* feedback is added. The surface temperature increase due to increased surface absorbed SW and LW radiation associated with increasing surface albedo and clouds, is enhanced by additional absorption of LW radiation emitted from the atmosphere, when the *WV* feedback is added. The linear combination of temperature changes from the three individual climate variables is ~60% of the coupled α_s -, *WV*- and f^c simulation in the high latitudes and ~76% in the low latitudes. The *WV* and f^c feedbacks are relatively linear over both the equator and the poles, which appears to be due to the cooling effect from the reflection of SW radiation by clouds.

The contribution of different feedbacks to the warming of the polar regions is slightly different compared to the contribution to PA, due to the latter quantity also being impacted by warming in the equatorial region. Decreasing surface albedo in the high latitudes has an important impact on PA by increasing the amount of SW radiation absorbed at the surface, but also through an indirect effect on the low latitude temperat-

ures, by decreasing the meridional temperature gradient and therefore the transport of heat from the equator to the poles, which slightly warms the equatorial regions. According to our model, the largest impact from a single feedback on PA can be attributed to the α_s feedback. This is consistent with the results presented by Graversen et al. (2014), who, by suppressing the surface albedo feedback, found that the surface albedo feedback accounts for 40% of PA in the Arctic and 65% of PA in the Antarctic, in the CCSM4 climate model. By prescribing the surface albedo in our EBM, which is comparable to the simulation studied by Graversen et al. (2014), ~44% of PA can be attributed to the surface albedo feedback. However, coupling between feedbacks is important for changes in surface temperatures, and if looking at the EBM output from our isolated surface albedo feedback simulation, when the other two feedbacks are prescribed, as much as ~89% can be attributed to the surface albedo feedback.

We have shown that coupling between feedbacks is important for warming in the polar regions and for PA, and the output from our simulations suggests that feedbacks from α_s-f^c interactions play a major role in warming the polar regions as well as in PA. The α_s-*WV* feedbacks are important for polar warming. However, *WV* also has a strong warming effect in the equatorial regions. This reduces the polar amplification (which by definition is the warming of the polar regions relative the lower latitudes), a result supported by Payne et al. (2015). According to the output from our EBM, the net increase in SW and LW radiation absorbed by the surface in the equatorial region is smaller when *WV* is fixed (simulation #3) compared to when all feedbacks are active (simulation #1). However, the effect of decreasing heat transport when the polar regions warm also plays a role in the magnitude of the PA (Alexeev and Jackson, 2013). In our model, there is more heat transported from the equatorial regions to the poles when *WV* is fixed compared to when all climate variables vary (Fig. 4.6), contributing to a stronger PA. Payne et al. (2015) reported amplified warming from the *WV* feedback in the equatorial region, with a ΔT^s_{eq}

of 2°C, which is larger than ΔT_{eq}^{s} from the isolated *WV* feedback simulated with our EBM. This discrepancy is likely to be caused by the transport of heat which is included in our model, and omitted in the work presented by Payne et al. (2015). The strong positive feedback from *WV* was also shown in the work of Roe et al. (2015).

Even though the approach to simulating clouds in this work is simple, our EBM gives cloud cover fractions that agree well with earlier published results. For a doubling of CO_2, our EBM gives an unchanged global mean f^c, with negative changes in the lower latitudes and positive changes in the higher latitudes, for all simulations. This is consistent with early work by Roads and Vallis (1984), who used an EBM to show that cloud cover changes tend to be small, except at higher latitudes where cloud cover was observed to increase strongly with increasing temperatures. Furthermore, at the end of the 21^{st} century, CMIP3 models consistently project negative changes (~-3% - 0%) in f^c for latitudes below ~50° and positive changes for higher latitudes (~1.5 - 2% for southern high latitudes and > 4% for northern high latitudes) (Trenberth and Fasullo, 2010). However, the CMIP3 simulations are transient simulations, while our EBM output results are associated with equilibrium states and therefore are expected to be of different magnitude. The simulations of cloud cover from CMIP3 are also associated with large biases, and therefore the results may be questionable (Trenberth and Fasullo, 2010).

The model presented here is simple with many processes omitted. Further developments that could improve the model, and open possibilities for other analyses, include implementation of temperature dependent cloud properties, such as taking into account the effects from clouds with different phases on absorption of LW radiation as well as the reflection of SW radiation. The model is averaged over the hemispheres which also should be considered with caution, since the magnitude of polar amplification is uncertain, especially in the Southern hemisphere. Furthermore our model is averaged over land and ocean. In-

clusion of land-sea contrast in our EBM would affect the parametrization of meridional transport of heat, surface albedo and surface fluxes. However, in this model surface albedo is set to a constant, and so is the representation of air over land or ocean in surface heat fluxes (i.e. the heat capacity) and in meridional transport of heat (heat capacity and diffusive constants). Therefore inclusion of land-sea contrast would not have an affect on our models ability to simulate the temperature response. Analysis using this model would support further understanding of feedbacks from clouds, and their non-linear interactions with the other feedbacks in the climate system. In the work presented in this chapter, we use additive non-linearity to investigate the feedback strengths in the CO_2-induced warming effects from ice albedo, cloud cover and water vapor. The aim of our paper is to investigate how much the temperature response changes when different feedbacks are activated or kept fixed. This could be a bit confusing sine in the literature multiplicative non-linearity is commonly used. Here follows a brief explanation of the non-linear response as commonly used in the literature.

The temperature response ΔT to a perturbation ΔR of the climate system can be written as follows (Roe, 2009),

$$\Delta T = \lambda \Delta R \tag{4.19}$$

The perturbation ΔR, can be expanded as a Taylor series,

$$\Delta R = \frac{dR}{dT}\Delta T + O(\Delta T^2) \tag{4.20}$$

where $O\Delta(T^2)$ is considered the non-linear response to that perturbation, and is assumed to be small. This approach is very different compared to the method used in the work presented in this chapter. However, an important point here is that we do not try to show that the feedbacks are non-linear (we know that already), we try to show how the strengths of the non-linarites differ between different combinations of contributions to temperature changes from feedbacks.

5

AN EXPLORATION OF THE IMPACTS OF CLOUD ALBEDO ON CLIMATE SENSITIVITY USING AN ENERGY BALANCE MODEL

In this chapter results from an extended version of the energy balance model (EBM) described in Chapter 4 are presented. In the work presented in the previous chapter an EBM was used to investigate interactions between the feedbacks from surface albedo, water vapour and cloud cover fraction and their relative impacts on polar amplification. In this chapter the EBM has been extended so that it includes latitude- and temperature dependent shortwave (SW) radiation reflected from clouds, i.e. cloud albedo and cloud top temperature that change with changing temperature.

5.1 ABSTRACT

The effects from reflectivity of clouds (cloud albedo) on the feedbacks from surface albedo, water vapor and cloud cover (referred to as climate variables), and the impact the interaction between these climate variables has on the surface temperature are examined, using an energy balance model (EBM), presented in the recently published work by Södergren et al. (2017). Output from simulations with all possible combinations of climate variables activated or prescribed with values from a reference run are examined. For a doubling of atmospheric concentration of carbon dioxide, the output from the simulations show that there is an increase in cloud albedo in the low and high

latitudes due to an increase in cloud temperature (and therefore an increase in the fraction of water droplets compared to ice crystals), and a very small decrease in cloud albedo in mid latitudes due to a decrease in cloud temperature. Changes in surface albedo greatly affect surface and atmospheric temperatures in the high latitudes, and therefore also cloud temperatures and cloud albedo. The cloud albedo in this EBM depends on atmospheric temperature and lapse rate, and therfore there is a large impact from cloud albedo on simulations where the surface albedo feedback is fixed with values from a reference simulation. Furthermore, CO_2-induced cloud albedo changes have the greatest effect on simulations where there is little or no interaction between surface albedo, water vapour and cloud cover, because the change in LW radiation emitted from the atmosphere to the surface is then small compared to the change in SW radiation reflected by clouds out to space.

5.2 INTRODUCTION

Climate sensitivity (CS) is a metric determined by a set of feedback mechanisms that can be used for analysis of the climate system's temperature response ΔT, to a perturbation (i.e. a forcing) F, externally imposed by for example greenhouse gases (GHGs), solar variability, etc. (Gregory et al., 2004; Gregory and Webb, 2007; Collins et al., 2013).

The difficulties in calculating CS are illustrated by the spread reported in the latest report from the Intergovernmental Panel on Climate Change (IPCC) (Collins et al., 2013). According to the IPCC, the global temperatures simulated under the representative concentration pathways (RCPs) 4.5 and 6.0 emissions scenarios are projected to exceed 1.5°C above 1850-1900 temperatures (with high confidence) at the end of the century, while for the RCP8.5 emissions scenario, the global mean temperature is projected, with medium confidence, to exceed 4°C. This range of threshold temperatures (1.5-4°C) has not narrowed since the Charney Report (1979). However, at the time of the Charney

report, the uncertainties in projections were large and uncertain. Climate models are now more detailed and their levels of complexity have increased. There is now also more knowledge about the uncertainties associated with projections.

The feedbacks from surface albedo, water vapour/temperature lapse rate and clouds are important processes in CS estimations (Stocker et al., 2013). In general, there is a good agreement among models clear-sky radiative flux responses, while discrepancies in their total-sky responses are large. This suggests that clouds are key contributors to the uncertainty in CS, while there are also inter-model differences in water vapour and surface albedo feedbacks that are likely to contribute to the spread (Cess et al., 1996; Colman, 2003; Bony et al., 2006; Soden and Held, 2006).

Feedback processes may either amplify or dampen the direct effect of a given forcing agent, which further complicates analysis of CS (Hegerl and Zwiers, 2011). For example, clouds cool the Earth by reflecting some of the incoming SW radiation from the sun. Clouds also warm the surface through their absorbing/emitting effects on LW radiation in the atmosphere. The feedback from clouds can thus be positive or negative. According to the latest IPCC report (Stocker et al., 2013), the net radiative feedback due to surface albedo and water vapour is positive. Furthermore, the net radiative feedback due to all cloud types is likely positive. However, the spread between models is large and some models still suggest negative cloud feedback (Colman, 2003; Soden and Held, 2006; Stocker et al., 2013; Zelinka et al., 2017).

As earlier simulations with our EBM show, changes in cloud cover fraction have a significant impact on the energy budget of the Earth. However, cloud properties, such as phase, cloud top temperature and particle size, also strongly control the cloud radiative effects (Kay et al., 2016). Water in the form of gas is an efficient absorber of longwave (LW) radiation in the atmosphere, but also affects the radiation budget of Earth by absorbing parts

of the shortwave (SW) radiation from the sun. When examining the output from climate models, it has been found that water vapour, often in combination with lapse rate, increases model sensitivities by about a factor of two (Manabe and Wetherald, 1975; Schneider et al., 1999; Stocker et al., 2013), which makes water vapour the dominant GHG.

The conversion of water vapour into clouds is controlled by microphysical processes, such as formation of ice crystals or water droplets. The properties of clouds (e.g. reflectivity and emissivity), and therefore the effect of clouds on the radiation budget of Earth, depend on the interaction of these microphysical processes. The reflectivity of clouds is directly related to the amount of water droplets and ice crystals, with water droplets being more efficient than ice crystals in both reflecting SW radiation and absorbing LW radiation. Uncertainties in cloud SW radiation components have been found to contribute to uncertainties in projections of GHG induced surface temperature changes. Especially, as suggested by both models and observations, supercooled water in clouds strongly influences cloud radiative effects (Kay et al., 2014; Forbes and Ahlgrimm, 2014; Cesana and Storelvmo, 2007). Lack of supercooled water in simulations of clouds results in excessive absorbed SW radiation over the midlatitude ocean compared to observations, especially the Southern Ocean, and this causes biases in radiative effects, and therefore CS, in climate models (Trenberth and Fasullo, 2010). Kay et al. (2016) showed with a climate model that these biases are reduced when more supercooled water is included.

In this chapter the impacts from changes in surface albedo, water vapour and cloud cover fraction on CS, and how CS and the strengths of feedbacks associated with changes in theses three climate variables are affected when albedo of clouds are taken into account, are presented. Since cloud albedo that interacts with the climate system has been incorporated, the model has been re-tuned, which means that some of the parameters

Table 5.1: Parameters used in the model. All parameters are global means, and surface is averaged over land and ocean. The paramters not listed here have the same values as in Chapter 4 and are listed in table 4.2

Parameter	Description	Value	Unit
α_s	Albedo for ice free surface	0.10	-
α_s	Albedo for ice covered surface	0.71	-
α_{cl}	Albedo for liquid water clouds	0.71	-
α_{ci}	Albedo for ice clouds	0.25	-
γ^c_{LW}	Emissivity for clouds	0.67	-
K^a	Diffusion constant for atmosphere	3.96×10^6	$m^2 s^{-1}$
K^s	Diffusion constant for surface	8.84×10^5	$m^2 s^{-1}$

in the new version of the model have values that differ from those in the version of the model presented in Chapter 4 (those parameters are listed in Table 5.1). The parameters are tuned so that the EBM simulated surface temperature, atmospheric temperature, meridional heat transport, total column water vapor, cloud cover fraction, lapse rate and latent heat flux agree with those from analyses or observations (see Figure 5.1). The surface temperature is slightly too high in the low latitudes. This is because the cloud albedo is set low, which allows more SW radiation to reach and warm the surface. The albedo for ice cloud is purposely set low in the tuning, so that the difference between ice cloud albedo and water cloud albedo is larger, and therefore the changes becomes more pronounced, which makes the analysis clearer. Since this is a "thought experiment" this is not considered to be an issue. Ice cloud albedo is here set to 0.25 and water cloud albedo is set to 0.71.

Figure 5.2 shows the different radiative flux components in the EBM. Considering the simplicity of the EBM, the agreement with values from Wild et al. (2013) is very good.

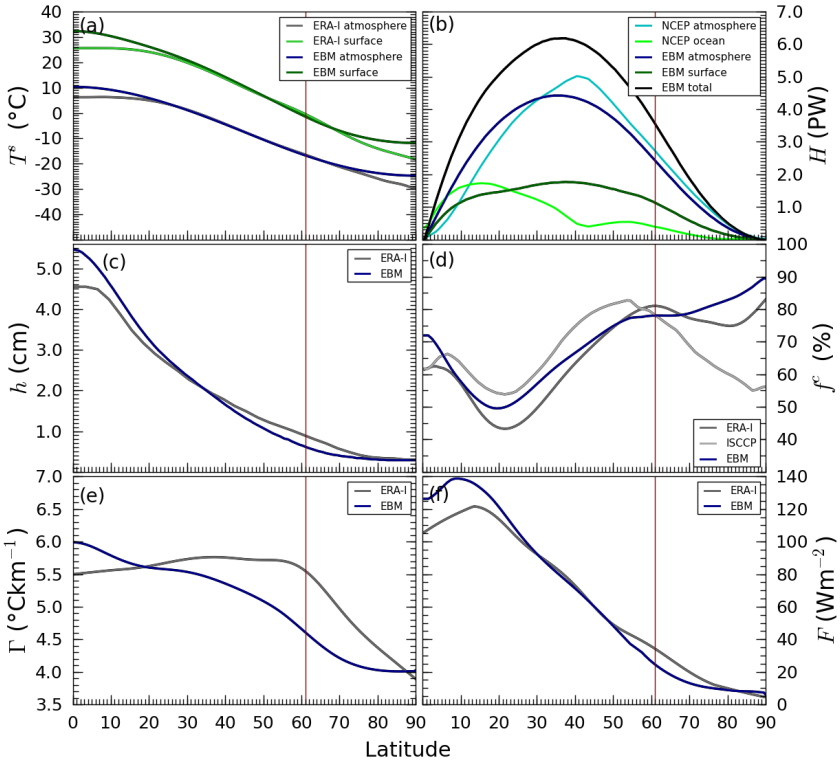

Figure 5.1: Output from the reference run simulated with 380 ppm CO_2, and compared to zonal mean 1979-2015 ERA-I, 1985-1989 NCEP and 1983-2009 ISCCP data. **(a)** Surface and atmospheric temperatures. **(b)** Ocean, atmospheric and total heat transport. **(c)** Total column water vapor. **(d)** Cloud cover fraction. **(e)** Lapse rate (averaged from surface to 650 hPa). **(f)** Latent heat flux.

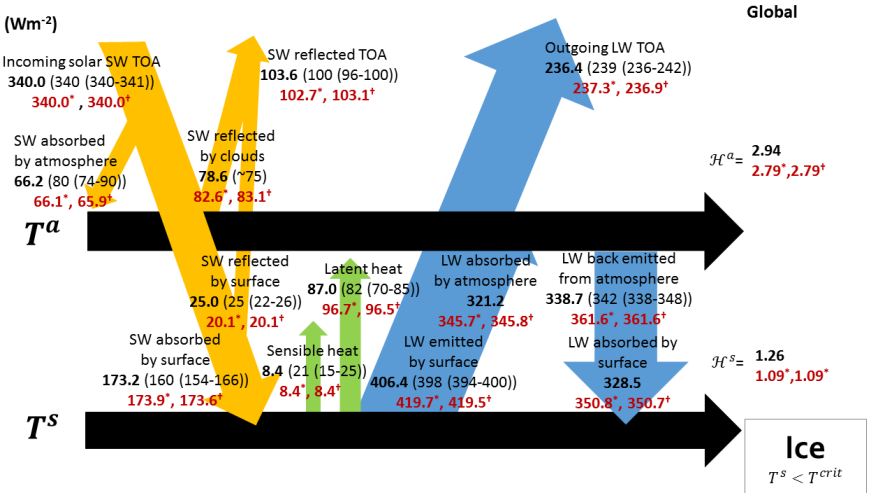

Figure 5.2: Schematic of the radiative fluxes in the EBM. Values shown in black bold text are output from our EBM run with 380 ppm CO_2,while values shown in brackets are from Wild et al. (2013). Red bold numbers denoted with a $\star$ are output from the EBM run with 760 ppm CO_2 and with cloud albedo prescribed, while red bold numbers denoted with a † are output from the EBM with cloud albedo activated. All values are in Wm^{-2}.

5.3 METHODS

5.3.1 *The model*

The model used in this work is an extension of the EBM presented and thoroughly described in Chapter 4. Here a brief description of the model is provided. For further details see Chapter 4. As mentioned in Chapter 4, the EBM developed during this PhD has a surface level (averaged over land and ocean), an atmospheric layer (representative of 650 hPa) extending from that surface to the top of the atmosphere, and a latitudinal resolution of 1°. The transport of heat across latitudes is represented by turbulent flow (diffusion), with a contribution from mean flow (advection) in low latitudes within the Hadley cell where the rotation of the Earth, and therefore baroclinic instability, becomes less important (see Chapter 4). This EBM also has a simple radiation scheme that takes into account the feedbacks from surface albedo, water vapour and cloud cover fraction. In this new version of the EBM, the feedback from cloud albedo, or reflectivity of clouds, is also included.

The differences in the model presented in this chapter compared to the version of the model presented in Chapter 4 lie in the SW^s and SW^a terms in Eqs. 4.1a and 4.1b. In Chapter 4, the albedo of clouds (α_c) in Eqs. 4.5a and 4.5b, was set to a constant. Here, α_c is calculated as a simple function of the approximate temperature of the top of the clouds in the model (T^c),

$$\begin{aligned}
\alpha_c &= \alpha_{cl} && T^c \geqslant T^A \\
\alpha_c &= \alpha_{cl} - (\alpha_{cl} - \alpha_{ci}) \\
&\quad \times (T^c - T^A)/(T^B - T^A) && T^A \geqslant T^c \geqslant T^B \\
\alpha_c &= a_{ci} && T^c \leqslant T^B
\end{aligned}$$

where α_{cl} is the albedo for liquid clouds (set to 0.71), α_{ci} is the albedo for ice in clouds (set to 0.25), T^A is the temperature at which the transition from liquid water to mixed phase and supercooled water takes place, and T^B is the temperature at

which the transition from mixed phase and supercooled water to ice crystals occur in the clouds. Kay et al. (2016) tested the sensitivity of T^A on the amount of SW radiation absorbed by the Southern Ocean, by using two different values, $-5°C$ and $-20°C$. In this work T^A is set to $-5°C$. Here T^B is set to $-48°C$, chosen to enhance the variation, so that the effects of changes in cloud temperature will become clear in the simulations (see Fig. 5.3).

As can be seen in Fig. 5.3 the temperature at the cloud top is cooler in the low latitudes compared to the high latitudes. This is because in the low latitudes, where the surface temperature is relatively high, there are strong vertical air motions that cause rapid cooling of air, and produce larger droplets when water condenses, compared to slow cooling associated with weaker vertical motions. Large droplets fall more rapidly than small droplets, and collide with other droplets, merging into larger droplets. Heat that is released when water condenses causes very rapid ascent of large air parcels, capable of forming clouds that extend into the upper troposphere where the colliding droplets freeze. This happens e.g. in stormy weather, and also explains the large fraction of ice clouds in the low latitudes where strong vertical motion takes place as a result of high surface temperatures and strong fluxes of latent heat. The processes just mentioned are too complex to include in a simple EBM such as the one presented here. The EBM presented in this thesis has a very simple vertical structure, and to take several vertical levels of clouds into account would not be possible without adding a significant amount of complexity to the model. The amount of SW radiation that is reflected by clouds depends on the properties of clouds at different levels in the atmosphere. However, at the top of the atmosphere, the properties of the top of high level clouds have the greatest impact on the SW radiation associated with clouds. The phase of the water in clouds depends on the temperature. The cloud top temperature T^c in the model presented here is calculated as follows,

$$T^c = T^a - \Gamma(z^c - z^{650\text{hPa}}) \tag{5.1}$$

where Γ is the lapse rate, z^c is the altitude of the cloud top (in km) and z^{650hPa} is the altitude at 650 hPa (in km). The altitude at the cloud top does not change with changing climate, and is calculated with the following expression,

$$z^c = a(b - (x \times x)^b) \tag{5.2}$$

where $x = \sin\phi$, ϕ is the latitude and the constants $a = 8.9$, $b = 2.0$ and $c = 1.8$ are tuned so that the EBM simulated cloud top altitude approximately agrees with the cloud top altitude from Hagihara et al. (2014). The cloud top temperature also regulates the emission of LW radiation to space. The emission temperature from clouds is corrected with a factor of 0.94, chosen so that the EBM simulated surface and atmospheric temperatures agree with ERA-I temperatures. The EBM simulated cloud top temperature and altitude for the simulation with 380 ppm CO_2 is displayed in Fig. 5.3. The horizontal lines in panel (a) in Fig. 5.3 show the temperatures where transition from water droplets to a mix of water and ice cloud occur (-5°C), and where the transition from mixed phase to total glaciation occurs (-48°C).

5.3.2 *Feedbacks*

When a forcing is applied to the climate system, the system responds by altering the radiative fluxes. It has been shown that there is a linear relation between the radiative response of the system at the top of the atmosphere (TOA) and the associated surface temperature change. For a climate system where all feedbacks are supressed, a climate sensitivity parameter, λ_0, can be defined as (Colman, 2003; Roe, 2009),

$$\lambda_0 = \frac{\Delta R_F^{TOA}}{\Delta T_0^s} \tag{5.3}$$

where ΔR_F^{TOA} is the perturbation in TOA radiative flux due to a forcing, and ΔT_0^s is the corresponding change in surface temperature. When feedback processes are added to the perturbed climate system, the radiative perturbation is either amplified or

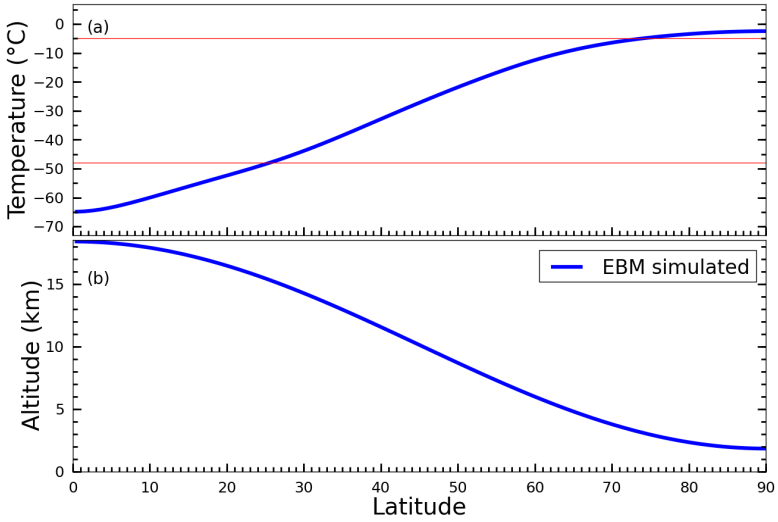

Figure 5.3: Cloud top **(a)** equilibrium temperature and **(b)** altitude. The red horizontal lines show the temperatures where the transition from ice phase to mixed phase and mixed phase to water vapour occur.

damped, and the new equilibrium surface temperature can be written

$$\begin{aligned} \Delta T^s &= \frac{1}{\lambda_0}(\Delta R_F^{TOA} + \sum_i^{nrf} \Delta R_i^{TOA}) \\ &= \frac{1}{\lambda_0}(\Delta R_F^{TOA} + \sum_i^{nrf} \lambda_i \Delta T^s) \end{aligned} \tag{5.4}$$

where nrf is the number of feedbacks included, R_i^{TOA} is the perturbation in radiative flux at TOA associated with the added feedbacks, and λ_i is the feedback factor for climate variable i. The final surface temperature change can then be expressed as (Colman, 2003; Roe, 2009),

$$\Delta T^s = \frac{\Delta T_0^s}{1 - \frac{1}{\lambda_0}\sum_i^{nrf} \lambda_i} \tag{5.5}$$

The climate feedback strength λ_i can then be obtained from Eq. 5.5, without explicitly having to calculate the R_F^{TOA}.

Climate sensitivity and the climate feedback factors can be calculated in different ways. Equilibrium climate sensitivity is usually defined as the change in surface temperature following a doubling of atmospheric CO_2 concentrations, after the climate system has readjusted to an equilibrium state. The climate sensitivity parameter is then calculated according to Eq. 5.4 or Eq. 5.5 from an equilibrium state. Estimates of equilibrium climate sensitivities are rare since the GCMs, due to the long response time scales of the deep ocean, need to be run for hundreds to thousands of years to reach full equilibrium (Li, 2012). To get around the requirement of having to run the model to equilibrium, model output for evolving transient conditions is sometimes used. The climate response parameter is then determined by regressing $R_i^{TOA}(t)$ against $T_i^s(t)$ where t is the timestep from the initial perturbation (Gregory et al., 2004). The slope is the effective climate response parameter and the intercept with R_i^{TOA} is F. In this work the EBM is always run to equilibrium, and the climate sensitivity is therefore always the equilibrium climate sensitivity.

Independent of the choice of method used to project CO_2-induced changes in temperature after the climate system has adjusted to a new equilibrium state, the concept of λ is associated with difficulties and uncertainties. For example, λ depends on the timescales at which feedbacks respond to the forcing. Gregory et al. (2004) showed that in a simulation where a GCM is run to equilibrium, the temperature change slows down when approaching the equilibrium state, when the ocean heat uptake is the major contributor to the change in temperature. Other responses, for example responses related to clouds, happen on very short timescales, which means that there will be a greater change in temperature during the time, linked to readjustment of clouds. The assumption that λ is linear is probably not completely true on longer timescales (Gregory et al., 2004). One reason why the linear approximation is still widely used is its simplicity, convenience and lack of alternatives (Knutti and Rugenstein, 2015).

5.4 CLIMATE SENSITIVITY FOR A DOUBLING OF CO_2

The EBM was run first with 380 ppm and then with 760 ppm atmospheric CO_2 concentration, with different feedbacks activated or disabled by prescribing the associated model variables, similar to Chapter 4. In addition, the EBM was run with cloud albedo (α_c) feedback activated or disabled, for all combinations of feedbacks. In this chapter the full feedback simulation is the simulation where surface albedo (α_s), water vapour (WV) and cloud cover (f^c) feedbacks are simultaneously activated, and the EBM is run with 380 ppm CO_2. The reference run is referred to as the full feedback simulation with cloud albedo feedback activated.

To make comparison between temperature changes (due to increased CO_2 loading) for different simulations easier, gain factors, G_g (for global temperature changes), G_{eq} (for temperature changes in the equatorial regions) and G_p (for changes in the polar regions), were introduced. The gain factors are simply calculated as the fraction between the surface temperature changes (due to increased CO_2 concentrations) from simulations with activated α_c feedback ($\Delta T^s_{int\alpha_c}$) and from simulations with α_c prescribed with values from the reference simulation ($\Delta T^s_{pre\alpha_c}$),

$$G = \frac{\Delta T^s_{int\alpha_c}}{\Delta T^s_{pre\alpha_c}} \tag{5.6}$$

A G that is larger than one implies that the cloud albedo feedback amplifies the surface warming, while a G that is less than one means that the cloud albedo feedback damps the surface warming.

5.4.1 *Global temperature changes*

For a doubling of CO_2, the global mean temperature change ΔT^s_g is increased for all simulations (see panel (a) in Fig. 5.4, and Table 5.2). When the cloud albedo is activated this increase in ΔT^s_g is reduced for the simulation where surface albedo, water

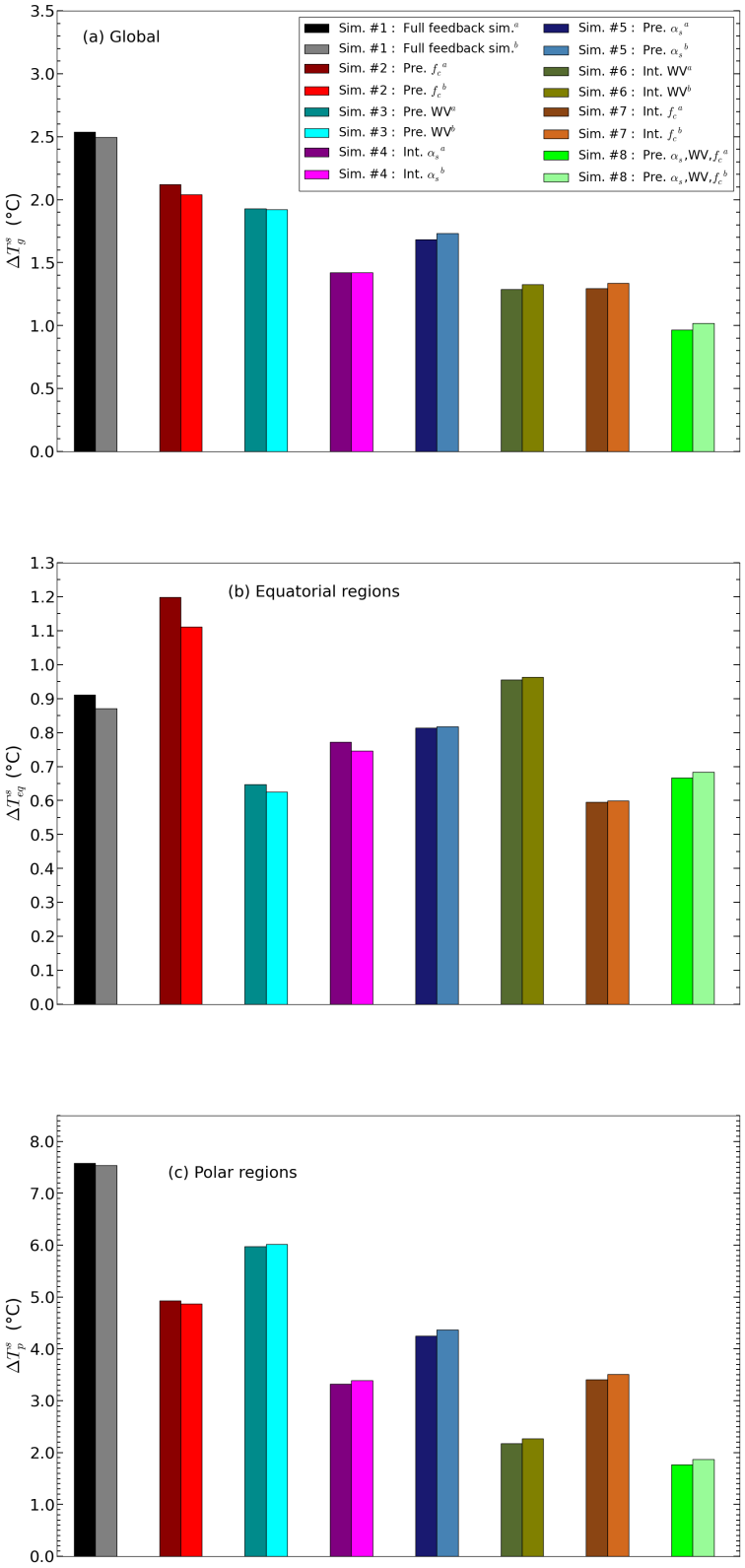

Figure 5.4: Equilibrium surface temperature changes for a doubling of CO_2, for all eight combinations of simulations, for simulations with [a]prescribed cloud albedo, [b]interactive cloud albedo. Global mean **(a)**, equatorial regions **(b)**, polar regions **(c)**.

Table 5.2: Changes in global mean temperatures for a doubling of CO_2 concentration, for simulations with cloud albedo that changes with changing temperature (Int. α_c) and simulations with prescribed cloud albedo (Pre. α_c). The global mean gain factors G_g are also listed.

				ΔT_g^s (°C)		
Sim.#	α_s	WV	f^c	Int. α_c	Pre. α_c	G_g
1	On	On	On	2.495	2.537	0.983
2	On	On	Off	2.040	2.121	0.962
3	On	Off	On	1.921	1.928	0.996
4	On	Off	Off	1.422	1.422	1.000
5	Off	On	On	1.734	1.684	1.030
6	Off	On	Off	1.327	1.287	1.031
7	Off	Off	On	1.337	1.296	1.032
8	Off	Off	Off	1.021	0.968	1.055

vapour and cloud cover interact (simulation #1) and the simulation with prescribed cloud cover, and where surface albedo and water vapour interact (simulation #2). The temperature increase is very small for the simulation where water vapour is prescribed (simulation #3), unchanged for the simulation where only the surface albedo is activated (simulation #2), and enhanced for simulations #5, 6, 7 and 8. This means that the global mean gain factor, G_g, is smaller than one for simulation # 1, 2, and 3, equal to one for simulation #4 and larger than one for simulation #5, 6, 7 and 8 (see Table 5.2). On a global scale, of all possible combinations of feedbacks, the full feedback simulation (simulation #1), with α_c prescribed, is found to have the greatest surface temperature change (2.537 °C) for a doubling of CO_2 concentrations (Fig. 5.4 and Table 5.2). The increase in ΔT_g^s is slightly reduced, to 2.495 °C, when the α_c feedback is activated. This gives a G_g of 0.983.

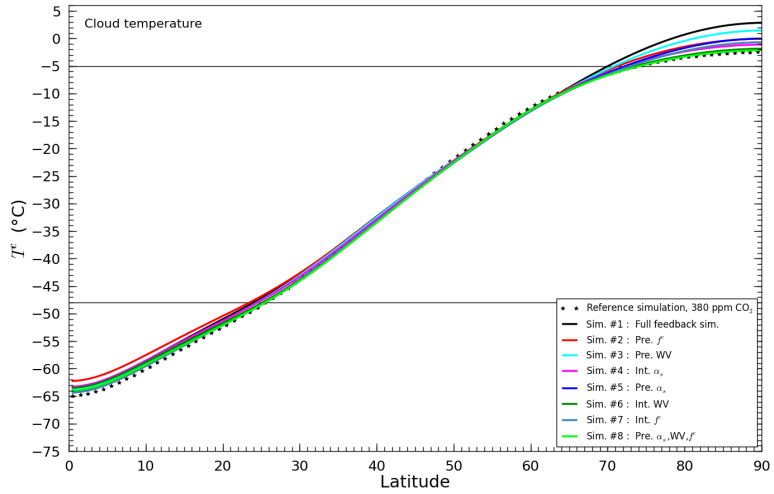

Figure 5.5: Cloud top temperature for EBM simulations with 760 ppm CO_2, for all eight possible combinations of activated feedbacks, with cloud albedo feedback activated for all simulations.

On a global scale, increased cloud top temperatures are found for all simulations for a doubling of CO_2, even though there is a decrease in cloud top temperatures the regions between 50° to 60° S/N (see Fig. 5.5 and Table 5.3). The exceptions are the simulations where the cloud cover feedback is activated and surface albedo and water vapour is prescribed (simulation #7) and the simulation where surface albedo, water vapour and cloud cover are prescribed (simulation #8, Table 5.3). An increase in cloud temperature gives a larger fraction of water droplets (compared to ice crystals) in the cloud. Since water droplets have higher albedo compared to ice crystals, in this simple EBM the albedo of clouds increase (see panel (a) in Fig. 5.6). This means that for a doubling of CO_2, clouds with higher albedo reflect SW radiation more efficiently. However, the amount of SW radiation that is reflected from clouds does not only depend on the albedo of the cloud, but also on the size of the area from which the SW radiation is reflected, i.e. the amount of clouds that cover the sky.

Table 5.3: Changes in global mean cloud top temperature (T_g^c), SW radiation reflected from clouds (SW_g^c) and LW radiation emitted from the atmosphere to the surface (LW_g) for a doubling of CO_2 concentration.

				ΔT_g^c		ΔSW_g^c		ΔLW_g	
Sim.#	α_s	WV	f^c	Int. α_c	Pre. α_c	Int. α_c	Pre. α_c	Int. α_c	Pre. α_c
1	On	On	On	0.739	0.794	4.397	3.979	22.524	22.693
2	On	On	Off	1.035	1.220	0.435	0.000	18.062	18.686
3	On	Off	On	0.480	0.506	4.157	3.866	16.265	16.209
4	On	Off	Off	0.558	0.594	0.130	0.000	11.714	11.753
5	Off	On	On	0.135	0.074	3.286	3.574	18.616	18.392
6	Off	On	Off	0.3333	0.270	0.183	0.000	14.445	14.217
7	Off	Off	On	-0.040	-0.066	2.924	3.276	13.826	13.727
8	Off	Off	Off	-0.101	0.000	-0.313	0.000	10.306	10.084

The reduction in surface temperature in simulation #1 when the cloud albedo feedback is activated is associated with the increase in SW radiation reflected from clouds (from 3.979 Wm^{-2} to 4.397 Wm^{-2}, see Table 5.3). There is a decrease in cloud top temperature change (from 0.794 to 0.739°C, Table 5.3) and therefore higher albedo, when the cloud albedo feedback is activated. The increase in cloud reflected SW radiation in simulation #1 is caused by increasing cloud cover fraction.

For a doubling of CO_2, there is an increase in SW radiation that is reflected from clouds for all simulations when cloud albedo is prescribed. This is because there is an increase in cloud cover fraction for all simulations (where the cloud cover fraction is activated, i.e. simulations #1, 3, 5 and 7), but no change in cloud albedo which gives a net increase in cloud reflected SW radiation. When the cloud albedo is activated there is a decrease in net cloud reflected SW radiation for the simulation where surface albedo, water vapour and cloud cover fraction are prescribed (simulation #8, -0.313 Wm^{-2}), due to a decrease in global mean cloud top temperature (-0.101 °C, leading to a lower albedo) and no change in cloud cover fraction (see Table 5.3).

Cloud reflected SW radiation has a cooling effect on the surface temperature. There is an increase in net SW radiation reflected from clouds for simulations #1, 2, and 3 when the cloud albedo feedback is activated, which dampens the surface temperature increase (see Figure 5.4 and Table 5.2). There is also an associated decrease in LW radiation emitted back to the surface from the atmosphere (Table 5.3).

In this simple EBM the cloud emissivity is set to 0.66, and the emissivity for CO_2 and water vapor is estimated to be 0.24 for the reference simulation, when calculated from Eq. 4.11. Because of the higher emissivity in clouds compared to clear sky, clouds emit more LW radiation back to the surface. With increasing cloud cover, not only does the cloud reflected SW radiation increase, but the cloud emitted LW radiation also in-

creases (see Table 5.3 and Figure 5.7).

There is no change in surface temperature for the simulations where the surface albedo feedback is active and water vapour and cloud cover are prescribed (simulation #4) when cloud albedo feedback is activated. This is a result of increasing SW radiation reflected from clouds (from 0.000 to 0.130 Wm^{-2}) which is offset by decreasing LW radiation backemitted to the surface, from 11.753 to 11.714 Wm^{-2}. The increase in LW radiation is caused by increased absorption of SW radiation by the surface, due to a shift of the ice edge towards higher latitudes, and therefore exposure of a larger, darker surface area. The warmer surface emits more LW radiation to the atmosphere. The increased amount of LW radiation that is absorbed by the atmosphere warms the atmosphere, which in turn emits more LW radiation back to the surface.

In the simulation where surface albedo is prescribed and the water vapour and cloud cover feedbacks are activated (simulation #5), there is an increase in LW radiation emitted back to the surface (from 18.392 to 18.616 Wm^{-2}) when the cloud albedo feedback is activated (Table 5.3). Even though there is an increase in cloud top temperature (from 0.074 to 0.135 °C) which gives a larger cloud albedo, there is a decrease in SW radiation reflected by clouds (from 3.574 to 3.286 Wm^{-2}), because of a decrease in cloud cover fraction when cloud albedo is activated. The enhanced LW radiation and decrease in SW radiation results in a net warming of the surface when the cloud albedo is active (see panel (a) in Fig. 5.4 and Table 5.2).

The warming effect from increasing LW radiation (from 14.217 to 14.445 Wm^{-2}) is stronger than the cooling effect from increasing SW radiation reflected by clouds (from 0.000 to 0.183 Wm^{-2}), resulting in a net warming of the surface (from 1.121 to 2.040 °C) when the cloud albedo is activated in the simulation where water vapour is active and surface albedo and cloud cover are prescribed (simulation #6).

The decrease in cloud top temperature for a doubling of CO_2 (-0.066 °C) found for the simulation where only the cloud cover feedback is active (simulation #7) gives a smaller cloud albedo, resulting in more SW radiation that reaches and warms the surface compared to the reference simulation. The cloud top temperature decreases slightly (to -0.040 °C), when the cloud albedo feedback is activated. However the net SW flux reflected from clouds is larger when cloud albedo is prescribed (3.276 Wm^{-2} compared to 2.924 Wm^{-2} when cloud albedo feedback is activated) because of a larger increase in cloud cover fraction. The smaller increase in cloud reflected SW radiation and larger increase in LW radiation when cloud albedo feedback is activated (Table 5.3) result in a net increase in surface temperature (see Fig.5.4 and Table 5.2).

There is a global mean decrease in cloud top temperature for the simulation where surface albedo, water vapour and cloud cover interact, and the albedo feedback is activated (simulation #8, -0.101 °C, see Table 5.3), giving a smaller cloud albedo. This gives a net decrease in SW radiation reflected from clouds. The decrease in net SW radiation reflected by clouds allows more SW radiation to be absorbed by the surface, and increase the surface temperature. The LW radiation that is emitted from the atmosphere to the surface is enhanced when climate variables interact (see Table 5.3 and also Chapter 4), which result in increased surface warming. When all three climate variables are prescribed, the increase in LW radiation is relatively small, 10.084 Wm^{-2} when cloud albedo is prescribed, and 10.306 Wm^{-2} when cloud albedo is activated (see Table 5.3), resulting in a relatively small surface temperature increase for a doubling of CO_2 (0.968 °C when cloud albedo is prescribed and 1.021 °C when cloud albedo feedback is active, Fig. 5.4 and Table 5.3).

The strongest effect from the cloud albedo feedback, on a global scale, is found for the simulation where surface albedo, water vapour and cloud cover fraction are prescribed, with a gain factor or 1.055 (simulation #8, Table 5.2). The smallest effect is found for the simulation where surface albedo is active and

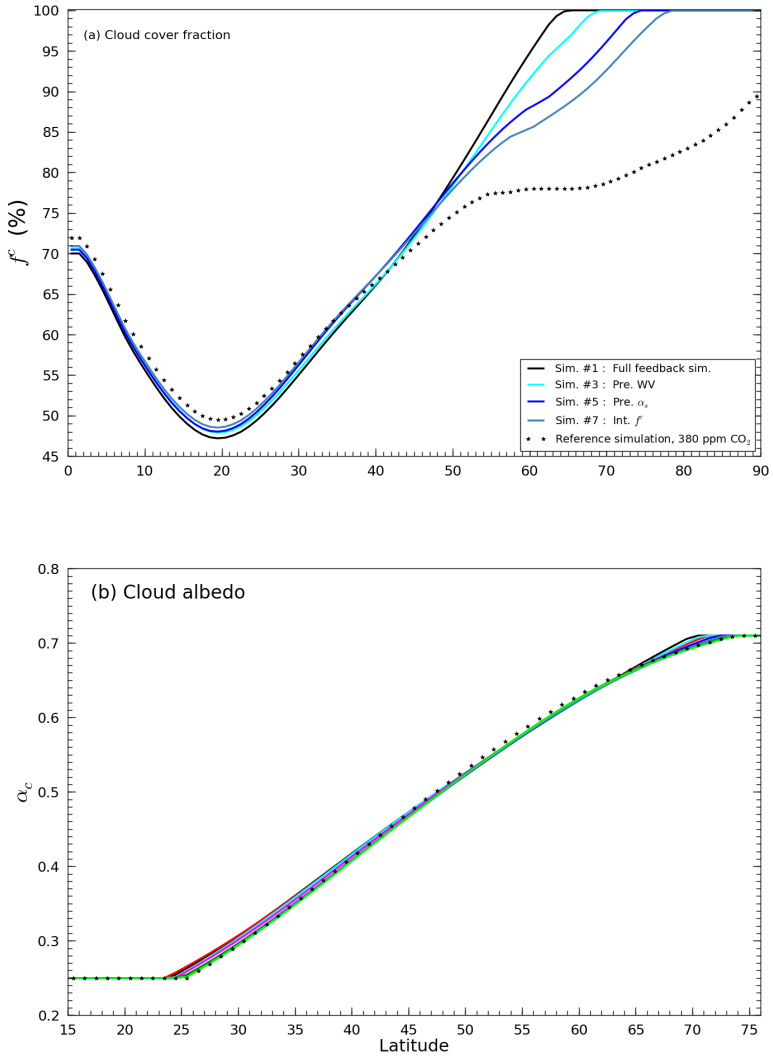

Figure 5.6: Zonal mean **(a)** cloud cover fraction and **(b)** cloud albedo for EBM simulations with 760 ppm CO_2, for all eight possible combinations of activated feedbacks, and with cloud albedo feedback activated for all simulations.

Table 5.4: Changes in equatorial (0°-30° S/N) mean temperatures for a doubling of CO_2 concentration, for simulations with cloud albedo that changes with changing temperature (Int. α_c) and simulations with prescribed cloud albedo (Pre. α_c). The low latitude mean gain factors G_{eq} are also listed.

				ΔT^s_{eq} (°C)		
Sim.#	α_s	WV	f^c	Int. α_c	Pre. α_c	G_{eq}
1	On	On	On	0.871	0.912	0.955
2	On	On	Off	1.111	1.199	0.927
3	On	Off	On	0.625	0.647	0.966
4	On	Off	Off	0.747	0.772	0.968
5	Off	On	On	0.818	0.814	1.005
6	Off	On	Off	0.963	0.956	1.007
7	Off	Off	On	0.600	0.596	1.007
8	Off	Off	Off	0.684	0.667	1.025

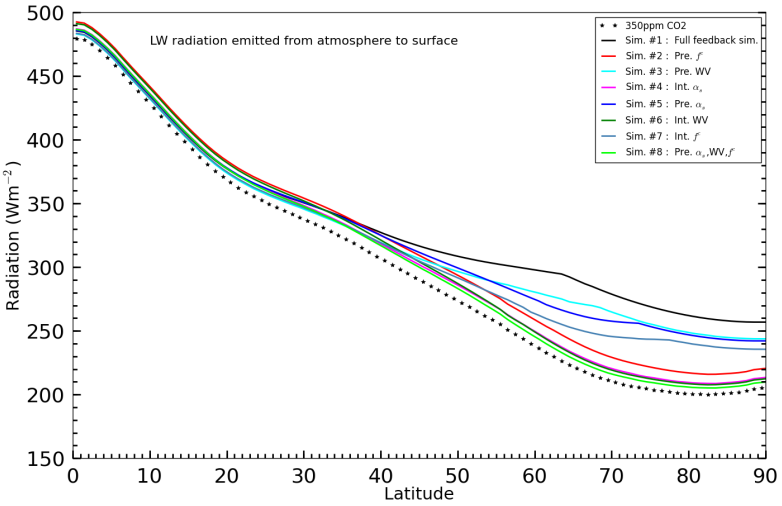

Figure 5.7: LW radiation emitted from the atmosphere to the surface for EBM simulations with 760 ppm CO_2, for all eight possible combinations of activated feedbacks, with cloud albedo feedback activated for all simulations.

water vapour and cloud cover fraction are prescribed, with a gain factor of 1.000 (simulation #4, Table 5.3).

5.4.2 *Temperature changes in low and high latitudes*

In the lower latitudes (here defined as 0° to 30° S/N) for a doubling of CO_2, a damping of the surface temperature when the cloud albedo feedback is activated is found for simulations #1, 2, 3 and 4 (the simulations with prescribed surface albedo). Simulations with cloud cover feedback activated and surface albedo prescribed (simulations #1 and 3) give decreases in cloud reflected SW radiation for a doubling of CO_2. This is because of decreases in cloud cover in the low latitudes (see panel (a) in Fig. 5.6).

The largest surface temperature change is found for the simulation with prescribed cloud cover fraction, and activated surface albedo and water vapor feedbacks (simulation #2, 1.199 °C for

the simulation when cloud albedo is prescribed, see panel (b) in Fig. 5.4 and Table 5.4). The temperature change is dampened when cloud albedo is activated, with an increase of 1.111 °C, which gives a gain factor G_{eq} of 0.927. The damping effect is due to an increase in reflected SW radiation (from 0.000 to 0.625 Wm^{-2}), and also a decrease in LW radiation emitted from the atmosphere to the surface (Table 5.5).

The damping effect is slightly weaker for the full feedback simulation (#1) in the lower latitudes, with a G_{eq} of 0.955, after a small temperature decrease from 0.912 °C when the cloud albedo is prescribed to 0.871 °C when the cloud albedo feedback is activated (see panel (b) in Fig. 5.4 and Table 5.4). This damping effect is caused by increasing reflected SW radiation, from -2.324 Wm^{-2} when cloud albedo is prescribed to -1.750 Wm^{-2} when cloud albedo is activated (Table 5.5). The LW radiation is also reduced, from 8.397 to 8.263 Wm^{-2}, due to a decrease in cloud cover.

A decrease in low latitude cloud cover is found for all simulations, but is greatest for the simulation where surface albedo, water vapor and cloud cover interact (simulation #1, see panel (a) in Fig. 5.5). In the low latitudes, the decrease in cloud cover dampens the effect from increasing albedo caused by increasing cloud temperature.

In the low latitudes, the simulation with all three climate variables prescribed (simulation #8) gives the largest G_{eq} (1.025), associated with a ΔT^{s}_{eq} of 0.667 °C when cloud albedo is prescribed, and 0.684 °C with the cloud albedo feedback active (see panel (b) in Fig. 5.4 and Table 5.4).

The effect from the cloud albedo feedback on the surface temperature is found to be greatest in the higher latitudes (here defined as 60° to 90° S/N) with gain factors G_p ranging from 0.988 for the simulation with surface albedo and water vapour active and cloud cover fraction prescribed (simulation #2) to 1.059 for the simulation with surface albedo, water vapour and cloud cover prescribed (simulation #8, Table 5.7). In the high

Table 5.5: Changes in equatorial mean cloud top temperature (T^c_{eq}), SW radiation reflected from clouds (SW^c_{eq}) and LW radiation emitted from the atmosphere to the surface (LW_{eq}) for a doubling of CO_2 concentration.

				ΔSW^c_{eq}		ΔLW_{eq}	
Sim.#	α_s	WV	f^c	Int. α_c	Pre. α_c	Int. α_c	Pre. α_c
1	On	On	On	-1.750	-2.324	8.263	8.397
2	On	On	Off	0.625	0.000	14.591	15.363
3	On	Off	On	-1.264	-1.670	5.316	5.325
4	On	Off	Off	0.357	0.000	9.035	9.176
5	Off	On	On	-1.444	-1.514	8.897	8.979
6	Off	On	Off	0.189	0.000	13.192	13.117
7	Off	Off	On	-1.043	-1.066	6.003	6.094
8	Off	Off	Off	0.098	0.000	8.616	8.510

Table 5.6: Changes in polar mean SW radiation reflected from clouds (SW_p^c) and LW radiation emitted from the atmosphere to the surface (LW_p) for a doubling of CO_2 concentration.

				ΔSW_p^c		ΔLW_p	
Sim.#	α_s	WV	f^c	Int. α_c	Pre. α_c	Int. α_c	Pre. α_c
1	On	On	On	27.798	27.630	64.061	64.396
2	On	On	Off	0.055	0.000	26.730	27.000
3	On	Off	On	26.182	25.971	50.895	50.649
4	On	Off	Off	-0.062	0.000	18.072	17.888
5	Off	On	On	22.177	22.211	46.086	45.402
6	Off	On	Off	-0.188	0.000	17.114	16.735
7	Off	Off	On	19.400	19.657	37.194	36.773
8	Off	Off	Off	-0.310	0.000	13.979	13.638

latitudes the large increase in cloud cover, i.e. the area of which SW radiation is reflected, enhances the increase in cloud albedo when the cloud albedo feedback is activated. A net surface warming is found for all simulations when cloud albedo feedback is activated (panel (c) in Fig. 5.4). The exception is the simulation where surface albedo, water vapor and cloud cover feedbacks are activated (simulation #1), and the simulation where surface albedo and water vapor feedbacks are active and cloud cover is prescribed (simulation #2). For simulation #1 there is a small decrease in surface temperature, from 7.585 °C to 7.539 °C which gives a gain factor of 0.994 (see Table 5.3). For simulation #1, there is an increase in cloud reflected SW radiation, from 27.630 to 27.798 Wm^{-2}, when cloud albedo is activated (Table 5.6). This cools the surface. This cooling effect is enhanced by an increase in LW radiation, from 64.396 to 64.061 Wm^{-2} when cloud albedo feedback is active, due to a smaller increase in cloud cover fraction, which dampens the surface temperature change when cloud albedo is activated.

A decrease in polar cloud reflected SW radiation is found for the simulations with prescribed water vapor and cloud cover and with surface albedo feedback active (-0.062 Wm^{-2}, simulation #4), when the cloud albedo feedback is activated (Table 5.6). This has a warming effect on the surface temperature, since more SW radiation reaches the surface. Decreases in SW radiation reflected from clouds are also found for the simulation where only the water vapor and cloud albedo feedbacks are active (-0.188 Wm^{-2}, simulation #6) and the simulation where only the cloud albedo feedback is active (-0.310 Wm^{-2}, simulation #8).

There are complicated interactions between increasing cloud temperature (and resulting increasing cloud albedo), and LW radiation in the low latitudes. The cooling effect from increasing cloud albedo, due to increased CO_2 concentrations, is partly offset by enhanced LW radiation emitted from the atmosphere to the surface.

5.5 FEEDBACK STRENGTHS FOR A DOUBLING OF CO_2

The feedback strength, λ, for each of the eight simulations was calculated using to Eq. 5.5. The feedback strength associated with the planck feedback, λ_0, in Eq. 5.5 was calculated from the temperature change for a doubling of CO_2 concentrations for the simulation where α_s, WV and f^c are prescribed (simulation #8). Just as for the surface temperature change, to investigate the effects from the cloud albedo on the feedback strength, a gain factor, G_λ, was calculated as follows,

$$G_\lambda = \frac{\lambda_{int\alpha_c}}{\lambda_{pre\alpha_c}} \tag{5.7}$$

where $\lambda_{int\alpha_c}$ is the feedback strength calculated from Eq. 5.5 with T^s from simulations with cloud albedo that is allowed to change with changing temperatures within the model, and where $\lambda_{pre\alpha_c}$ is the climate sensitivity calculated with T^s from

Table 5.7: Changes in polar (60°-90° S/N) mean temperatures for a doubling of CO_2 concentration, for simulations with cloud albedo that changes with changing temperature (Int. α_c) and simulations with prescribed cloud albedo (Pre. α_c). The high latitude mean gain factors G_p are also listed.

				ΔT_p^s (°C)		
Sim.#	α_s	WV	f^c	Int. α_c	Pre. α_c	G_p
1	On	On	On	7.539	7.585	0.994
2	On	On	Off	4.872	4.932	0.988
3	On	Off	On	6.015	5.974	1.007
4	On	Off	Off	3.392	3.323	1.021
5	Off	On	On	4.371	4.247	1.029
6	Off	On	Off	2.270	2.179	1.042
7	Off	Off	On	3.508	3.407	1.030
8	Off	Off	Off	1.871	1.767	1.059

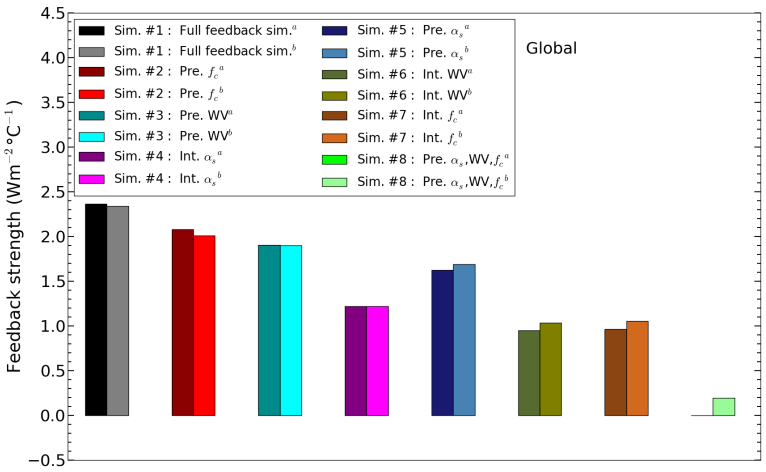

Figure 5.8: Climate feedback strengths for global mean temperature responses to a doubling of CO_2 in the atmosphere, for all eight combinations of feedbacks, for simulations with [a]prescribed cloud albedo, [b]interactive cloud albedo.

simulations where the cloud albedo is prescribed with values from the reference run.

According to our simulations, the largest λ is found for the simulations where there is interaction between two or more climate variables (simulations #1, 2, 3 and 5, see Fig. 5.8 and Table 5.8). For simulations with prescribed cloud albedo, the largest λ is found for the full feedback simulation (simulation #1, 2.365 $Wm^{-2}°C^{-1}$), followed by the simulation where the cloud cover is prescribed (simulation #2, 2.079 $Wm^{-2}°C^{-1}$), the simulation where the water vapor is prescribed (#3, 1.904 $Wm^{-2}°C^{-1}$) and the simulation where the surface albedo is prescribed (#5, 1.627 $Wm^{-2}°C^{-1}$) (see Fig. 5.8 and Table 5.8). For the single isolated feedback simulations, the case with the surface albedo feedback active and with water vapor and cloud cover prescribed (simulation #4), gives the largest climate feedback factor (1.221 $Wm^{-2}°C^{-1}$), followed by the simulation with only the cloud cover feedback active (simulation #7, 0.967 $Wm^{-2}°C^{-1}$) and the simulation with only water vapor feedback active (#6,

Table 5.8: Climate feedback parameters (λ) for a doubling of CO_2 concentration, for simulations with cloud albedo that changes with changing temperature (Int. α_c) and simulations with prescribed cloud albedo (Pre. α_c). The gain factors G_λ are also listed.

				λ ($Wm^{-2}°C^{-1}$)		
Sim.#	α_s	WV	f^c	Int. α_c	Pre. α_c	G_λ
1	On	On	On	2.340	2.365	0.989
2	On	On	Off	2.010	2.079	0.967
3	On	Off	On	1.898	1.904	0.997
4	On	Off	Off	1.222	1.221	1.001
5	Off	On	On	1.689	1.627	1.038
6	Off	On	Off	1.035	0.948	1.092
7	Off	Off	On	1.057	0.967	1.093
8	Off	Off	Off	0.195	0.000	-

0.948 $Wm^{-2}°C^{-1}$). When the cloud albedo feedback is activated, an amplifying effect on the climate feedback factor is found for the simulations with prescribed surface albedo (simulations #5, 6, 7 and 8), while a damping effect is found for simulations where the surface albedo feedback is active (simulations #1, 2 and 3). The simulation where only the surface albedo feedback is active (#4) gives a very small increase in the climate feedback factor (see Fig. 5.8 and Table 5.8). The simulation with only surface albedo feedback active has a gain factor G_λ of 1.001.

The simulations where the surface albedo is prescribed (simulations #5, 6, 7), respond more strongly to the activation of cloud albedo feedback compared to the simulations where the surface albedo feedback is activated (i.e. simulations #1, 2, 3 and 4). The largest increase in λ is found for the simulation with isolated cloud cover feedback (simulation #7) with a G_λ of

1.093, followed by the isolated water vapour feedback (simulation #6) with a G_λ of 1.092 and the coupled water vapor and cloud cover simulation (#5) with a G_λ of 1.038 (see Table 5.8).

The relatively small gain factor G_λ for simulations where the surface albedo is activated (simulations #1, 2, 3 and 4), compared to where surface albedo is prescribed (simulation #5, 6 and 7) indicates that surface albedo dampens the effect from cloud albedo on λ. Clouds and ice covered surface have similar albedos (in this EBM set to 0.71), so changes in clouds over ice covered surface will have little effect on the net SW radiation.

When cloud albedo is activated, there is a reduction in SW radiation reflected from clouds, from 3.574 to 3.286 Wm^{-2} for the simulation where surface albedo is prescribed (simulation #5), due to a decrease in cloud cover in the area where cloud albedo changes the most (see Fig. 5.6). A reduction in SW radiation is also found for the simulation with only cloud cover activated (from 3.276 to 2.924 Wm^{-2}, simulation #7, see Table 5.3). Surface albedo primarily affects surface SW fluxes, but also the LW radiation components. The combination of reduced SW radiation and a relative large increase in LW fluxes when cloud albedo is activated in simulation #5 and 7 gives a relatively large G_λ. This indicates that the cloud albedo affects the interaction between the SW and LW components.

5.6 DISCUSSION AND SUMMARY

In this chapter results from the EBM described in Chapter 4, extended with cloud albedo feedback, are presented. It is found that for a doubling of CO_2, on a global scale the activation of the cloud albedo feedback enhances the CO_2-induced surface temperature increase for simulations where the surface albedo is prescribed (simulations #5, 6, 7 and 8), and dampens the surface temperature increase in simulations where surface albedo feedback interacts with water vapour or/and cloud cover feedbacks (#1, 2 and 3). In the high latitudes (here defined as 60° to

90° S/N), the surface temperature increase is damped for the simulation where the surface albedo feedback interacts with water vapour (simulations #1 and 2), and is enhanced for the rest of the simulations. In the equatorial regions, the surface temperature warming for all simulations where the surface albedo feedback is activated is also dampened by activation of the cloud albedo feedback (simulations #1, 2, 3 and 4).

For a doubling of CO_2, the increase in temperature in clouds found for all simulations except for the simulation where surface albedo, water vapor and cloud cover are prescribed (simulations #8) and the simulation with only cloud cover feedback activated (#7), lead to higher cloud albedo, allowing less SW radiation to reach and warm the surface. The increase in cloud temperature in the lower most and higher most latitudes (defined by the latitudes poleward of where the critical temperature for cloud phase transformation T^A takes place, and equatorward of where T^B takes place, see Fig. 5.3) does not affect the cloud albedo in this model since the temperature is well below the critical temperature for transition from ice to water-ice mixed phase and from mixed phase to total water phase for all simulations. There are only two critical temperatures for phase transitions in the EBM presented in this chapter. Therefore the geographical distribution of changes in cloud albedo is also simplified. However, the results presented here give an indication of the importance of representing the reflectivity of clouds and changes of reflectivity of clouds correctly in climate models.

The results presented here indicate that the other feedbacks, i.e. surface albedo, water vapour and cloud cover feedbacks also impact the effects that cloud albedo has on the climate system. The cooling effect that cloud albedo has on the global mean surface temperature is enhanced for the simulation where surface albedo, water vapour and cloud cover interact (simulation #1), the simulation where the cloud cover fraction is prescribed (simulation #2), and the simulation where water vapor is prescribed (simulation #3).

In both high and low latitudes, a warming of the clouds is found, which results in increasing cloud albedo due to more water droplets in the cloud, which leads to a cooling of the surface temperature. However, there is also a competing effect from the warming related to the increase in LW radiation that is emitted from the atmosphere to the surface. When the LW radiation is smaller, e.g. when the interaction between positive feedbacks such as surface albedo, water vapour or cloud cover feedbacks are weaker, the effect from cloud albedo feedback becomes more important. Of the isolated feedback simulations cloud albedo has the greatest impact on the cloud cover feedback, followed by the water vapour and the surface albedo feedbacks.

The amplified climate feedback strength caused by the the cloud albedo feedback is greatest when the surface albedo is prescribed, due to a warming of the cloud temperature, and therefore increase in cloud albedo, especially in the high latitudes, in combination with increased LW radiation backemitted from the atmosphere to the surface.

According to the output from our EBM, the climate feedback strength for the full feedback simulation is $2.365\,\mathrm{Wm^{-2}{}^{\circ}C^{-1}}$ with an increase to $2.340\,\mathrm{Wm^{-2}{}^{\circ}C^{-1}}$ when the cloud albedo feedback is prescribed. This is very close to the feedback strength of $2.2\,\mathrm{Wm^{-2}{}^{\circ}C^{-1}}$ presented by Colman (2003). The feedback strength for the surface albedo from the work of Colman (2003) can be compared to our isolated α_s simulation. Our EBM simulated feedback strength for the isolated α_s simulation is $1.221\,\mathrm{Wm^{-2}{}^{\circ}C^{-1}}$ and is slightly increased to $1.222\,\mathrm{Wm^{-2}{}^{\circ}C^{-1}}$ when the cloud albedo feedback is activated. This is above the high end of the model range presented by Colman (2003), where the model mean for the surface albedo feedback strength is reported to be $0.36\,\mathrm{Wm^{-2}{}^{\circ}C^{-1}}$, with a model spread $0.75\,\mathrm{Wm^{-2}{}^{\circ}C^{-1}}$. The model mean feedback strength for surface albedo in the fifth assessment report from IPCC is $0.3\,\mathrm{Wm^{-2}{}^{\circ}C^{-1}}$, with values ranging from 0.2 to $0.4\,\mathrm{Wm^{-2}{}^{\circ}C^{-1}}$ (Flato et al., 2013). However, the

difference between λ for the full feedback simulation (simulation #1, 2.340 $Wm^{-2}°C^{-1}$) and λ for the simulation with locked surface albedo (simulation #5, 1.689 $Wm^{-2}°C^{-1}$) is 0.651 $Wm^{-2}°C^{-1}$, which is within the uncertainty range presented by Colman (2003). The difference in λ for the α_s feedback (i.e. 1.222 $Wm^{-2}°C^{-1}$ and 0.651 $Wm^{-2}°C^{-1}$) also points towards the non-linearities of the system (as also discussed in Chapter 4).

The feedback strength for water vapor simulated with the EBM presented here is 0.948 $Wm^{-2}°C^{-1}$ (increased to 1.035 $Wm^{-2}°C^{-1}$ when cloud albedo feedback is activated) which is just below the lower end of the combined feedback strength from water vapour and lapse rate reported by Colman (2003). Their model mean water vapour/lapse rate feedback strength is reported to be 1.37 $Wm^{-2}°C^{-1}$ with a model spread of 0.63 $Wm^{-2}°C^{-1}$. Our EBM simulated *WV* feedback strength is however very close to the sum of the lapse rate and water vapour feedback strengths of 0.95 $Wm^{-2}°C^{-1}$ as reported by Soden and Held (2006). In the fifth assessment report from IPCC, the model mean lapse rate feedback strength is -0.6 Wm^{-2}, and the model mean water vapour feedback strength 1.6 $Wm^{-2}°C^{-1}$ (Flato et al., 2013). The sum of the lapse rate and water vapour feedback strengths is 1.0 $Wm^{-2}°C^{-1}$, very close to our EBM simulated water vapour feedback strength.

The spread in model results is large for all feedback strengths, both in the work of Colman (2003) and in the IPCC report. The largest spread is found for the cloud feedback. In the work of Colman (2003) the model mean cloud feedback strength is 0.55 $Wm^{-2}°C^{-1}$, with a model range of 1.45 $Wm^{-2}°C^{-1}$. Even the sign differs between models. In the IPCC report the model mean for cloud feedback is 0.3 $Wm^{-2}°C^{-1}$, with model values from -0.4 to 0.5 $Wm^{-2}°C^{-1}$. Our EBM simulated feedback strengths for cloud cover is 0.967 $Wm^{-2}°C^{-1}$, within the uncertainty presented by Colman (2003), but higher than the upper values of the range presented by IPCC. The feedback strength for our EBM simulation where both the cloud cover and cloud albedo feedbacks are taken into consideration increases λ further, to

$1.057\,\mathrm{Wm}^{-2}{}^{\circ}\mathrm{C}^{-1}$. The difference between the feedback strength between the full feedback simulation (#1, 2.340) and the simulation with locked cloud cover fraction (#2, 2.010) is 0.330, which is much closer to the values reported in the literature. This also points towards the non-linearities of the system.

6

A PROBABILISTIC STUDY OF THE RETURN OF STRATOSPHERIC OZONE TO 1960 LEVELS

The research presented in this chapter has been peer reviewed and published in the scientific journal Geophysical Reserch Letters (see Ref. Södergren et al. 2016), and the text in the following sections (6.1 to 6.5) is a copy of that paper (with minor changes). Thereafter follows an Addendum, where the work presented in the published paper is further explained.

6.1 ABSTRACT

Anthropogenic emissions of greenhouse gases and ozone depleting substances are expected to continue to affect concentrations of ozone in the stratosphere through the 21st century. While a range of estimates for when stratospheric ozone is expected to return to unperturbed levels is available in the literature, quantification of the spread in results is sparse. Here, we present the first probabilistic study of latitudinally resolved years of return of stratospheric ozone to 1960 levels. Results from our 180 member ensemble, simulated with a newly developed simple climate model, suggest that the spread in return years of ozone is largest around 40° N/S and in the southern high latitudes, and decreases with increasing greenhouse gas emissions. The spread in projections of ozone is larger for higher greenhouse gas scenarios, and is larger in the polar regions than in the mid-latitudes, while the spread in ozone radiative forcing is smallest in the polar regions.

6.2 INTRODUCTION

Chemistry climate models (CCMs) are the tools most commonly used to project the future evolution of the ozone layer (Pawson, Steinbrecht et al., 2014). Uncertainties in projections of ozone arise due to a wide range of plausible future greenhouse gas (GHG) and ozone depleting substance (ODS) emissions scenarios, as well as differences between models (see Refs. Nowack et al. 2015; Eyring et al. 2010a,b; Charlton-Perez et al. 2010; Eyring et al. 2007). The complexity and resultant high computational costs of CCM simulations, however, precludes a thorough exploration of the uncertainty space.

Since the 1970s, anthropogenic emissions of ODSs have led to a global depletion of stratospheric ozone, most severe over Antarctica in late winter and spring. The Montreal Protocol, with its amendments and adjustments, has led to observed decreases in tropospheric concentrations of controlled ODSs which are expected to return to 1960 levels around the end of the 21st century (Carpenter, Reimann et al., 2014). The decline of ozone outside the polar regions has been reported to have ceased in the late 1990s, meeting the criterion for the first stage of ozone recovery (Chipperfield, Fioletov et al., 2007).

As atmospheric concentrations of ODSs decline, other factors, such as changes in the climate of the stratosphere due to ongoing emissions of GHGs, will increasingly influence stratospheric ozone (Eyring et al. 2010b; Bekryaev et al. 2010; Gauss et al. 2006; Shepherd and Jonsson 2008). Increasing concentrations of GHGs alter the abundances of stratospheric ozone through decreases in stratospheric temperatures which in turn affect temperature dependent chemical reactions (e.g. slowing of the $O_3 + O \rightarrow O_2$, see Sec. 2.3), through changes in hydrogen and nitrogen oxide chemistry, and through GHG-induced changes in transport (Eyring et al. 2006; Jonsson 2004). For example, GHG-induced radiative warming of the troposphere affects transport pathways of ozone, ozone precursors (nitrogen oxides, carbon monoxide and volatile organic compounds) and ODSs to the stratosphere. One such transport pathway is the Brewer Dobson circulation (BDC) (see Ref. Butchart 2014, and also Sec.

2.3 in this thesis) which globally redistributes ozone produced primarily in the tropical upper stratosphere. Changes in the BDC also affect the rate at which ODS photolyze. Simple climate models (SCMs) can be used as fast emulators of complex atmosphere-ocean general circulation models (AOGCMs) (Randall et al., 2007a). While a SCM cannot replace more sophisticated AOGCMs, it offers a complementary research tool that can synthesize and consistently integrate a range of uncertainties resulting from our imperfect knowledge of the climate system and of future emissions. To date, and to our knowledge, no SCM has incorporated an interactive stratosphere which has precluded the use of SCMs in diagnosing uncertainties in projections of stratospheric ozone.

Here we present a SCM that has been extended to include an interactive stratosphere, and its application to simulating the evolution of the ozone layer through the 21st century. To our knowledge, this is the first probabilistic study of the years of return of stratospheric column ozone (SCO) to 1960 levels.

6.3 METHODS

A new interactive SCM has been developed as an extension to the Model for Assessment of Greenhouse-gas Induced Climate Change (MAGICC) (Meinshausen et al. 2011b,a) SCM, briefly described in Sec. 3.2.1 in this thesis. In this new version of MAGICC, the radiative forcing (RF; downward minus upward flux at the tropopause) from stratospheric ozone couples simulated ozone changes to the climate system in the model. Resultant changes to surface temperatures, and thereby other components of MAGICC sensitive to surface temperature, affect stratospheric carbon dioxide (CO_2) concentrations and hence stratospheric temperatures which affect ozone chemistry. This two-way coupling is important for simulating SCO.

MAGICC generates an estimate of equivalent effective stratospheric chlorine (EESC, derived from chlorine and bromine) (Newman et al. 2007; Daniel et al. 1999) and CO_2 concentrations at the end of each model year. The estimated CO_2 and EESC

provide the inputs needed to simulate SCO and RF within MAGICC. A pattern scaling technique, previously applied to surface climate variables (Kremser et al. 2014; Mitchell 2003), was used to statistically model the dependence of:

1. SCO on EESC and CO_2,
2. the vertically weighted SCO (wSCO) on EESC and CO_2, and
3. stratospheric ozone RF on wSCO

SCO is modelled since this is of direct interest to policy-makers (in terms of dates of return of ozone to unperturbed levels). EESC is a measure of the net effect of chlorine and bromine on ozone and is therefore included as a predictor in the ozone regression models (see Sec. 6.3.1, *v.i.*). CO_2 is also included as a predictor since it affects stratospheric temperatures which in turn impact ozone chemistry.
RF depends on the altitude, i.e. the point in the radiating layer, at which the change in ozone occurs (Forster and Shine 1997; Lacis et al. 1990). To capture this, the ozone profile that is used to calculate SCO is weighted so that the ozone near the tropopause has a greater influence on the RF compared to ozone at higher altitudes. The simulated wSCO is used in a second regression model (see Sec. 6.3.2, *v.i.*).
Ozone RF is simulated in MAGICC so that modelled changes in ozone modulate the total RF thereby coupling stratospheric ozone changes to the climate system. A third regression model was trained on the vertically weighted ozone and its corresponding RF (see Sec. 6.3.3, *v.i.*).

6.3.1 *Statistical modelling of SCO*

The regression model used to capture the functional dependence of zonal mean SCO anomalies on global EESC and CO_2 anomalies is of the form:

$$SCO'_i = \alpha_i EESC' + \beta_i CO'_2 + \epsilon \tag{6.1}$$

The primes in Eq. 6.1 denote anomalies with respect to 1960 levels and the coefficients α, β and ϵ are obtained from fitting Eq. 6.1 to CCM output for each latitude zone i. Daily zonal mean SCO' and EESC', simulated by the ECHAM/MESSy Atmospheric Chemistry (EMAC) (Jöckel, 2006) CCM, and CO_2 anomalies following the RCP8.5 emissions scenario, were used to derive the fit coefficients. Fit coefficients are derived across the 64 latitude zones represented in EMAC.
To capture the seasonal dependence of SCO' on EESC' and CO_2', the fit coefficients in Eq. 6.1 are expanded in a Fourier series:

$$\alpha(t) = \alpha_0 + \sum_{k=1}^{M} [\alpha_{2k-1} \sin(\frac{2\pi kt}{365}) + \alpha_{2k} \cos(\frac{2\pi kt}{365})] \qquad (6.2)$$

where t is the day of the year and M is the number of Fourier pairs to which the fit coefficient are expanded. The value of M can be set depending on the seasonal structure expected in the fit coefficients. For the analysis presented here, M in Eq. 6.2 was set to 4 for ϵ in Eq. 6.1, and 2 for α and β.

In our model, the effects of GHGs on the abundances of polar stratospheric clouds (PSCs), by virtue of their cooling effect on the stratosphere, are not directly accounted for. Because PSCs are essential for the polar heterogeneous chemistry that causes severe ozone depletion (Huck et al. 2013), increases in GHG concentrations increase the ubiquity of PSCs and reduce ozone. Our methodology considers only the positive effects of GHG-induced stratospheric cooling on ozone Chapman chemistry. That said, the effects of PSCs on polar ozone are captured in our regression model of SCO in the form of elevated sensitivity of polar ozone to EESC in the polar regions. The use of a semi-empirical model such as SWIFT (Semi-empirical Weighted Iterative Fit Technique) (Rex et al., 2013) in MAGICC for the polar regions could improve the simulation of the direct effects of GHGs on ozone Chapman chemistry and the indirect effects of GHGs on heterogeneous ozone chemistry via PSCs.

6.3.2 *Statistical modelling of wSCO*

To account for the vertical dependence of RF on ozone in MAGICC, wSCO was trained similarly to Eq. 6.1 but with wSCO′ replacing SCO′. The weights (w) needed to calculate wSCO were obtained from the RF sensitivity function developed by Lacis et al. (1990),

$$\begin{aligned} w_{i,j} &= 0.334e^{-z_{i,j}/3.6} \\ &\quad - 5.4 \times 10^{-5}(z_{i,j} - z_{th})^{1.4}(1 - 41e^{-z_{th}/7.5}) \end{aligned} \tag{6.3}$$

where z is the altitude in km at latitude i and level j and z_{th} is the tropopause height. The location of the tropopause, which is also used to calculate the SCO, was determined using the WMO definition i.e. the altitude at which the lapse rate falls below -2 Kkm^{-1} and stays below -2 Kkm^{-1} for at least 2 km.

6.3.3 *Statistical modelling of RF*

A similar technique was used to determine the functional dependence of RF on wSCO. Because the radiative effect of stratospheric ozone varies with latitude, zonal mean wSCO′ for the combined polar regions (60°-90° N/S), the combined midlatitudes (30°-60° N/S) and the equatorial region (30°S-30°N) were used as predictors for global stratospheric ozone RF as:

$$RF = \sigma wSCO'_{90°-60°} + \phi wSCO'_{60°-30°} + \omega wSCO'_{30°-0°} + \epsilon \tag{6.4}$$

where the coefficients σ, ϕ, ω and ϵ are derived by fitting Eq. 6.4 to wSCO′ calculated from the ozone database that was constructed in support of Coupled Model Intercomparison Project Phase 5 (CMIP5) simulations and corresponding stratospheric ozone RF (Cionni et al., 2011).
There are few archived CCM model simulations which provide latitudinally resolved ozone at monthly resolution and corresponding RF values that can be used for training a wSCO′ to RF regression model. There are also uncertainties in the RF used in

the training, primarily due to outdated ozone absorption coefficients (Cionni et al., 2011). These uncertainties propagate into the regression and therefore also the simulation of RF within MAGICC. Availability of a larger number of ozone and RF data sets from CCM simulations would make the training of the wSCO′ to RF regression model more robust.
To test whether the uncertainty in our regression-derived relationship between wSCO′ and ozone RF may affect our derived years of return of SCO to 1960 levels, a set of regression model coefficients, obtained by averaging the coefficients obtained for equatorial, mid-latitude and polar regions, was used to drive the wSCO′ to ozone RF. The years of return were shown to be largely insensitive to the wSCO′ to RF relationship encapsulated in the regression model.

6.3.4 *An interactive stratosphere in MAGICC*

The coefficients derived from equations 6.1, 6.2 and 6.4 are used in MAGGIC to calculate stratospheric ozone RF from SCO′ and wSCO′. The wSCO′ values are averaged over the three latitude zones 60°-90° N/S, 30°-60° N/S and 30° S-30°N and the resulting ozone RF is then calculated using Eq. 6.4. The ozone RF for the three latitude zones is summed to create an annual global stratospheric ozone RF. This global RF is partitioned into four regions, viz. northern hemisphere ocean and land and southern hemisphere ocean and land as required by the underlying MAGICC model, thereby coupling the MAGICC stratosphere to the climate system.

6.4 RESULTS: YEARS OF RETURN OF STRATOSPHERIC COLUMN OZONE TO 1960 LEVELS

Tunings to 18 different AOGCMs and 10 different carbon cycle models used in the World Climate Research Programme's Coupled Model Intercomparison Project phase 3 (CMIP3) multi-model dataset (Meehl et al., 2007b) and Coupled Carbon Cycle Climate

Model Intercomparison Project (Friedlingstein et al., 2006), are used to explore the effects of model structural uncertainty on the SCO projections and return dates. The tuning procedure is outside the scope of this thesis, but is very briefly described in Sec. 3.2.3. MAGICC is then run with an interactive stratosphere, for all 180 combinations of AOGCMs and carbon cycle model tunings, creating one ensemble for each of the four Representative Concentration Pathways (RCP) emissions scenarios, viz. RCP2.6, RCP4.5, RCP6 and RCP8.5 (Moss et al., 2010), from 1960 to 2100. All simulations were run under the A1 ODS scenario (Daniel et al., 2007).
The probabilities of the return dates of zonal mean SCO to 1960 levels for all RCP emissions scenarios are shown in Fig. 6.1. The return to 1960 values is projected to occur earliest at mid-latitudes, later in the polar regions and latest, if at all, in the tropics (Fig. 6.1 and Table 6.1). The results presented here are consistent with previous studies (Eyring et al. 2013; Garny et al. 2013; Bekki et al. 2013; Cionni et al. 2011; Eyring et al. 2010a) but now include robustly determined uncertainties in the dates of return.

At 60°N, under the RCP2.6 emissions scenario, SCO is expected to return to 1960 levels between 2020 and 2028, with an average year of return in 2022.4±1.9 (ensemble mean $\pm 1\sigma$, as stated ranges hereafter) (Table 6.1) and with the most likely year of return (the mode of the ensemble) in 2023 (Fig. 6.1). At 60° S, the mean year of return of SCO to 1960 levels is 2067.9±8.2, around 45 years later, and with a larger uncertainty, compared to the return date at 60°N. Chemically-induced changes in ozone (Garny et al., 2013), as well as changes in ozone due to changes in the strength of the BDC (Butchart 2014; Eyring et al. 2010b) drive an earlier return of SCO to unperturbed levels in the Northern Hemisphere than in the Southern Hemisphere. An enhanced tropical upwelling, as a part of the BDC, is an important driver of reductions of ozone in the tropical lower stratosphere (Pawson, Steinbrecht et al., 2014).

The largest spread in simulated years of return of SCO to 1960 levels is found at 40°N, 40° S and in the Antarctic. At 40°N, un-

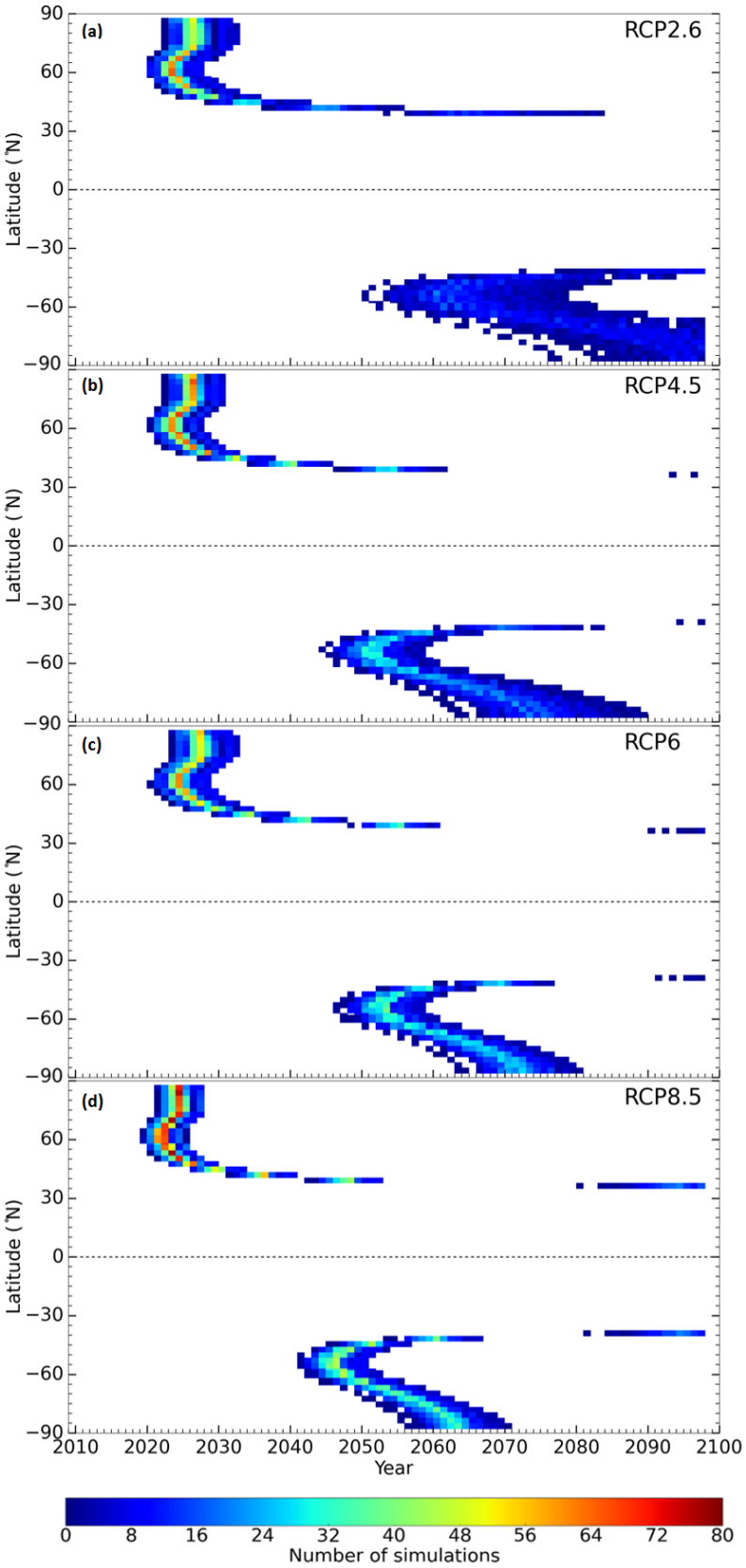

Figure 6.1: Probability of year of return of SCO to 1960 levels. 180 member ensembles for 90° S to 90°N, simulated with MAGICC under four GHG emissions scenarios: RCP2.6 **(a)**, RCP4.5 **(b)**, RCP6.0 **(c)** and RCP8.5 **(d)**.

Table 6.1: The mean years of return of SCO to 1960 levels.

	RCP2.6	RCP4.5	RCP6.0	RCP8.5
85°N	2025.2±2.1	2024.9±2.0	2026.1±1.9	2023.0±1.3
	[2022-2032]	[2022-2030]	[2023-2031]	[2021-2027]
60°N	2022.4±1.9	2022.5±1.6	2023.4±1.9	2022.4±1.3
	[2020-2028]	[2019-2027]	[2020-2028]	[2019-2025]
40°N	2066.1±8.4	2052.3±3.4	2.53.3±2.5	2046.4±2.2
	[2053-2083]	[2046-2062]	[2048-2061]	[2042-2053]
40° S	[2072-]	2069.7±4.8	2067.6±3.0	2058.9±2.5
		[2060-2084]	[2060-2077]	[2053-2067]
60° S	2067.9±8.2	2053.2±3.2	2054.2±2.4	2047.2±2.0
	[2052-2082]	[2046-2060]	[2047-2060]	[2042-2052]
85° S	[2076-]	2074.3±6.0	2071.3±3.1	2061.8±2.5
		[2063-2089]	[2063-2080]	[2056-2070]

der RCP2.6, SCO is expected to return to 1960 levels in 2066.1 ± 8.4, with the 180 member ensemble ranging from 2053 to 2083 (Table 6.1). At 40° S, SCO is projected to return to unperturbed levels at the earliest in 2072, and some of the simulations suggest a return beyond 2100. With increasing GHG loading of the stratosphere, the ensemble spread in dates of return of extra-tropical latitude SCO to 1960 levels decrease. At 40°N the ensemble spread decreases from ±8.4 years when simulated under RCP2.6 to ±2.2 years under RCP8.5 (Table 6.1). Under RCP8.5, all simulations show a return of SCO to 1960 levels before the end of this century at 40° S, and the mean year of return is 2058.9 ± 2.5. At 40°N, under RCP8.5, SCO returns to 1960 levels 20 years earlier than under RCP2.6. The min-max spread in simulated return years in the Arctic is 10 years under RCP2.6 and 6 years under RCP8.5. In the Antarctic, the range of return dates is more than 25 years (with values beyond 2100) under RCP2.6, and decreases to 14 years (with a $\pm 1\sigma$ of 2.5 years) under RCP8.5. Under RCP8.5, the return year in the Arctic shifts earlier compared to RCP2.6, from 2025.2 to 2023.0. Until 2060, CO_2 emissions under RCP4.5 are larger than under RCP6.0 which results in SCO at some latitudes returning slightly earlier to 1960 levels for RCP4.5 compared to RCP6.0 (Fig. 6.1 and Table 6.1).

6.4.1 *Ensemble simulations of SCO anomalies*

The differences in ensemble spreads of return years of SCO between different emissions scenarios can be understood by considering the evolution of SCO throughout the 21st century. SCO' simulated under the RCP8.5 emissions scenario shows larger changes (decreases in tropics (30° S to 30° N), and increases in the mid-latitudes (30° to 60°) and the polar regions (60° to 90°)) than under RCP2.6 and therefore crosses the zero anomaly line earlier and within a smaller range of years than under RCP2.6 (Fig. 6.2). The simulations of SCO' are averaged over the Southern and Northern hemisphere 30° zones, since the RF from stratospheric ozone (right-hand axis in Fig. 6.2, discussed

Table 6.2: Zonal mean SCO'and the approximate corresponding mean RF projected for the end of the century (2100). The SCO anomalies are with respect to 1960. The uncertainties are expressed as $\pm 1\sigma$, and the range of SCO'and RF (minimum-maximum) are shown in brackets.

	SCO'(DU)		RF (mWm^{-2})	
	RCP2.6	RCP8.5	RCP2.6	RCP8.5
30° S - 30° N	-4.9±0.9	-24.6±3.4	-20.4±4.0	-120.3±19.7
	[-7.1 to -3.7]	[-40.4 to -18.3]	[-30.8 to -14.9]	[-232.6 to 80.1]
30° - 60° S/N	1.3±0.6	12.5±1.9	3.2±1.6	38.4±7.3
	[0.5-3.1]	[8.6-21.6]	[0.9-7.9]	[23.5-70.4]
60° - 90° S/N	3.9±1.5	31.8±4.9	0.6±0.2	5.1±1.0
	[1.7-8.1]	[22.3-54.6]	[0.3-1.3]	[3.6-9.0]

below) in MAGICC is simulated over Southern and Northern hemispheres zones combined.

Although tropical SCO is not projected to reach 1960 levels before the end of this century, the simulations under RCP2.6 indicate a slow increase from around 2030 onwards, consistent with previous studies (Eyring et al. 2013, 2010b,a). At the end of the century, the SCO ensemble mean under RCP2.6 is 4.9 DU below 1960 levels, with an uncertainty of ±0.9 DU (Table 6.2). Under the highest emissions scenario, SCO is likely to continue to decrease in the tropics due to a strengthening of the BDC, with the spread in simulations increasing to ±3.4 DU. Under RCP8.5, while SCO decreases in the equatorial regions, it continues to increase in the middle and high latitudes, surpassing 1960 levels (Fig. 6.2). At the end of the century, extra-tropical SCO is projected to reach levels well above those of 1960, especially under the RCP8.5 emissions scenario.
In the mid-latitudes, under RCP2.6, the ensemble mean in 2100 is 1.3 DU above 1960 levels with an uncertainty of ±0.6 DU

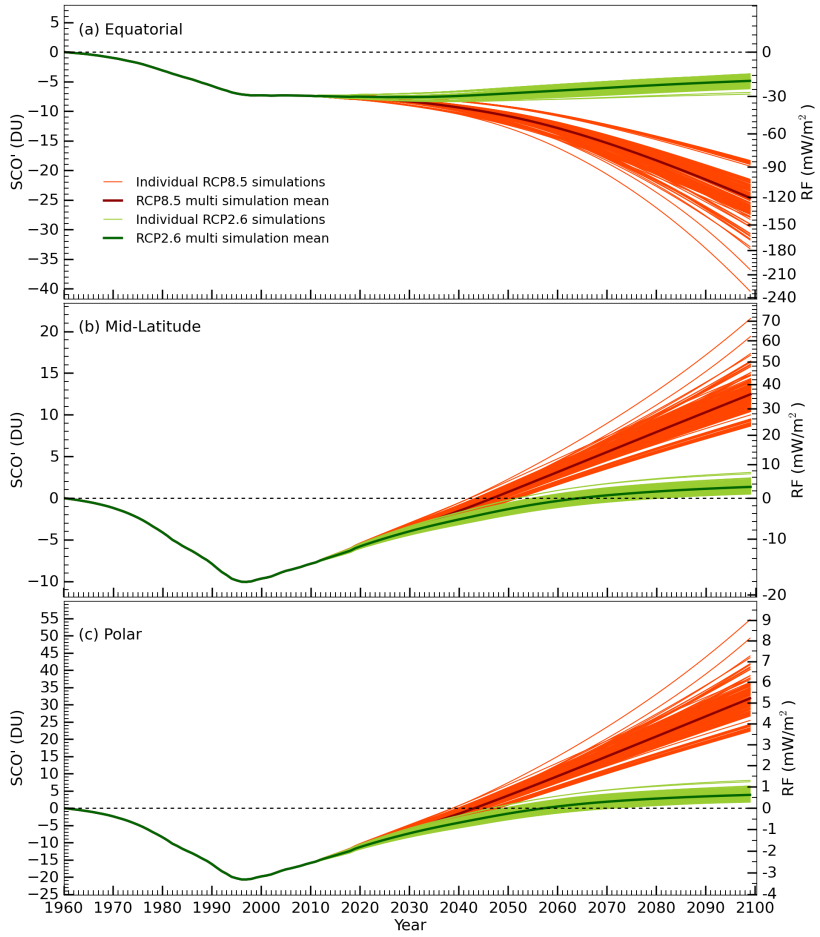

Figure 6.2: Ensembles of 180 simulations of zonal mean SCO corresponding approximate RF. The SCO anomalies are with respect to 1960 on the left hand axis while the corresponding approximate RF is shown on the right-hand axis, for three latitude zones, under RCP2.6 and RCP8.5, for three latitude zones: Equatorial (30° S-30° N) **(a)**, mid-latitude (30°-60° S/N) **(b)** and polar (60°-90° S/N) **(c)**.

while under RCP8.5 the ensemble mean is more than nine times larger (12.5 DU) with an uncertainty of ±1.9 DU. In the polar regions, the ensemble mean in 2100 under RCP8.5 is eight times larger than the ensemble mean simulated under RCP2.6 and the uncertainty is more than three times larger (3.9 ± 1.5 DU cf. 31.8 ± 4.9 DU). At the end of the century the uncertainty in SCO′ simulated under RCP8.5 is more than twice as large in the polar regions than in the mid-latitudes.

6.4.2 *Ensemble simulations of stratospheric ozone radiative forcing*

By the end of the century, the ensemble mean ozone RF in the equatorial region simulated by MAGICC under RCP2.6 is -20.4 ± 4.0 mWm^{-2} and under RCP8.5 -120.3 ± 19.7 mWm^{-2} (right-hand axis of Fig. 6.2 and Table 6.2). Noting the non-linear scale on the right-hand axes in Fig. 6.2, the spread in RF simulations, as for SCO, increases with increasing GHG loading. A negative RF contributes to a lowering of the surface temperature.

In the extra-tropics, the negative RF from stratospheric ozone maximizes in the mid-1990s due to substantial depletion of ozone by ODSs at that time (Fig. 6.2). Thereafter, the negative RF from ozone decreases and is simulated to become positive in the middle of the 21st century. In contrast to SCO, in the polar regions the ensemble mean RF, as well as the simulation spread, are smaller than in the mid-latitudes, under both RCP2.6 and RCP8.5, due to the dependence on RF of the vertical distribution of ozone. By 2100, under RCP8.5, the 180 member ensemble mean RF in the mid-latitudes is 38.4 ± 7.3 mWm^{-2}, more than 7 times larger than in the polar regions where the mean RF is 5.1 ± 1.0 mWm^{-2}. A stronger BDC enhances transport of ozone in the lower stratosphere from the tropics to the mid- high latitudes (Pawson, Steinbrecht et al., 2014). Since RF is affected mainly by ozone in the lower stratosphere, the largest change in RF is expected to be found where the largest change in lower stratospheric ozone takes place (Lacis et al., 1990). Under RCP2.6, the ensemble mean RF is smaller

Table 6.3: Zonal mean SCO′ projected for the end of the century (2100) for simulations where either CO_2 or EESC is kept constant. The uncertainties are expressed as $\pm 1\sigma$ and the SCO′ ranges (min-max) are shown in brackets.

	SCO′(DU),const. CO_2		SCO′(DU),const. EESC	
	RCP2.6	RCP8.5	RCP2.6	RCP8.5
Equatorial	-0.5±0.1	-0.24±0.1	-4.4±0.9	-24.4±3.4
	[-0.6 to -0.3]	[-0.4 to 0.0]	[-6.9 to -3.1]	[-40.6 to -17.9.1]
Midlatitudes	-1.0±0.6	-0.5±0.2	2.3±0.5	13.0±1.9
	[-1.2 to -0.5]	[-0.9 to -0.9]	[1.7 to 3.7]	[9.5 to 21.6]
Polar	-2.1±0.3	-1.0±0.4	5.9±1.2	32.9±4.7
	[-2.5 to -1.1]	[-1.8 to 0.2]	[4.2 to 9.3]	[24.2 to 54.7]

than under RCP8.5 with a narrower uncertainty range; 3.2 ± 1.6 mWm^{-2} in the mid-latitudes and 0.6 ± 0.2 W/m^{-2} in the polar regions.

6.5 DISCUSSION AND SUMMARY

The output from our 180 member ensemble simulation study shows that increasing GHG loading decreases the ensemble spread in projections of years of return of SCO to 1960 levels, but increases the ensemble spread in SCO and corresponding RF simulations, due to increased spread in CO_2 (Fig. 6.3). SCO′ as well as the spread in SCO′, increase with increasing GHG loading and decreasing EESC′. The influence of GHGs on SCO′ increases around the middle of this century, while the ozone depleting effect of EESC becomes less important. To confirm the dominant effect from CO_2, MAGICC was run first with constant CO_2 and thereafter with constant EESC′. In the polar regions, for RCP8.5 simulations, the uncertainty in SCO′ at the

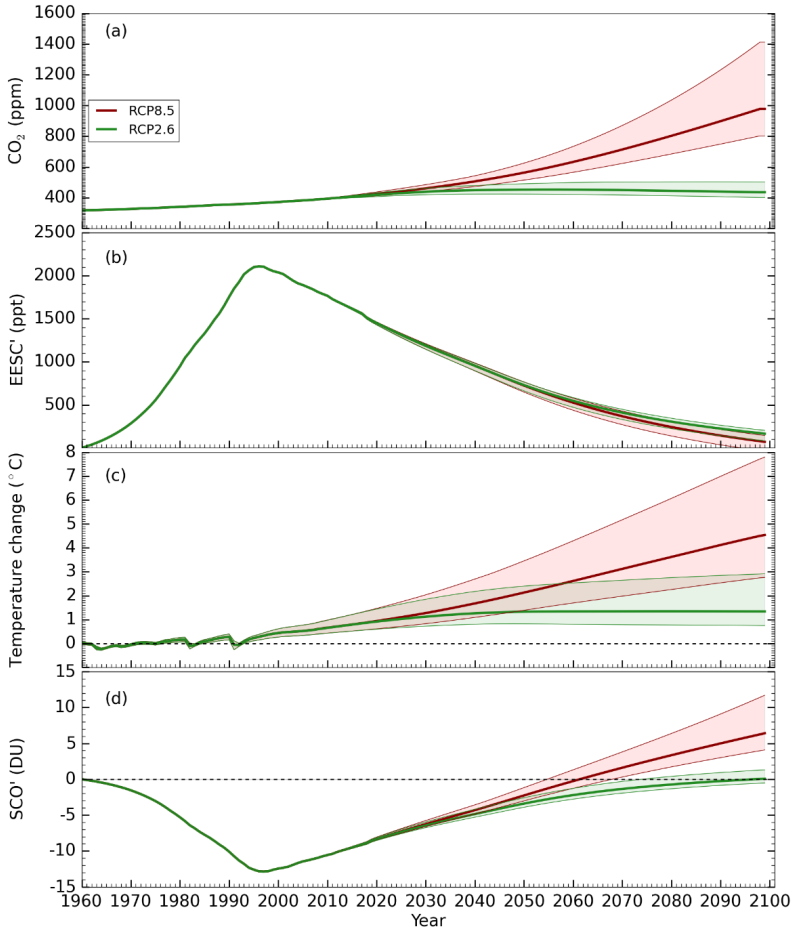

Figure 6.3: Global 180 member ensemble mean time series (solid lines) with uncertainty ranges (shaded areas) for CO_2 concentrations **(a)**, EESC anomalies with respect to 1960 **(b)**, surface temperature changes with respect to 1960 **(c)** and SCO anomalies with respect to 1960 **(d)**. All results are shown for two different GHG emissions scenarios.

end of the century decreases from ±4.9 DU (Table 6.3) to ±0.4 DU when CO_2 is kept constant, compared to a decrease to ±4.7 DU when EESC is kept constant (Table 6.3). The same pattern is found in the equatorial region and the mid-latitudes.
SCO is simulated to never reach 1960 levels when CO_2 is kept fixed and with changing EESC concentrations. Under RCP2.6, the differences between uncertainties in simulations when CO_2 is kept fixed and EESC is kept fixed are smaller compared to RCP8.5 simulations, since the total GHG loading is smaller, and therefore the effect from EESC is greater (Table 6.3).
There is a clear relationship between the change in tropical upwelling, as part of the BDC, and the response of tropical ozone in the lower stratosphere, and CCMs show a wide range of responses of the BDC to a single emissions scenario. The effect of the BDC on EESC' in MAGICC is represented in terms of stratospheric lifetimes of halogenated gases, and the uncertainties in EESC' ensemble simulations are largest at the end of the century, when the spread in simulated CO_2 concentrations and surface temperature are large (Fig. 6.3). The BDC effect on the relationship between CO_2 (as a proxy for the stratospheric temperature), EESC' and SCO' is embedded in the simulations through the fitting of Eq. 6.1 to the EMAC model. To capture the full range of responses of the BDC to climate change across different CCMs, the method presented here could be used in the future to emulate a range of CCMs. For the present study, CO_2 is a proxy for temperature and climate related effects in the settings of Eq. 6.1. In future work and further development of the SCM, other gases that affect stratospheric ozone concentrations such as methane and nitrogen oxide, could be added to the regression (Eq. 6.1). Thereby contributions to uncertainties from compounds other than CO_2 and EESC could be estimated.
Since the output from our ensemble simulations are based on MAGICC emulations of different AOGCMs and carbon cycle models, the spreads in simulations may be different compared to what would be generated by an ensemble of 180 CCM simulations. Selected sets of key parameters are used to force MAGICC to emulate the behavior of any one of 18 different AOGCMS and any one of 10 difference carbon cycle models; para-

meter sets optimize the ability of MAGICC to simulate global-mean temperatures and ocean heat uptake (Meinshausen et al. 2011b,a). The different sets of parameters, captured in MAGICC, determine the spread in our ensemble of SCO projections using MAGICC. It is not possible to include the full range of parameter possibilities (i.e. as included in each one of the AOGCMs and carbon cycle models) in the tuning of MAGICC. This limits our ability to capture the full range of uncertainty (Meinshausen et al. 2011b,a). Furthermore, in MAGICC common forcing agents, for example forcing from CO_2, tropospheric ozone, direct black carbon, etc., are averaged over all emulated AOGCMs and therefore model spread due to differences in there forcing agents is not accounted for, which further narrows the spread of simulations (Meinshausen et al. 2011b,a), and therefore also in our MAGICC simulations.
Previous multi-model studies of years of return of stratospheric ozone to unperturbed levels include simulations either from groups of CCMs that are run under a single GHG emissions scenario (Eyring et al. 2007, 2010a), or from only a few CCM simulations run under a set of emissions scenarios (Eyring et al. 2010b, 2013). Agreement of the mean behavior of our ensemble of simulations with the results of these earlier studies provides confidence in the overall behavior of our simulations. Since our study is the first to provide a full probability density function (PDF) of projections of SCO, it is not possible to validate our PDFs against these earlier studies.

6.6 ADDENDUM

6.6.1 *Preparation of data - Tropopause height*

In this work stratospheric ozone and RF output from the CCM EMAC and the CMIP5 data set was used, as described in Sec. 6.3. Ozone output from EMAC and the CMIP5 dataset required some preparation since in this work the zonal mean stratospheric column ozone was of interest, rather than the vertially

and longitudinally resolved data provided by the EMAC and CMIP5 dataset output files. To be able to separate the stratospheric ozone from the tropospheric ozone, it was necessary to find the tropopause height. The tropopause is the boundary between the turbulent mixed troposphere and the stably stratisfied stratosphere. The tropopause is often described as a transition region between the troposphere and the stratosphere (Birner et al., 2006). In order to calculate stratospheric ozone budgets, knowledge of an exact tropopuase height is required. It has been shown that variations of 1-2 km in the location of the tropopause can cause differences of 10-20% in the total tropospheric column ozone (Stajner, 2008).

The tropopause height depends on the temperature in the troposphere and on the amount of ozone above the tropopause. The increase in tropopause heigths is affected by expansion, because of warming, of the troposphere and also through cooling of the stratosphere, see for example the work of Hall et al. (2011). Hall et al. presented results from a seasonal climatology of tropopause altitude for 78°N 16°E, derived from observations between 2007-2010 on Svalbard. They found that the spring minimum in tropopause height occurs one month later than the spring minimum of the surface air temperature but coincides with the maximum in ozone column density. Due to the effects of changes in temperature and stratospheric ozone abundances it has been discussed if tropopause height might be useful as an indicator of climate change (Sausen and Santer 2003; Santer et al. 2003).

Ozone in the lower stratosphere, in particular ozone close to the tropopause, has a greater effect on RF than ozone in the upper stratosphere. This is due to the lower temperature in the lower stratosphere (Forster and Shine, 1997). Therefore, as mentioned in Sec. 6.3.2, when calculating the ozone to be used in the calculation of RF, it is necessary to weight the ozone profile. The effect of ozone on RF decreases approximately exponentially with altitude which makes it extremely important to calculate tropopause heights correctly in the calculation of RF from stra-

tospheric ozone.

The tropopause heights used in the calculations of SCO from ozone profiles from the CMIP5 dataset are the climatological tropopause heights from the CMIP5 project. However, the tropopause heights used for the EMAC data were calculated from temperature and pressure profiles, due to inconsistencies in time resolution and vertical structure in the EMAC simulations.

6.6.1.1 *Calculation of tropopause heights from EMAC data*

The tropopause altitude was determined from the definition of the World Meteorological Organization (1992):

The boundary between the troposphere and the stratosphere, where an abrupt change in lapse rate usually occurs. It is defined as the lowest level at which the lapse rate decreases to 2°Ckm^{-1} or less, provided that the average lapse rate between this level and all higher levels within 2 km does not exceed 2°Ckm^{-1}.

In this work we use the atmospheric levels in altitude rather than pressure, therefore also the tropopause height was calculated in km. First the pressure levels given in the EMAC output files (38 levels) where converted from pressure to altitude, for each time step t (daily data was used), using the hydrostatic approximation as follows,

$$z_{i,j,l}(t) = \frac{RT_{i,j,l}(t)}{g} \times \log(\frac{p_{i,j,l}(t)}{p_0}) \times 1000 \tag{6.5}$$

where the subscripts i, j and l represent the longitude, latitude and atmospheric level, respectively, $z_{i,j,l}(t)$ is the altitude in km, R is the gas constant for dry air (287.058 Jkg^{-1}K^{-1}), $T_{i,j,l}(t)$ is the EMAC daily mean temperature in K, g is the gravity constant (9.81 ms^{-2}), $p_{i,j,l}(t)$ is the EMAC zonal mean pressure at the current atmospheric level and p_0 is the mean pressure at sea level. In a first attempt of calculating the tropopause height, $RT_{i,j,l}(t)/g$ in Eq. 6.5, i.e. the scale height, was approximated

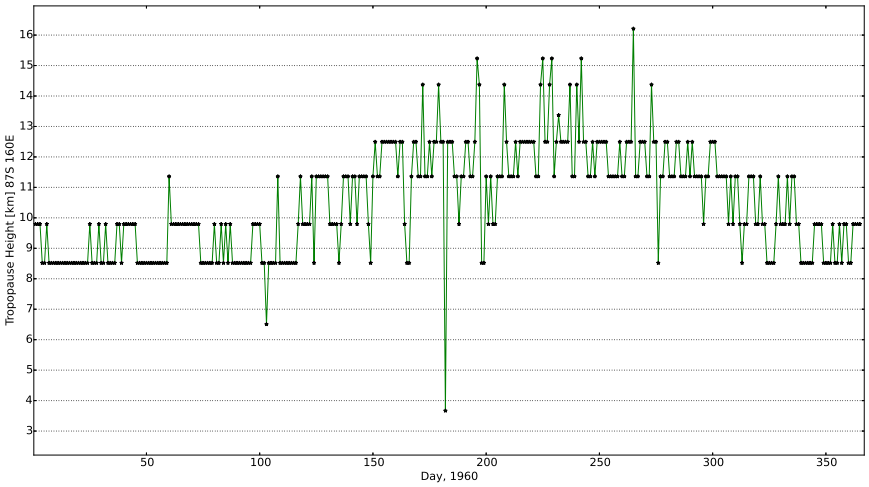

Figure 6.4: Timeseries of calulated daily tropopause heights 87°S, 160°E, 1960.

by 7 km. Furthermore, zonal mean pressure levels were used, rather than using data with longitudinal resolution, and therefore $z_{i,j,l} = z_{j,l}$ is not dependent on longitude. The calculated $z_{j,l}$ and EMAC zonal mean temperature profiles, $T_{j,l}(t)$, (64 latitudes and 38 levels) were used to calculate the zonal mean lapse rates at half levels as follows,

$$\Gamma_{j,l+1/2}(t) = -\frac{T_{j,l+1}(t) - T_{j,l}(t)}{z_{j,l+1}(t) - z_{j,l}(t)} \tag{6.6}$$

The first atmospheric level where the lapse rate decreases to below 2 kmK^{-1} defines the tropopause height. This method is very simple to implement, however the atmospheric levels are quantized, and therefore the tropopause heights are not very accurate. Figure 6.4 demonstrates how the tropopause height "flips"switches between the atmospheric levels.

To improve the estimation of the tropopause height, all longitudes, latitudes and levels given in the EMAC output were used, rather than zonal means. The altitudes $z_{i,j,l}$ in Eq. 6.6 were obtained from converting the EMAC pressure levels to altitudes in km using the hydrostatic formula (Eq. 6.5) and the temperature

profiles from EMAC (rather than approximate $RT_{i,j,l}(t)/g$ with 7 km), for all longitudes, latitudes, vertical levels and with a time step of one day. This means that there is an altitude profile for each longitude, latitude and day from 1960-2100. Furthermore, rather than using the predefined pressure levels from the EMAC output as tropopause heights, the interpolation method described in the work of Reichler et al. (2003) was used. After the lapse rates at half levels were calculated, according to Eq. 6.6, for all longitude, latitudes and days for the years 1960-2100, the half levels were calculated as follows,

$$z_{i,j,l+1/2}(t) = \frac{z_{i,j,l+1}(t) + z_{i,j,l}(t)}{2} \tag{6.7}$$

Thereafter the lowest half level where the lapse rate

1. goes below 2 Kkm^{-1},
2. stays below 2 Kkm^{-1} for at least 2 km

was searched for. When these two criteria were met, the exact tropopause level was calculated with simple interpolation,

$$z_{i,j,th} = z_{i,j,l-1} + (z_{i,j,l} - z_{i,j,l-1}) \times \frac{2.0 - \Gamma_{i,j,l-1}}{\Gamma_{i,j,l} - \Gamma_{i,j,l-1}} \tag{6.8}$$

where the subscript th denotes the tropopause level. In order to find out whether the lapse rate was still below 2 Kkm^{-1} for at least 2 km above the level where it first went below 2 kmK^{-1}, another simple interpolation had to be used, in order to find the exact altitude, rather than the prescribed pressure level provided by the EMAC files. Profiles of the calculated lapse rates for a chosen day, longitude and latitude (15^{th} of January 1960, 160°E, 87°S) are shown in Fig. 6.5. The temperature decreases with altitude in the troposphere, which gives a positive lapse rate. Close to the tropopause, the temperature increase slows down, and at the altitude of 10 km the lapse rate is 2 Kkm^{-1}. Thereafter the temperature increases with altitude and the lapse rate stays below 2 Kkm^{-1}.

In Fig. 6.6, our calculated tropopause heights obtained from

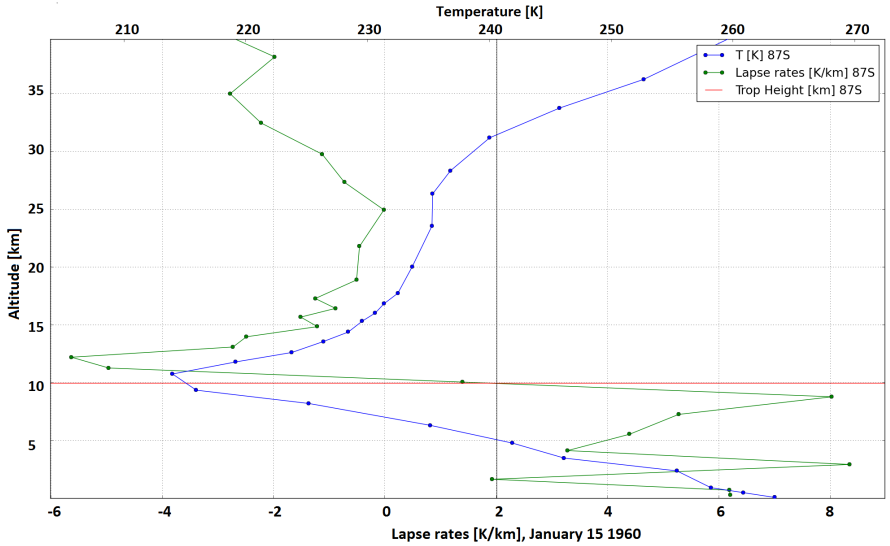

Figure 6.5: Profile of lapse rates (green line) at half vertical model levels calculated from EMAC temperature profiles (blue line), 15^{th} of January 1960, 87°S, 160°E. Red line shows our calculated tropopause height.

the lapse rates calculated with EMAC temperature profiles are compared to the tropopause heights from EMAC output files. Only one single location, at 87°N, 160°E, and one single year, 1960, is shown as an example. The EMAC tropopause heights are given in Pa, and in order to compare them with the tropopause heights calculated from the EMAC temperature profiles they were converted to km using Eq. 6.5. The differences between the EMAC tropopause heights and the calculated tropopause heights occur because the EMAC tropopause height is calculated online with a time-step resolution of 15 minutes, while the tropopause heights calculated from the lapse rates are based on temperature profiles calculated offline, with a time-step resolution of one day, which alters the temperature profiles. Furthermore, the EMAC daily temperature profiles that I used to calculate the lapse rates are interpolated to CCMVal standard pressure levels while the tropopause heights from EMAC output files are based on the model pressure levels.

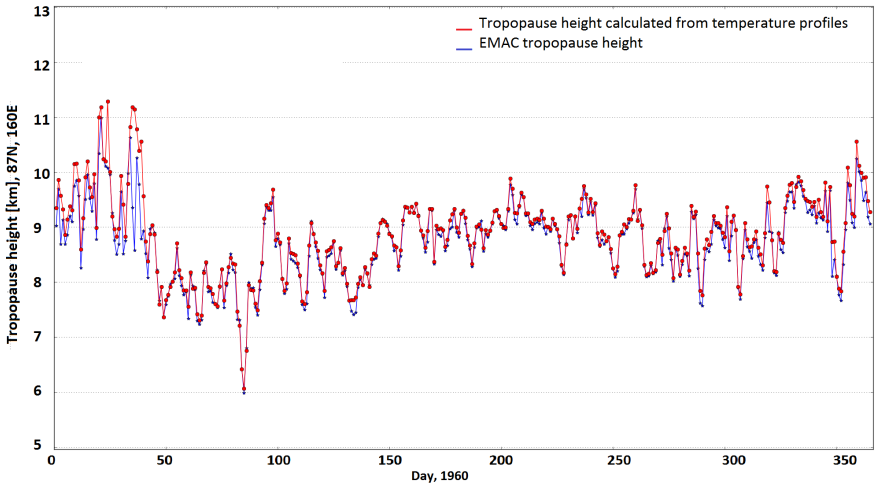

Figure 6.6: Daily tropopause heights timeseries for 87°N, 160°E, 1960. Blue line show the tropopause heights from EMAC output files (converted from Pa to km) and red line show tropopause heights determined from lapse rates calculated from EMAC temperature profiles.

6.6.2 *Preparation of data: EESC*

The global mean EESC used in the training of Eq. 6.1 was calculated from the sum of the two dimensional monthly mean chlorine and bromine compounds, *viz.* Cl_y and Br_y, from EMAC. An equivalency factor is often used to compare the effectiveness of ozone depletion of bromine versus chlorine. In this work we use an equivalency factor α that follows the definition by Daniel et al. (1999),

$$\alpha = \frac{\text{ozone loss rate due to bromine catalytic cycles per bromine atom}}{\text{ozone loss rate due to chlorine catalytic cycles per atom}} \tag{6.9}$$

EESC was calculated according to the work of Newman et al. (2007) and Meinshausen (2001), with a equivalency factor set to 60, i.e.

$$\text{EESC} = Cl_y + 60 \times Br_y \tag{6.10}$$

The monthly mean EESC was interpolated to daily mean, and the anomalies were calculated with respect to 1960 levels, before it was used in Eq. 6.1.

6.6.3 *Preparation of data: SCO*

In MAGICC, we use monthly mean zonal mean SCO. However, the training of the regression model is completed with daily data. First ozone from the EMAC output files was converted from mol/mol to number density, and for that the pressure levels had to be converted from pressure to altitude in meters. Then the SCO could be expressed in Dobson Units (DU). SCO was calculated with tropopause heights calculated as explained in Sec 6.6.1. The stratospheric column ozone for October 1960, 2010 and 2080 are shown in Fig. 6.7. Only one month is shown as an example. The decrease in stratospheric ozone from 1960 to 2010 can clearly be seen, especially over Antarctica. An increase in stratospheric ozone is seen in mid to high latitude ozone in both hemispheres from 2010 to 2080. Furthermore, the start of the breakup of the polar vortex can be seen in the mid-latitudes in the southern hemisphere.

6.6.4 *Preparation of data: wSCO*

WSCO was calculated to account for the vertical dependence of ozone on RF (see Sec. 6.3.2). Daily zonal mean ozone at each level in the stratosphere was multiplied with a daily zonal mean normalized weight, according to

$$s_{j,l}(t) = \frac{w_{j,l}(t)}{\sum w_{j,l}(t)} \tag{6.11}$$

where $w_{j,l}$ is set up as in Eq. 6.3 in Sec. 6.3.2. Lacis et al. (1990) presented a simple method for evaluating the RF of surface temperature from changes in the vertical distribution of ozone and our approach of calculating the weights are based on their method. Lacis et al. (1990) showed that the surface temperature

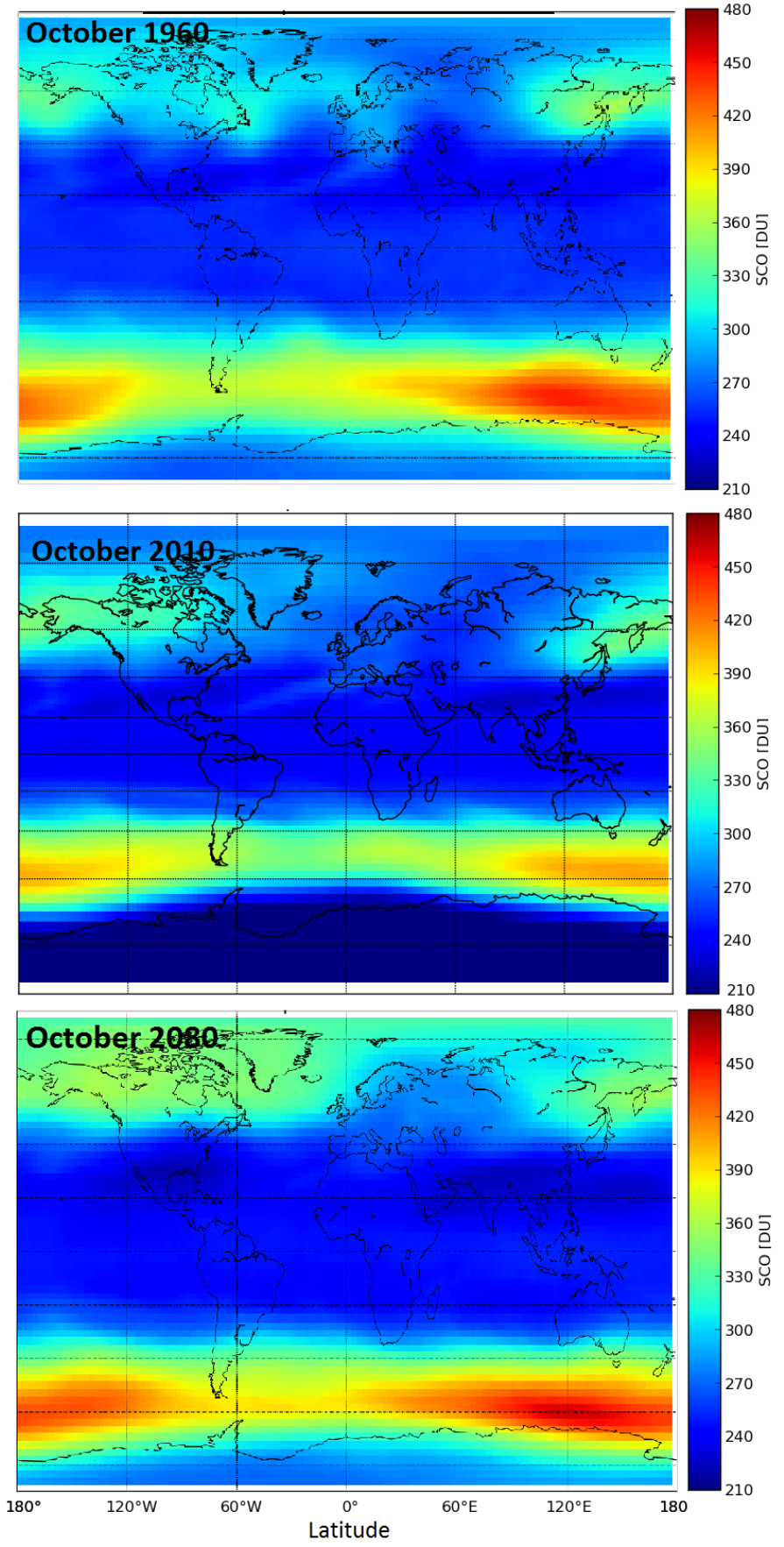

Figure 6.7: Monthly mean stratospheric column ozone from EMAC simulated under the RCP8.5 GHG emissions scenario, for October 1960 (top panel), 2010 (middle panel) and 2080 (bottom panel).

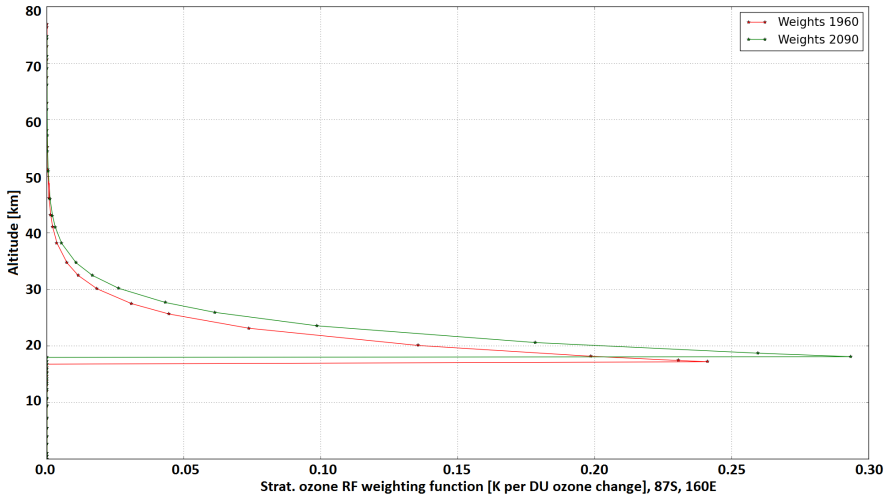

Figure 6.8: Calculated normalized sensitivity functions for 87°S, 160°E, annual mean for 1960 and year 2090.

will warm with increasing ozone below 30 km and cool with increasing ozone above 30 km altitude. In their work they multiply the weighting function with the temperature profile for the specific coordinates of interest. In this study, the temperature profiles above 30 km are omitted and $w_{j,l}$ is set to zero. As an example, the weighting functions for years 1960 and 2090 are shown in Fig. 6.8.

6.6.5 *Preparation of data: RF from stratospheric ozone*

The RF regression model (Eq. 6.4) is trained on the ozone database that was created for the Coupled Model Intercomparison Project Phase 5 (CMIP5), simulated under the RCP8.5 emission scenario, and the corresponding RF values from stratospheric ozone are obtained from Cionni et al. (2011) (as described in Sec. 6.3.3). Figure 6.9 shows the radiative forcing from stratospheric ozone, calculated with the fit coefficients derived from fitting Eq. 6.4 to stratospheric ozone obtained from CMIP5 output. When constructing the CMIP5 database, satellite measurements were used before 2009 and the regression that was used on the stratospheric observations includes terms representing

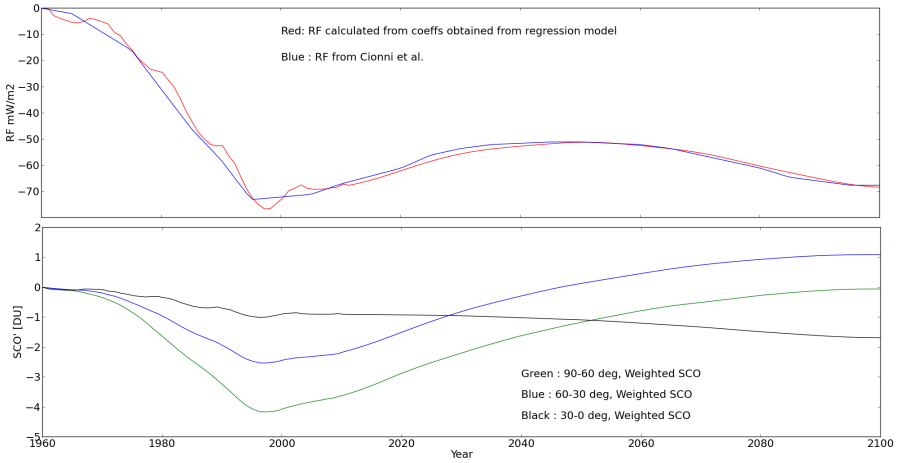

Figure 6.9: Top figure: Annual mean radiative forcing from stratospheric ozone calculated with fit coefficients from the least squares fit technique described in this work (red) and from Ref. Cionni et al. (2011) (blue). Bottom figure shows the basis functions used in the fit, i.e. the annual zonal mean SCO anomalies (w.r.t. 1960 year baseline).

the 11-year solar cycle variability (Cionni et al., 2011). After 2009 a multi-model mean of 13 simulations was used and these simulations do not include solar cycle variations (Cionni et al., 2011). The calculated RF, as well as the SCO anomalies for the three latitude bands used in the regression (0-30, 30-60 and 60-90°S/N) are shown in Fig. 6.9. The variations in the solar cycle before 2009 can be seen in Fig. 6.9, especially in the low latitudes.

6.6.6 *Preparation of data: Statistical modelling of SCO*

The daily mean SCO calculated for the years 1960-2100 with the fit coefficients derived from training the regression model (Eq. 6.1) on EMAC, with EMAC EESC' and CO_2' as basis functions, is shown in Fig. 6.10. SCO calculated with the coefficients agree very well with SCO from EMAC. The ozone minima around year 2000, and the following increase in SCO can clearly be seen. To obtain the SCO anomalies, needed in MAGICC, the

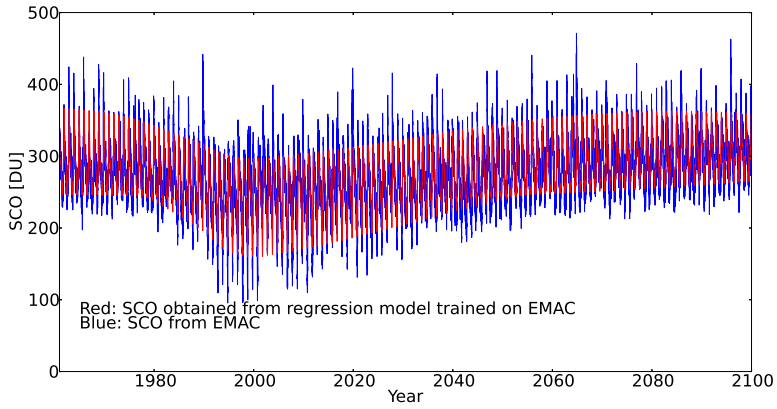

Figure 6.10: Daily zonal mean stratospheric ozone, calculated with coefficients derived from regression model trained on EMAC data simulated under RCP8.5 emissions scenario for 87°S.

coefficient ϵ derived from Eq. 6.1 is set to zero.

To evaluate the derived coefficients the separate contributions from EESC′ and CO_2′ to SCO′ were plotted. In the top panel of Fig. 6.11 only the contribution from EESC′ to SCO′, i.e., the last term in Eq. 6.1, is included, and in the bottom panel only the contribution from CO_2′, i.e. the first term in Eq. 6.1 is included (β is set to zero). The contribution from EESC′ is negative everywhere, as expected, since when EESC decreases in the stratosphere, SCO increases. The depletion of ozone in the southern hemisphere high latitudes around year 2000 can also clearly be seen. It is also evident that SCO increases due to increasing CO_2 burden in the mid to high latitudes in the middle to end of the century, and at the same time the depleting effects from EESC decline. In the low latitudes, decreases in SCO due to increasing CO_2 burden (through strengthening in the BDC circulation, see Sec. 2.3) can also be observed.

6.6.7 *Implementation in MAGICC*

This section describes how the new stratospheric module (presented earlier in this chapter) is incorporated in MAGICC. For an

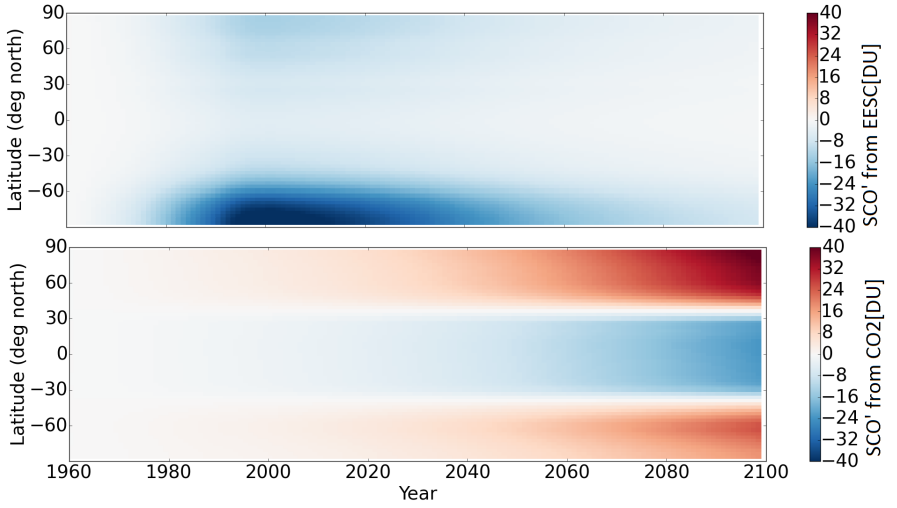

Figure 6.11: Annual mean zonal mean SCO′ calculated with coefficients derived from regression model trained on EMAC data, simulated under the RCP8.5 emissions scenario. Contribution from EESC′, i.e. SCO′ = $\alpha \times$EESC′ (top panel), and from CO_2′, i.e. SCO′ = $\beta \times CO_2$′ (bottom panel)

overview, it might be helpful to look at the flowchart in Fig. 6.12. MAGICC loads three sets of fit coefficients:

- 19 SCO coefficients for 64 latitude zones, derived from EMAC data as descibed in Sec. 6.3.1 and trained on regression model set up in Eq. 6.1.
- 19 wSCO coefficients for 64 latitude zones, derived from EMAC data descibed in Sec. 6.3.2 and trained on regression model set up in Eq. 6.1.
- 3 RF coefficients for 3 latitude zones, trained on ozone from the database created for CMIP5 and corresponding RF from the work of Cionni et al. (2011), using regression model set up in Eq. 6.4.

In MAGICC the SCO anomalies are of interest, therefore the offset coefficients in equations 6.1 and 6.4 are set to zero. The loaded SCO coefficients are used to calculate SCO′ for 64 latitude zones within MAGICC with EESC′ and CO_2′ provided by MAGICC. The resulting SCO′ is an output from MAGICC

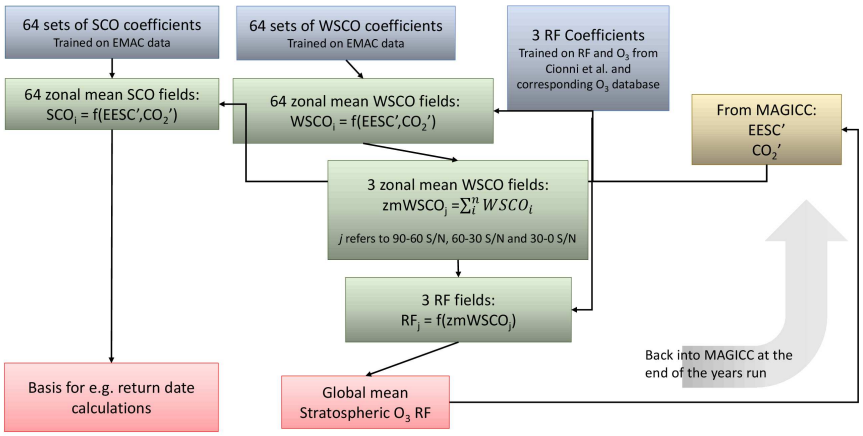

Figure 6.12: Visualizing overview over the new stratospheric module in MAGICC.

and can be used for studies of the evolution of the stratospheric ozone, e.g. probabilistic study of return date calculations.

In a similar way the wSCO coefficients are used to calculate the wSCO' for 64 latitude zones within MAGICC, with EESC' and CO_2' provided by MAGICC. The wSCO' is averaged over three latitude zones, $90° - 60°$, $60° - 30°$ and 30-0° and used with the RF coefficients to calculate global mean RF within MAGICC. The RF is split into four "boxes" to connect with the setup of the MAGICC model: northern hemisphere land, northern hemisphere ocean, southern hemisphere land and southern hemisphere ocean (see also Sec. 3.2.1). Thereafter the calculated RF is fed back into MAGICC, added to the total RF in MAGICC (i.e. RF from climate variables other than SCO) and used in the next year's run.

Figure 6.13 shows an example of SCO' output from a simulation with MAGICC, using the new stratospheric module under the lowest and the highest of the four emissions scenarios used in this study, RCP2.6 and RCP8.5, respectively. Here MAGICC is tuned to the MRI_CGCM2 AOGCM and the BERN carbon cycle model.

In Fig. 6.14 the total RF simulated with MAGICC, with the old stratospheric module (see Eq. 3.10 in Sec. 6.3.4) and the

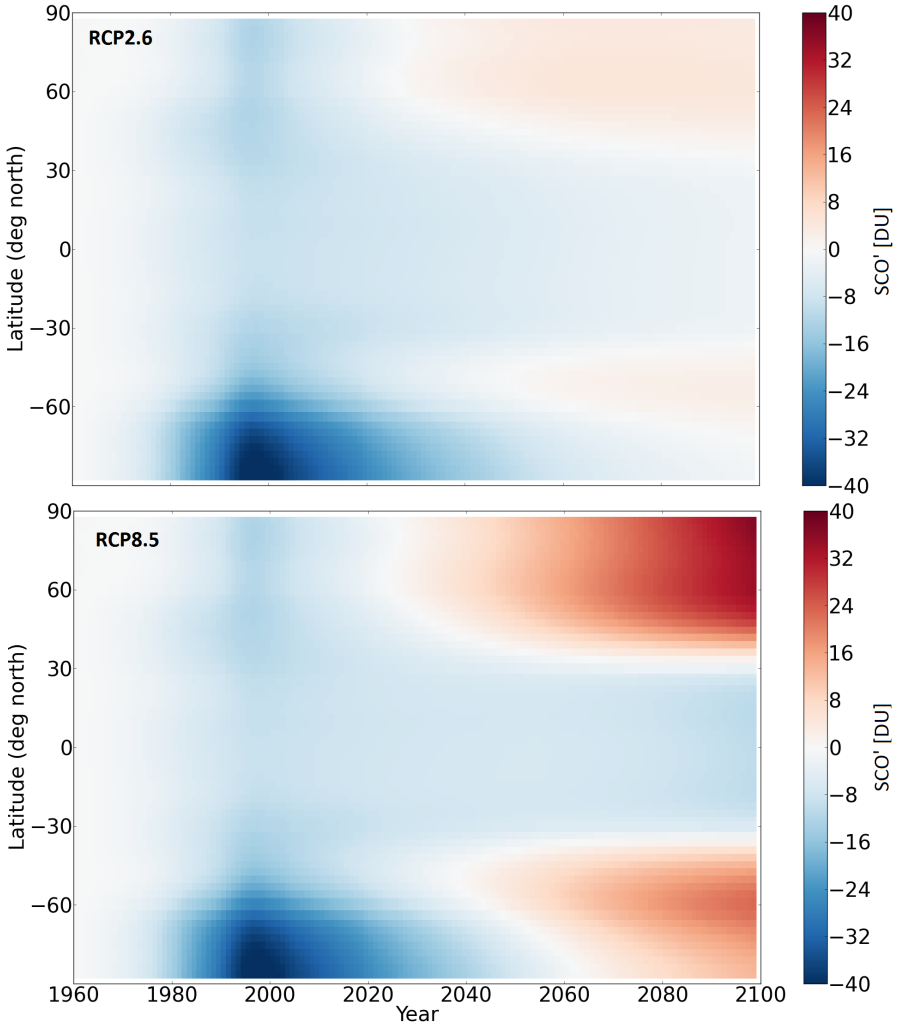

Figure 6.13: Annual mean zonal mean SCO′ (w.r.t. 1960 year baseline) for the years 1960 to 2100 calculated with MAGICC, with the new stratospheric module developed in this PhD thesis. The top panel shows SCO′ under the RCP2.6 emissions scenario and the bottom panel shows SCO′ under the RCP8.5 emssions scenario. Here MAGICC is tuned to the AOGCM MRI_CGCM2 and the carbon cycle BERN.

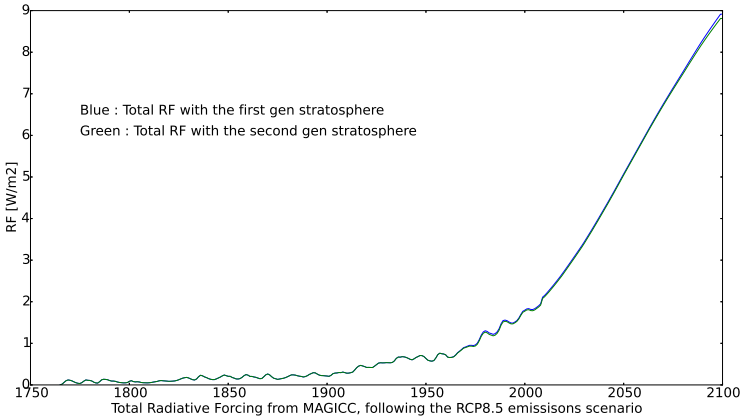

Figure 6.14: MAGICC calculated stratospheric RF using the old stratospheric module (blue) and new stratospheric module (green line).

new stratospheric module (the new module presented in this chapter). The new stratospheric module lower the stratospheric ozone RF slightly, especially in the end of the century, compared to the old stratospheric module.

7

CONCLUSION AND FUTURE WORK

The goal of this thesis was to use simple models to improve understanding of components of the atmosphere. Models with three levels of complexity were used: a simple climate model (SCM), an energy balance model (EBM) and semi-empirical regression models.

To start with, a stratospheric ozone module, consisting of a semi-empirical model, was developed and implemented into the SCM MAGICC. MAGICC has been used in the IPCC reports to emulate the projections of future climate change conducted with complex AOGCMs, allowing investigations of temperature and sea level changes for many different emissions scenarios (Randall et al., 2007a).

The intention with extending MAGICC to include stratospheric ozone that interacts with the climate system was to estimate the uncertainty ranges in stratospheric ozone projections, as a complement to studies where more complex climate models are used. In the semi-empirical model, a statistical method to simulate the dependence of stratospheric column ozone (SCO) on EESC and CO_2 was used.
In this project MAGICC, with the new stratospheric module, was used to emulate 18 different AOGCMs and 10 carbon cycle models to simulate ensembles of SCO abundances and years of return to pre-industrial levels, for four representative concentration pathway (RCP) emissions scenarios. This gives a total of 720 simulations, which would have taken years for more com-

plex climate models to run, but was simulated within only a few seconds with this new fast emulator.
It was found that SCO in the mid- to high latitudes will return to 1960 levels more quickly when the grenhouse gas (GHG) emissions are higher. However in the equatorial regions SCO will not return to 1960 levels before the end of the century. Furthermore, in the equatorial regions SCO decreases more rapidly for higher GHG emissions scenarios. The spread in return years of SCO to 1960 levels is larger for lower GHG emissions scenarios, with the largest spread around 40°N/S and in the southern high latitudes.

There is a larger spread in SCO projections for higher GHG emissions scenarios. The MAGICC simulations suggest that the spread in SCO projections are largest in the polar regions, followed by the equatorial regions and the mid-latitudes.

SCO was implemented into MAGICC to represent the coupling to the climate system, via radiative forcing (RF). On a global scale, RF from ozone changes are projected to increase in the future (Bekki et al., 2013). Earlier studies suggest that in the low latitudes RF associated with ozone is negative in the end of the century, while in mid-latitudes and polar regions, RF is projected to be positive (Bekki et al., 2013). The output from MAGICC,presented in Chapter 6, is in agreement with earlier work, and shows that in the mid-latitudes and polar regions, RF associated with SCO is negative before the middle of the century, when SCO abundances are below pre-industrial levels, and becomes positive in the end of the century, when SCO increases to above pre-industrial levels. A negative RF means an increase in outgoing longwave (LW) radiation at the top of the atmosphere (TOA), and a cooling of the surface temperature. A positive RF means that more shortwave (SW) is coming into the Earth than LW leaving it, which leads to a warming of the surface temperature.

Stratospheric ozone RF is smaller for lower GHG emissions, when SCO levels are lower. In the equatorial regions RF stays

negative, with RF simulated under higher emissions scenarios more negative than RF simulated under lower emissions scenarios. The largest changes in future stratospheric ozone levels are expected to be found in the lower stratosphere (Eyring et al., 2013), and this is also where the largest contribution from stratospheric ozone to RF origin from (Lacis et al., 1990). The largest spread in RF is found in the equatorial regions for the higher emissions scenarios, while the smallest spread is found in the polar regions for the lower emissions scenarios. The larger spread in SCO abundances for higher GHG emissions scenarios is associated with a larger spread in CO_2.

Both SCMs and EBMs provide conceptual pictures of climate processes without the complicated details of GCMs. To make accurate predictions of e.g. local temperature changes due to changes in anthropogenic emissions the level of detail often found in GCMs is necessary. However, the complexity of GCMs makes it difficult to unravel cause and effect, e.g. to understand the effects from single processes on the climate system. In order to understand the climate system, a range of model complexity is therefore useful. EBMs are in general less complex than SCMs, and after the stratospheric module was implemented into MAGICC, the focus of this PhD project shifted towards the core of most climate models: EBMs.

The overall problem investigated in this work was to investigate the non-linear interactions between surface albedo, water vapour and clouds, and the effects they have on amplified warming in the polar regions. One advantage of EBMs is that it is possible to isolate some climate processes in order to study their effects on the climate system independent of other processes. The EBM developed in this PhD project for this purpose is described in terms of thermodynamics (i.e. temperature) and is a two-layer model, with a surface layer and an atmospheric layer, heat transport and with a simple radiative scheme based on Stefan-Boltzmann's radiation law. The heat transport is described by diffusive processes, a method commonly used in the literature (Shell and Sommerville, 2005; Rose and Marshall,

2009). In this EBM the main climate variables are surface albedo, water vapour, cloud cover fraction and cloud albedo. These climate variables are implemented in a way that allow them to vary or keep them at fixed reference levels, so that each climate variable can be studied in isolation from the others. Thereby it is possible to study the effects from different climate variables on the other variables and on the climate system.

In the EBM presented in this thesis, the surface albedo is represented by a simple cut-off temperature, as in the early work of Budyko (1968). The absorption of water vapour and CO_2 in the atmosphere is described by the simple approximation used by Barker and Ross (1999). A simple regression model, similar to the methodology used to add SCO into MAGICC, is used to determine the dependence of cloud cover fraction on relative humidity, lapse rate and latent heat fluxes. In Chapter 4 the cloud albedo is fixed. However, research has suggested that the cloud albedo feedback mechanism represents a powerful climate feedback that can even control the sign of the net cloud feedback simulated in GCMs (Storelvmo et al., 2015). Output from GCMs suggest that feedbacks associated with cloud phase changes, and therefore cloud albedo, are the dominant cloud feedbacks especially in high latitudes (Storelvmo et al., 2015).

In Chapter 5 the EBM is extended to include cloud albedo that changes with phase change in clouds, i.e. with changing amount of ice crystals and water droplets in the cloud. The amount of ice crystals and water droplets is determined by the cloud temperature. Generally liquid clouds consist of a high number of relatively small water droplets (10 µm), while ice clouds consist of fewer but larger ice crystals (100 µm) (Pruppacher and Klett, 2010). Therefore, for a given water content, liquid clouds are usually more opaque compared to ice clouds leading to a higher albedo. A warming atmosphere will have an increasing amount of liquid clouds, at the expense of ice clouds resulting in a higher albedo.

In this EBM the cloud albedo is, just like the surface albedo,

represented by simple cut-off temperatures, one for the transition from total glaciation in clouds (all ice crystals) to mixed phase (ice crystals and water droplets), and one temperature for transition from mixed phase to all water droplets. The cloud top temperature in the EBM depends on the lapse rate and the atmospheric temperature.

The EBM was run under doubled or quadrupled CO_2 loading with surface albedo, water vapour and cloud cover either activated (i.e. allowed to change with changing temperatures) or inactive, i.e. prescribed with values from a reference run. Furthermore, in the work presented in Chapter 5, all different combinations of activated/inactive climate variables were run with activated and inactive cloud albedo. The EBM is always run to equilibrium, and each one of these sixteen simulations takes only a couple of seconds to run.

The output from the EBM simulations suggest that surface albedo contributes more than water vapour and cloud cover to the amplified warming in the polar regions. Surface albedo primarily regulates the surface absorption of incoming SW radiation, especially in the high latitudes where the sea ice cover is significantly reduced. However it also affects the LW fluxes, since a warmer surface (from increased absorbed SW radiation) emits more LW radiation back to the atmosphere and out to space. More LW radiation is absorbed by and therefore warms the atmosphere, and the following increase in backemitted LW radiation further warms the surface. This interaction of relatively large changes in SW and LW fluxes causes a strong surface albedo feedback. Furthermore, the warming effect from surface albedo in the polar regions causes a decrease in temperature difference between the equatorial and polar regions, i.e. decreases in the meridional temperature gradient, and therefore the meridional transport of heat. This leaves more heat in the equatorial regions, and partly dampens the warming effect in the polar regions.

Consistent with previous findings (Graversen and Wang, 2009),

it was found that for an increase in CO_2 loading in the atmosphere, the warming effect from decreasing surface albedo in the polar regions is strongly enhanced by increasing cloud cover and water vapour, when these variables are allowed to vary. Water vapour affects the LW components of the radiative fluxes, while cloud cover has an impact on both the SW and LW radiation (Marshall and Plumb, 2007). The atmospheric temperature raises when the amount of CO_2 is increased which causes more LW radiation to be backemitted to the surface. The surface warms and, according to the Clausius-Clapeyron relation, the warmer air is able to hold more water vapour. As a consequence, more LW radiation is absorbed by the water vapour in the atmosphere. The atmospheric temperature is further increased and therefore emits more LW radiation back to the surface. The output from the EBM simulations shows that the warming effect from water vapour is stronger in the equatorial regions compared to the polar regions, since the CO_2-induced increase in total column water vapour is larger in the equatorial regions.

In this model the warming effect from a CO_2 induced increase in absorption of LW radiation due to increased cloud cover dominates over the cooling effect from increase in SW radiation associated with increasing cloud cover. Increasing cloud cover thus leads to an increase in surface temperature. The output from this EBM suggest a large increase in cloud cover in the polar regions, and a small decrease in cloud cover in the lower latitudes, resulting in a cooling of the surface temperature.

For a doubling of CO_2, on a global scale the activation of the cloud albedo feedback damps the surface temperature increase for the simulation where all three feedbacks are activated in our EBM. This is an agreement with the results presented by Mitchell et al. (1989), where the effects of phase changes, when included in a GCM, suggested a halving of the simulated climate sensitivity. According to the output from our EBM, on a global scale and in the equatorial regions, the simulations where surface albedo feedback is activated, suggest a damping

of the surface temperature increase when cloud albedo is activated. The cloud albedo feedback has the largest effect in the polar regions, which is also in agreement with earlier work () In the polar regions the surface temperature increase is enhanced for all simulations except for the simulation where surface albedo, water vapor and clouds interact and the simulation when cloud cover is prescribed, due to decreases in net SW radiation reflected from clouds.

The decrease in temperature in clouds found in the high latitudes contribute to lower cloud albedo (due to an increase in fraction of ice crystals), while in the low latitudes the simulated increase in cloud temperature leads to a higher cloud albedo (due to an increase in fraction of water droplets). In the EBM presented in Chapter 5 there are only two critical temperatures for phase transitions, and therefore the change in cloud albedo lacks a detailed geographical distribution. However, the results presented here point toward the importance of representing the reflectivity of clouds and changes of reflectivity of clouds correctly in climate models, as is also pointed out in the work of Storelvmo et al. (2015).

Clouds are a critical part of the climate system of Earth, since they exert a strong radiative cooling on the surface, as well as warming depending on cloud type and optical thickness (Stephens et al., 2012). Changes in cloud amount, cloud height, cloud condensation nuclei and cloud radiative properties such as reflection of SW and absorption of LW radiation are all important contributions to cloud feedbacks. Changes in cloud radiative effects can be decomposed by cloud type, for example through altitude and optical thickness. Different mechanisms and processes responsible for cloud responses to RF in different regimes. Because of the large number of different cloud types and regimes and the dependence of clouds on both micro and macro physical influences, cloud feedback on climate represents the largest uncertainty in climate modeling. The feedback associated with phase changes in clouds is a powerful feedback, even controlling the sign of the overall feedback, yet not well

understood.

In the simple EBM presented in Chapter 5 GHG-induced changes in cloud reflectivity depend not only on the temperature of clouds but also on the area from which the SW radiation is reflected. Changes in albedo are thus enhanced/ damped depending on if the cloud cover fraction is increased or decreased. The output from the EBM presented here shows that where the LW radiation is small, e.g. when the interaction between positive feedbacks such as surface albedo, water vapour or cloud cover feedbacks are weaker, the effect from cloud albedo feedback becomes more important. According to the EBM simulations studied here, the cloud albedo feedback has the greatest impact on the cloud cover feedback, followed by the water vapor and the surface albedo feedbacks.

One of the main findings in this project is that the sums of CO_2-induced EBM simulated surface temperature changes due to any variable (viz surface albedo, water vapour or cloud cover) considered in isolation are smaller than the temperature changes from coupled feedback simulations. This points towards non-linear behaviour in the feedbacks associated with these three variables. It was found that surface albedo is the strongest driver of this non-linearity, followed by water vapour and cloud cover. The strongest non-linear behaviour is found when all three climate variables interact. This is because the increase in LW radiation absorbed by the surface, associated with changes in water vapour and cloud cover, and increases in SW radiation, related to decrease in surface albedo, amplify each other. The non-linearities are stronger in the polar regions compared to in the lower latitudes.

7.1 FUTURE WORK

7.1.1 *Representation of Antarctic ozone in MAGICC*

Even though the work presented in this PhD thesis is complete, there is room for improvements and development. The model described in Chapter 6 is very sensitive to changes in CO_2 (see Table 6.3). However according to Eyring et al. (2013), over Antarctica in September, the sensitivity of ozone to the GHG scnenario is generally not very high. This results in very similar evolution of stratospheric column ozone over the 21^{st} century in different RCP's. The method to calculate SCO described in Chapter 6 is good on a global scale, but is rather poor in the high latitudes since it does take into account the effect from polar stratospheric clouds, and does not describe for example stratospheric sudden warming and other interannual extreme events well. Therefore the sensitivity to changes in CO_2 in our model is likely overestimated in the Antarctic region. This result in differences between RCP emissions scenarios that are likely too large.

A stratospheric semi-empirical model referred to as semi-empirical weighted iterative fit technique (SWIFT) (Rex et al., 2013) could be implemented in MAGICC to cover the high latitudes of the globe. SWIFT comprises a set of coupled first order differential equations describing the time rate of change of key species in the polar stratosphere, including HNO_3, HCl, $ClONO_2$, ClO_x and ozone. It describes the time evolution of these prognostic variables throughout the polar winter starting from prescribed initial conditions. SWIFT is driven by a time series of fractional area of polar stratospheric clouds (FAP), i.e. the fraction of vortex with temperatures below 195 K (the threshold temperature for formation of polar stratospheric clouds (PSCs)) and fractional area of sunlight (FAS), i.e. the fraction of the vortex exposed to sunlight. FAP would be calculated from stratospheric temperature fields, with a method called stratospheric temperature pattern scaling (STePS).

STePS would require input in the form of CO_2 and SCO fields, in order to calculate stratospheric temperature fields. The functional dependence of stratospheric temperature on CO_2 and ozone anomalies would be determined based on a similar concept as for SCO, as described in Chapter 6,

$$T'_{strat,j} = \alpha_j CO'_2 + \beta_j SCO'_j + \varepsilon_j \tag{7.1}$$

where α, β and ε are fit coefficients derived individually for each latitude (denoted by j subscripts), $T'_{j\,strat,j}$ is the perturbation in temperature in the Antarctic stratosphere with respect to some baseline, CO'_2 and SCO' are perturbations in vortex averaged CO_2 and stratospheric column ozone concentrations with respect to the same baseline. The temperature fields would be calculated on a monthly basis, to catch the extreme stratospheric events, and therefore monthly mean CO_2 and SCO would be required. From these temperature fields FAP would be calculated in STePS and sent into SWIFT, new ozone fields are calculated within SWIFT, and sent back to STePS.

7.1.2 *Representation of gases other than CO_2 in the stratospheric module in MAGICC*

In the work presented in Chapter 6, CO_2 is used as a proxy for statospheric temperature and climate related effects on SCO, while EESC represent effects from the ODSs on SCO abundances. However, future evolution of stratospheric ozone is affected not only by CO_2 and EESC, but also by other GHGs with nitrous oxide (N_2O) and methane (NH_4) probably playing the dominant roles, especially when halocarbons return toward pre-industrial levels in the middle to end of the century.

Garny et al. (2013) suggest that the earlier return of stratospheric ozone to 1980 levels are caused by

1. stronger increases in ozone production due to enhanced NO_x concentrations in the Northern Hemisphere (lower stratosphere and upper troposphere),

2. stronger decreases in destruction rates of ozone by the NO_x cycle in the Northern Hemisphere (lower stratosphere) linked to effects of dynamics and temperature on NO_x concentrations, and
3. increasing efficiency of heterogeneous ozone destruction by Cl_y in the Southern Hemisphere mid-latitudes as a result of decreasing lower stratospheric temperatures

In the model described in Chapter 6, CO_2 is used as a proxy for stratospheric temperatures, and EESC to represent the destruction of ozone due to chlorine and bromine compounds. Thereby there is no spread in the simulations due to NO_x. This causes a relatively small spread in return years between GHG emissions scenarios in the Northern Hemispere.

N_2O is relatively inert in the troposphere, and is transported to the stratosphere, where it is broken down via photolysis according to the following (Portmann, Daniel, and Ravishankara, 2012),

$$N_2O + h\nu \rightarrow N_2 + O\bullet \tag{7.2}$$

$$N_2O + O\bullet \rightarrow N_2 + O_2 \tag{7.3}$$

$$N_2O + O\bullet \rightarrow 2NO \tag{7.4}$$

NO produced in Eq. 7.4, just like e.g. chlorine (Cl) and hydrogen oxide (HO), destroys ozone in the stratosphere through the following catalytic processes (Portmann, Daniel, and Ravishankara, 2012),

$$X + O_3 \rightarrow XO + O_2 \tag{7.5}$$

$$XO + O \rightarrow X + O_2 \tag{7.6}$$

where X = NO, HO, Cl. The X molecule is able to destroy many ozone molecules before it is removed from the stratosphere.

While N_2O causes ozone depletion, methane (CH_4) causes ozone increases by converting active chlorine (Cl) to a chlorine reservoir (HCl) that does not directly destroy ozone (Portmann, Daniel, and Ravishankara, 2012),

$$Cl + CH_4 \rightarrow HCl + CH_3 \tag{7.7}$$

This means that an increase in methane will decrease active chlorine that otherwise would have reacted with ozone. Global ozone loss would thus have been larger if there was no increase in methane.

In future work and further development of the SCM, other gases that affect stratospheric ozone concentrations such as methane and nitrogen oxide, could be added to the regression model presented in Chapter 6 (Eq. 6.1). Thereby contributions to uncertainties from methane and nitrogen oxide could be estimated along with CO_2 and EESC.

By fitting Eq. 6.1 to output from the EMAC model, the effect from the Brewer-Dobson circulation (BDC) on the relationship between CO_2, EESC' and SCO' is included in our EBM. However, climate models display a wide range of responses of the BDC to climate change.

To capture the full range of responses of the BDC to climate change across different CCMs, the method presented here could be used in the future to emulate a range of CCMs.

7.1.3 *Representation of cloud properties in the EBM*

The first version of the EBM (presented in Chapter 4) incorporates surface albedo, water vapour and cloud cover. Cloud properties such as emissivity and albedo are omitted. In Chapter 5 the EBM was extended with cloud albedo that changes with changing cloud temperure is presented. The representation of cloud albedo in the EBM developed in this PhD project is very simple, however it is useful as the output gives an indication of how changes in cloud albedo affects other feedbacks. Since only two cut-off temperatures are used, the geographic representation is limited.
The cloud albedo in the EBM could be developed so that it depends on e.g. the cloud water path. The cloud water path is determined by the amount of water in the column of the cloud, which depends on the thickness of the cloud. The amount of water in the column of the cloud depends on cloud temperature. For example, cooler clouds contain more ice crystals and less water droplets.

In the current version of this EBM, cloud emissivity is set to a constant. Emissivity of clouds that vary with changes in the climate system could also be implemented in the EBM. According to Chýlek and Ramaswamy (1981), the emissivity of clouds can be expressed in terms of ice water path (IWP) in clouds,

$$\varepsilon_c = 1 - e^{-DK_{abs}IPW} \tag{7.8}$$

where D is a diffusivity factor, k_{abs} is the LW absorption coefficient, IPW depends on temperature. The absorption coefficient k_{abs} can be defined as

$$k_{abs} = k_l(1 - f_{ice}) + k_i f_{ice} \tag{7.9}$$

where f_{ice} is the ice/water fraction in clouds, k_l is the LW absorption coefficient for liquid water, and can be expressed as (Ebert and Curry, 1992)

$$k_i = 0.005 + 1/r_{ei} \tag{7.10}$$

where r_{ei} is the effective radius of the ice crystal distribution.

Even though implementation of more sophisticated cloud properties such as albedo and emissivity would expand the use of the EBM, it would also increase its complexity. This could possibly be an interesting topic for future work.

Furthermore, in the EBM developed during this PhD project, the cloud cover depends on relative humidity, lapse rate and latent heat flux. It is assumed that changes in these climate processes are insensitive to the geographic distribution of cloud changes. An attempt to investigate the geographical distribution of the sensitivity was made, however it was difficult to find a trend in cloud cover changes over the time period in the ERA-Interim data set. Improvement of the geographical sensitivity of cloud cover to the processes governing the creation of clouds could also be a topic for future work on this EBM, however this would also increase the complexity of the model.

The EBM presented in Chapters 4 and 5 could be a useful too for educational purposes. One idea is to develop an online interface which would allow students or public to run the model with different settings, and thereby get an insight into how different components of the climate system interact and how they affect the surface temperature on Earth.

BIBLIOGRAPHY

Alduchov, O. A. and R. E. Eskridge, 1995: Improved magnus form approximation of saturation vapor pressure. *J. Appl. Meteorol.*, **35**, 601–609.

Alexeev, V. A. and C. H. Jackson, 2013: Polar amplification: is atmospheric heat transport important? *Clim. Dyn.*, **41**, 533–547.

Alexeev, V. A., P. L. Langen, and J. R. Bates, 2005: Polar amplification of surface warming on an aquaplanet in "ghost forcing" experiments without sea ice feedbacks. *Clim. Dyn.*, **24**, 655–666, doi:10.1007/s00382-005-0018-3.

Arblaster, J. M., N. P. Gillett, et al., 2014: Stratospheric ozone changes and climate, chapter 4 in *Scientific Assessment of Ozone Depletion:2014*. Tech. rep., Global Ozone Research and Monitoring Project - Report No. 55, World Meteorological Organization, Geneva, Switzerland.

Armour, K. C., E. Blanchard-Wrigglesworth, and M. K. E., 2011: The reversibility of sea ice loss in a state-of-the-art climate model. *Geophys. Res. Lett.*, **38**, L16 705.

Barker, J. R. and M. H. Ross, 1999: An introduction to gloabal warming. *Am. J. Phys.*, **67**, 1216–1226.

Bates, J. R., 2016: Estimating climate sensitivity using two-zone energy balance models. *Earth and Space Science*, **3**, 207–225, doi:10.1002/2015EA000154.

Bekki, S. et al., 2013: Climate impact of stratospheric ozone recovery. *Geophys. Res. Let.*, **40**, 2796–2800, doi:10.1002/grl50358.

Bekryaev, R. V. et al., 2010: Role of polar amplification in long-term surface air temperature variations and modern arctic

warming. *J. Climate*, **23**, 3888–3906, doi:10.1175/2010JCLI3297.1.

Bell, J., 2013: URL https://www.acs.org/content/acs/en/climatescience/energybalance.html.

Bendtsen, J., 2002: Climate sensitivity to changes in solar insolation in a simple coupled climate model. *Clim. Dyn.*, **18**, 595–609, doi:10.1007/s00382-001-0198-4.

Bindoff, N. L. et al., 2013: *Climate change 2013: The physical science basis. Contribution of working group I to the fifth assessment report of the intergovernmental panel on climate change*, chap. Detection and attribution of climate change. Cambridge University Press, Cambridge, United Kingdom and New York, NY, USA, doi:10.1017/CBO9781107415324.022.

Birner, T. et al., 2006: The tropopause inversion layer in models and analyses. *Geophys. Res. Lett.*, **33**, L14 804, doi:10.1029/2006GL026549.

Bony, S. et al., 2006: How well do we understand and evaluate climate change feedback processes? *J. Climate*, **19**, 3445–3482, doi:10.1175/JCLI3819.1.

Boucher, O. et al., 2013: *Clouds and aerosols. In: Climate change 2013: The physical science basis. Contribution of working group I to the fifth assessment report of the intergovernmental panel on climate Change*. Cambridge University Press, Cambridge, United Kingdom and New York, NY, USA.

Budyko, M. I., 1968: Effect of solar radiation variations on climate of earth. *Tellus*, **21**, 611–619.

Butchart, N., 2014: The brewer-dobson circulation. *Rev. Geophys.*, **52**, 157–184, doi:10.1002/2013RG000448.

Cai, M., 2005: Dynamical amplification of polar warming. *Geophys. Res. Lett.*, **32**, L22 710, doi:10.1029/2005GL024481.

Cai, M. and K. K. Tung, 2012: Robustness of dynamical feedbacks from radiative forcing: 2% solar versus $2\times co_2$ experiments in an idealized gcm. *J. Atmos. Sci.*, **69**, 2246–2271.

Carpenter, L. J., S. Reimann, et al., 2014: Ozone-depleting substances (odss) and other gases of interest to the montreal protocol, chapter 1 in *Scientific Assessment of Ozone Depletion: 2014*. Tech. rep., Global Ozone Research and Monitoring Project - Report No. 55, World Meteorological Organization, Geneva, Switzerland.

Cesana, G. and Storelvmo, 2007: Improving climate projections by understanding how cloud phase affects radiation. *J. Geophys. Res. Atmos.*, **122**, 4594–4599, doi:10.1002/2017JD026927.

Cess, R. D. and G. L. Potter, 1991: Interpretation of snow-climate feedback as produced by 17 general circulation models. *Science*, **253**, 888–892.

Cess, R. D. et al., 1996: Cloud feedback in atmospheric general circulation models: An update. *J. Geophys. Res.*, **101**, 12 791–12 794.

Charlton-Perez, A. J. et al., 2010: The potential to narrow uncertainty in projections of stratospheric ozone over the 21st century. *Atmos. Chem. Phys.*, **10**, 9473–9486, doi:10.5194/acp-10-9473-2010, URL http://dx.doi.org/10.5194/acp-10-9473-2010.

Charney Report, K., 1979: Carbon dioxide and climate: A scientific assessment. Tech. rep., National Academy of Sciences, Washington D. C.

Chipperfield, M. P., V. E. Fioletov, et al., 2007: Global ozone: Past and present, chapter 3 in *Scientific Assessment of Ozone Depletion:2006*. Tech. rep., Global Ozone Research and Monitoring Project - Report No. 50, World Meteorological Organization, Geneva, Switzerland.

Choi, Y. S. et al., 2014: Influence of cloud phase composition on climate feedbacks. *J. Geophys. Res. Atmos.*, **119**, 3687–3700, doi:10.1002/2013JD020582.

Chýlek, P. and J. A. Coakley, 1975: Analytical analysis of a budyko-type climate model. *J. Atmos. Sci.*, **32**, 675–679.

Chýlek, P. and V. Ramaswamy, 1981: Simple approximation for infrared emissivity of water clouds. *J. Atmos. Sci.*, **39**, 171–177.

Cionni, I. et al., 2011: Ozone database in support of cmip5 simulations: results and corresponding radiative forcing. *Atmos. Chem. Phys.*, **11**, 11 267–11 292.

Collins, M. et al., 2013: *Climate change 2013: The physical science basis. Contribution of working group I to the fifth assessment report of the intergovernmental panel on climate change*, chap. Long-term climate change: Projections, commitments and irreversibility. Cambridge University Press, Cambridge, United Kingdom and New York, NY, USA, doi:10.1017/CBO9781107415324.024.

Colman, R., 2003: A comparison of climate feedbacks in general circulation models. *Clim. Dynam.*, **20**, 865–873.

Crook, J. A. and P. M. Foster, 2014: Comparison of surface albedo feedback in climate models and observations. *Geophys. Res. Lett.*, 1717–1723, doi:10.1002/2014GL059280.

Daniel, J. S. et al., 1999: Stratospheric ozone destruction: The importance of bromine relative to chlorine. *J. Geophys. Res.*, **104**, 23,871–23,880.

Daniel, J. S. et al., 2007: Halocarbon scenarios, ozone depletion potentials, and global warming potentials, chapter 8 in *Scientific Assessment of Ozone Depletion:2006*. Tech. rep., Global Ozone Research and Monitoring Project - Report No. 50, World Meteorological Organization, Geneva, Switzerland.

Dee, D. P. et al., 2011: The era-interim reanalysis: configuration and performance of the data assimilation system. *Q. J. R. Meteorol. Soc.*, **137**, 553–597, doi:10.1002/qj.828.

Dines, W. H., 1917: The heat balance of the atmosphere. *Q. J. Roy. Meteor. Soc.*, **43**, 151–158, doi:10.1002/qj.49704318203.

Ebert, E. E. and J. A. Curry, 1992: A parametrization of ice cloud optical properties for climate models. *J. Geophys. Res.*, **97**, 3831–3836.

Eyring, V. et al., 2006: Assessment of temperature, trace species, and ozone in chemistry-climate model simulations of the recent past. *Journal of Geophysical Research*, **11**, D22 308.

Eyring, V. et al., 2007: Multimodel projections of stratospheric ozone in the 21st century. *Journal of Geophysical Research*, **112**, D16 303.

Eyring, V. et al., 2010a: Multi-model assessment of stratospheric ozone return dates and ozone recovery in ccmval-2 models. *Atmos. Chem. Phys.*, **10**, 9451–9472, doi:10.5194/acp-10-9451-2010.

Eyring, V. et al., 2010b: Sensitivity of 21st century stratospheric ozone to greenhouse gas scenarios. *Geophys. Res. Lett.*, **37**, L16 087.

Eyring, V. et al., 2013: Long-term ozone changes and associated climate impacts in cmip5 simulations. *J. Geophys. Res.-Atmos.*, **118**, 5029–5060, doi:10.1002/jgrd.50316.

Fasullo, J. T. and K. E. Trenberth, 2008: The annual cycle of the energy budget. part ii: Meridional structures and poleward transports. *J. Climate*, **21**, 2,313–2,325.

Flannery, B. P., 1984: Energy balance models incorporating transport of thermal and latent energy. *J. Atmos. Sci.*, **41**, 414–421.

Flato, G. et al., 2013: *Evaluation of climate models. In: Climate change 2013: The physical science basis. Contribution of working group I to the fifth assessment report of the intergovernmental panel on climate change*. Cambridge University Press, Cambridge, United Kingdom and New York, NY, USA.

Forbes, R. M. and M. Ahlgrimm, 2014: On the representation of high-latitude boundary layer mixed-phase cloud in the ecmwf global model. *Amer. Meteorological Soc.*, **142**, 3425–3455, doi:10.1175/MWR-D-13-00325.1.

Forster, P. M. and K. P. Shine, 1997: Radiative forcing and temperature trends from stratospheric ozone changes. *J. Geophys. Res.*, **102**, 10 841–10 845.

Fourier, J. B., 1827: On the temperatures of the terrestrial sphere and interplanetary space. *M'emoires d l'Academie Royale des Sciences de l'Institute de France*, **7**, 570–604, URL http://books.google.com/books?hl=en&lr=&id=lhzK1-woaiQC&oi=fnd&pg=PA7&dq=On+The+Temperatures+of+the+Terrestrial+Sphere+and+Interplanetary+Space&ots=Ok5MXfmZVn&sig=l63bw8_IHL2mPYjApO2l7pw2jVQ.

Friedlingstein, P. et al., 2006: Climate-carbon cycle feedback analysis: Results from the c^{4}mip model intercomparison. *J. Climate*, **19**, 3337–3353.

Garny, H. et al., 2013: Drivers of hemispheric differences in return dates of mid-latitude stratospheric ozone to historical levels. *Atmos. Chem. Phys.*, **13**, 7279–7300, doi:10.5194/acp-13-7279-2013.

Gauss, M. et al., 2006: Radiative forcing since preindustrial times due to ozone change in the troposphere and the lower stratosphere. *Atmos. Chem. Phys.*, **6**, 575–599.

Gille, S. T., 2008: Decadal-scale temperature trends in the southern hemisphere ocean. *J. Climate*, **21**, 4749–4765, doi:10.1175/2008JCLI2131.1.

Graversen, R. G., P. L. Langen, and T. Mauritsen, 2014: Polar amplification in ccsm4: Contributions from the lapse rate and surface albedo feedbacks. *J. Climate*, **27**, 4433–4450, doi:10.1175/JCLI-D-13-00551.1.

Graversen, R. G. and M. Wang, 2009: Polar amplification in a coupled climate model with locked albedo. *Clim. Dyn*, **33**, 629–643, doi:10.1007/s00382-009-0535-6.

Gregory, J. and M. Webb, 2007: Tropospheric adjustment induces a cloud component in co_2 forcing. *J. Climate*, **21**, 58–71, doi:10.1175/2007JCLI1834.1.

Gregory, J. M. et al., 2004: A new method for diagnosing radiative forcing and climate sensitivity. *Geophys. Res. Lett.*, **31**, L03 205, doi:10.1029/2003GL018747.

Hagihara, Y. et al., 2014: Joint analysis of cloud top heights from cloudsat and calipso: New insights into cloud top microphysics. *Geophys. Res. Atmos.*, **119**, 4087–4106, doi:10.1002/2013JD020919.

Hall, C. M. et al., 2011: Tropopause height at 78° n and 16° e: average seasonal variation 2007-2010. *Atmos. Chem. Phys.*, **11**, 5485–5490.

Hansen, J. et al., 1997: Radiative forcing and climate response. *Journal of Geophysical Research*, **102**, 6831–6864.

Harvey, L. D. D., 1989: Managing atmospheric co_2. *Climatic Change*, **15**, 343–381.

Hegerl, G. and F. Zwiers, 2011: Use of models in detection and attribution of climate change, wires climate change. *Climate Change*, **2**, 570–591, doi:10.1002/wcc.121.

Held, I. M. and B. J. Soden, 2000: Water vapor feedback and global warming. *Annual Review of energy and the environment*, **25**, 441–475.

Held, I. M. and M. J. Suarez, 1974: Simple albedo feedback models of the icecaps. *Tellus*, **6**, 613–629.

Ho, C. H. et al., 1998: Effect of ice cloud on gcm climate simulations. *Geophys. Res. Lett.*, **25**, 71–74.

Hoffert, M. I., A. J. Callegari, and C. T. Hsieh, 1980: The role of deep sea heat storage in the secular response to climatic forcing. *J. Geophys. Res.*, **85**, 6667–6679.

Holland, M. M. and C. M. Bitz, 2003: Polar amplification of climate change in coupled models. *Clim. Dyn.*, **21**, 221–232.

Huck, P. E. et al., 2013: Semi-empirical models for chlorine activation and ozone depletion in the antarctic stratosphere: proof of concep. *Atmos. Chem. Phys.*, **13**, 3237–3243, doi:10.5194/acp-13-3237-2013.

Hulme, M. et al., 1995: An integrated framework to adress climate change (escape) and further developments of the global

and regional climate modules (magicc). *Energy Policy*, **23**, 347–355.

Ingram, W. J., C. A. Wilson, and J. F. B. Mitchell, 1989: Modeling climate change: An assessment of sea ice and surface albedo feedbacks. *J. Geophys. Res.*, **94**, 8609–8622.

Jeffries, M. O., J. Richter-Menge, and J. E. Overland, 2015: Executive summary, in: Arctic report card 2015. Tech. rep. URL http://www.arctic.noaa.gov/reportcard.

Jentch, V., 1991: An energy balance climate model with hydrological cycle 1. model description and sensitivity to internal parameters. *J. Geophys. Res.*, **96**, 17 169–17 179.

Jöckel, P., 2006: The atmospheric chemistry general circulation model echam5/messy1: consistent simulation of ozone from the surface to the mesosphere. *Atmos. Chem. Phys.*, **6**, 5067–5104, doi:10.5194/acpd-6-6957-2006.

Jonsson, A. I., 2004: Doubled co_2-induced cooling in the middle atmosphere: Photochemical analysis of the ozone radiative feedback. *J. Geophys. Res.*, **109**, D24 103, doi:10.1029/2004JD005093.

Kay, J. E. et al., 2014: Processes controlling southern ocean shortwave climate feedbacks in cesm. *Geophys. Res. Lett.*, **41**, 616–622, doi:10.1002/2013GL058315.

Kay, J. E. et al., 2016: Global climate impacts of fixing the southern ocean shortwave radiation bias in the community earth system model (cesm). *J. Climate*, **29**, 4617–4636, doi:10.1175/JCLI-D-15-0358.1.

Knutson, T. R., F. Zeng, and A. T. Wittenberg, 2013: Multimodel assessment of regional surface temperature trends: Cmip3 and cmip5 twentieth-century simulations. *J. Climate*, **26**, 8709–8743.

Knutti, R. and M. A. Rugenstein, 2015: Feedbacks, climate sensitivity and the limits of linear models. *Phil. Trans. R. Soc. A.*, **373**, 20150 146.

Kremser, S. et al., 2014: Methodological aspects of a pattern-scaling approach to produce global fields of monthly means of daily maximum and minimum temperature. *Geosci. Model Dev.*, **7**, 249–266, doi:10.5194/gmd-7-249-2014.

Lacis, A. A. and J. E. Hansen, 1975: A parametrization for the absorption of solar radiation in the earth's atmosphere. *J. Atmos. Sci.*, **31**, 118–132.

Lacis, A. A. et al., 1990: Radiative forcing of climate by changes in the vertical distribution of ozone. *Journal of Geophysical Research*, **95**, 9971–9981.

Li, C., 2012: Deep-ocean heat uptake and equilibrium climate response. *Clim. Dyn.*, **40**, 1071–1086, doi:10.1007/s00382-012-1350-z.

Lian, M. S. and R. D. Cess, 1977: Energy balance climate models: A reappraisal of ice-albedo feedback. *J. Atmos. Sci.*, **34**, 1058–1062.

Lu, J. and M. Cai, 2010: Quantifying contributions to polar warming amplification in an idealized coupled general circulation model. *Clim. Dyn.*, **34**, 669–687, doi:10.1007/s00382-009-0673-x.

Manabe, S. and R. J. Stouffer, 1980: Sensitivity of a global climate model to an increase of co_2 concentration in the atmosphere. *J. Geophys. Res.*, **85**, 5529–5554.

Manabe, S. and R. T. Wetherald, 1975: The effects of doubling of the co_2 concentrations on the climate of a general circulation model. *J. Atmos. Sci.*, **32**, 3–15.

Marshall, J. and R. A. Plumb, 2007: *Atmosphere, ocean and climate dynamics: An introductory text.* Academic Press, URL http://books.google.co.nz/books/about/Atmosphere_Ocean_and_Climate_Dynamics.html?id=KvJfvYBHiegC&pgis=1.

Meehl, G. A. et al., 2007a: *Climate Change 2007: The Physical Science Basis. Contribution of Working Group I to the Fourth Assessment Report of the Intergovernmental Panel on Climate Change*, chap. Global Climate Projections. Cambridge Univer-

sity Press, Cambridge, United Kingdom and New York, NY, USA.

Meehl, G. A. et al., 2007b: The wcrp cmip3 multi-model dataset: A new era in climate change research. *Bull. Am. Meteorol. Soc.*, **88**, 1383–1394, doi:10.1175/BAMS-88-9-1383.

Meinshausen, M., 2001: Long-term chlorine loading prediction. M.S. thesis, Institute for Atmosphere and Climate.

Meinshausen, M. et al., 2011a: Emulating atmosphere-ocean and carboncycle models with a simpler model, magicc-part 2: Applications. *Atmos. Chem. Phys.*, **11**, 1457–1471.

Meinshausen, M. et al., 2011b: Emulating coupled atmosphere-ocean and carboncycle models with a simpler model, magicc-part 1: Model description and calibration. *Atmos. Chem. Phys.*, **11**, 1417–1456.

Mitchell, J. F. B., C. A. Senior, and W. J. Ingram, 1989: Co_2 and climate: a missing feedback? *Nature*, **341**, 132–134.

Mitchell, T. D., 2003: Pattern scaling an examination of the accuracy of the technique for describing future climates. *Climatic Change*, **60**, 217–242.

Moss, R. H. et al., 2010: The next generation of scenarios for climate change research and assessment. *Nature*, **463**, 747–756, doi:10.1038/nature08823.

Myhre, G. et al., 1998: New estimates of radiative forcing due to well mixed greenhouse gases. *Geophys. Res. Lett.*, **25**, 2715–2718.

Myhre, G. et al., 2013a: *Anthropogenic and natural radiative forcing. In: Climate change 2013: The physical science basis. Contribution of working group I to the fifth assessment report of the intergovernmental panel on climate change*. Cambridge University Press, Cambridge, United Kingdom and New York, NY, USA, doi:10.1017/CBO9781107415324.018.

Myhre, G. et al., 2013b: *Climate Change 2013: The Physical Science Basis. Contribution of Working Group I to the Fifth Assessment*

Report of the Intergovernmental Panel on Climate Change, chap. Anthropogenic and Natural Radiative Forcing, 659–740. Cambridge University Press, Cambridge, United Kingdom and New York, NY, USA, doi:10.1017/CBO9781107415324.018.

Newman, P. A. et al., 2007: A new formulation of equivalent effective stratospheric chlorine (eesc). *Atmos. Chem. Phys.*, **7**, 4537–4522.

North, G. R., 1975a: Analytical solution to a simple climate model with diffuse heat transport. *Journal of the Atmospheric Science*, **32**, 1301–1307.

North, G. R., 1975b: Theory of energy-balance climate models. *J. Atmos. Sci.*, **32**, 2033–2043.

North, G. R. et al., 1981: Energy balance climate models. *Reviews of Geophysics and Space Physics*, **19**, 91–121.

Nowack, P. J. et al., 2015: A large ozone-circulation feedback and its implications for global warming assessments. *Nature Clim. Change*, **5**, 41–45, doi:10.1038/nclimate2451, URL http://dx.doi.org/10.1038/nclimate2451.

O'Gorman, P. A. and C. J. Muller, 2010: How closely do changes in surface and column water vapor follow clausius-clapeyron scaling in climate change simulations? *Environ. Res. Lett.*, **5**, 1–7, doi:doi:10.1088/1748-9326/5/2/025207.

Organization, W. M., 1992: International meteorological vocabulary (2nd ed.). 636 pp., Geneva: Secretariat of the World Meteorological Organization.

Paltridge, G. W. et al., 2007: Maximum entropy production, cloud feedback, and climate change. *Geophys. Res. Lett.*, **34**, L14 708, doi:doi:10.1029/2007GL029925.

Pawson, S., W. Steinbrecht, et al., 2014: Update on global ozone: Past, present, and future, chapter 3 in *Scientific Assessment of Ozone Depletion:2014*. Tech. rep., Global Ozone Research and Monitoring Project - Report No. 55, World Meteorological Organization, Geneva, Switzerland.

Payne, A. E. et al., 2015: Conceptual model analysis of the influence of temperature feedbacks on polar amplification. *Geophys. Res. Lett.*, **42**, 9561–9570, doi:10.1002/2015GL065889.

Pierrehumbert, R. T., 2002: The hydrologic cycle in deep-time climate problems. *Nature*, **419**, 191–198.

Pithan, F. and T. Mauritsen, 2014: Arctic amplification dominated by temperature feedbacks in contemporary climate models. *Nat. Geosci.*, **7**, 181–184, doi:10.1038/NGEO2071.

Portmann, R. W., J. S. Daniel, and A. R. Ravishankara, 2012: Stratospheric ozone depletion due to nitrous oxide: influences of other gases. *Phil. Trans. R. Soc. B*, **367**, 1256–1264, doi:10.1098/rstb.2011.0377.

Prather, M. et al., 1990: Global impact of the antarctic ozone hole-dynamic dilution with a 3-dimensional chemical-transport model. *J. Geophys. Res. Atmos.*, **95**, 3449–3471, doi:10.1029/JD095iD04p03449.

Pruppacher, H. and J. Klett, 2010: *Microphysics of clouds and precipitation.*, 954. Atmospheric and oceanographic science library, Dordrecht.

Randall, D. A. et al., 2007a: *Climate change 2007: The physical science basis. Contribution of working group I to the fourth assessment report of the intergovernmental panel on climate change*, chap. Climate models and their evaluation. Cambridge University Press, Cambridge, United Kingdom and New York, NY, USA.

Randall, D. A. et al., 2007b: *Climate Change 2007: The Physical Science Basis. Contribution of Working Group I to the Fourth Assessment Report of the Intergovernmental Panel on Climate Change*, chap. Climate models and their evaluation. Cambridge University Press, Cambridge, United Kingdom and New York, NY, USA.

Raper, S. C. B., 1996: Emulation of the results from a coupled general circulation model using a simple climate model. *Geophysical research letters*, **23**, 1107–1110.

Reichler, T. et al., 2003: Determining the tropopause height from gridded data. *Geophys. Res. Lett.*, **30**, 2042.

Rex, M. et al., 2013: Technical note: Swift - a fast semi-empirical model for polar stratospheric ozone loss. *Atmos. Chem. Phys.*, **13**, 31 607–31 634, doi:10.5194/acpd-13-31607-2013.

Rind, D., 1987: The doubled co_2 climate: Impact of the sea surface temperature gradient. *J. Atmos. Sci.*, **44**, 3235–3268.

Roads, J. O. and G. K. Vallis, 1984: An energy balance climate model with cloud feedbacks. *Tellus*, **36A**, 236–250.

Roe, G., 2009: Feedbacks, timescales and seeing red. *Annu. Rev. Earth Planet. Sci.*, **37**, 93–115.

Roe, G. H., F. N., A. K. C., H. Y.-T., and F. M. W., 2015: The remote impacts of climate feedbacks on regional climate predictability. *Nat. Geosci.*, **8**, 135–139, doi:10.1038/NGEO2346.

Rose, B. E. J. and J. Marshall, 2009: Ocean heat transport, sea ice, and mulitple climate states: Insight from energy balance models. *J. Atmos. Sci.*, **66**, 2828–2843.

Rossow, W. B. and R. A. Schiffer, 1999: Advances in understanding clouds from isccp. *Bull. Amer. Meteor. Soc.*, 2261–2288.

Salzmann, M., 2017: The polar amplification assymmetry: Role of antarctic surface height. *Earth Syst. Dynam. Discuss.*, 392–400, doi:10.5194/esd-2016-74.

Santer, B. D. et al., 2003: Contributions of anthropogenic and natural forcing to recent tropopause height changes. *Science*, 479–483.

Sausen, R. and B. D. Santer, 2003: Use of changes in tropopause height to detect human influences on climate. *Meteorologische Zeitschrift*, 131–136, doi:10.1127/0941-2948/2003/0012-0131.

Schneider, E. K., R. S. Lindzen, and B. P. Kirtman, 1997: A tropical influence on global climate. *J. Atmos. Sci.*, **54**, 1349–1358.

Schneider, E. K. et al., 1999: Tropospheric water vapor and climate sensitivity. *J. Atmos. Sci.*, **56**, 1649–1658.

Schneider, S. H., 1972: Cloudiness as a global climatic feedback mechanism: The effects on the radiation balance and surface temperature of variations in cloudiness. *J. Atmos. Sci.*, **29**, 1413–1422.

Screen, J. A. and I. Simmonds, 2010: The central role of diminishing sea ice in recent arctic temperature amplification. *Nature*, 1,334–1,337, doi:10.1038/nature0951.

Seidel, 2016: .

Sellers, W. D., 1969: A global climatic model based on the energy balance of the earth-atmosphere system. *Journal of Applied Meteorology*, **8**, 392–400.

Sellers, W. D., 1976: A two-dimensional global climatic model. *Mon. Weather Rev.*, **104**, 233–248.

Senior, C. A. and J. F. B. Mitchell, 1993: Carbon dioxide and climate: The impact of cloud parametrization. *J. Climate*, **6**, 393–418.

Serreze, M. C. and R. G. Barry, 2011: Processes and impacts of arctic amplification: A research synthesis. *Global and Planetary Change*, **77**, 85–96, doi:10.1016/j.gloplacha.2011.03.004.

Serreze, M. C. and J. A. Francis, 2006: The arctic amplification debate. *Clim. Change*, **76**, 241–264, doi:10.1007/s10584-005-9017-y.

Shell, K. M. and R. C. J. Sommerville, 2005: A generalized energy balance climate model with parametrized dynamics and diabatic heating. *J. Climate*, **18**, 1753–1772.

Shell, K. M. et al., 2008: Using the radiative kernel technique to calculate climate feedbacks in ncar's community atmospheric model. *J. Climate*, **21**, 2269–2282, doi:10.1175/2007JCLI2044.1.

Shepherd, T. G. and A. I. Jonsson, 2008: On attribution of stratospheric ozone and temperature changes to changes in ozone-depleting substances and well-mixed greenhouse gases. *Atmos. Chem. Phys.*, **8**, 1435–1444, doi:10.5194/acp-8-1435-2008.

Shine, K. et al., 1990: *Radiative forcing of climate*, chap. Climate change: The IPCC scientific assessment, 41–68. Cambridge University Press, New York, USA, doi:10.1017/CBO9781107415324.024.

Slingo, A. and J. M. Slingo, 1988: The response of a general circulation model to cloud longwave radiative forcing. i: Introduction and initial experiments. *Q. J. Roy. Meteor. Soc.*, **114**, 1027–1062, doi:10.1002/qj.49711448209.

Soden, B. J. and I. M. Held, 2006: An assessment of climate feedbacks in coupled ocean-atmosphere models. *J. Climate*, **19**, 3354–3360, doi:10.1175/JCLI3799.

Södergren, A. H., A. J. McDonald, and G. E. Bodeker, 2017: An energy balance model exploration of the impacts of the interactions between surface albedo, cloud cover and water vapor on polar amplification. *Clim. Dyn.*

Södergren, A. H. et al., 2016: A probabilistic study of the return of stratospheric ozone to 1960 levels. *Geophys. Res. Lett.*, **43**, 9289–9297, doi:10.1002/2016GL069700.

Stajner, I., 2008: Assimilated ozone from eos-aura: Evaluation of the tropopause region and tropospheric columns. *J. Geophys. Res.*, **113**, D16S32, doi:10.1029/2007JD008863.

Stephens, G. L., 2005: Cloud feedbacks ni the climate system: A critical review. *J. Climate*, **18**, 237–273.

Stephens, G. L. et al., 2012: An update on earth's energy balance in light of the latest global observations. *Nature Geosci.*, **5**, 691–696, doi:10.1038/ngeo1580.

Stocker, T. F. et al., 2013: *Climate change 2013: The physical science basis. Contribution of working group I to the fifth assessment report of the intergovernmental panel on climate change*, chap. Technical summary. Cambridge University Press, Cambridge, United Kingdom and New York, NY, USA, doi:10.1017/CBO9781107415324.005.

Stone, P. A., 1978: Baroclinic adjustments. *J. Atmos. Sci.*, 561–571.

Storelvmo, T. et al., 2015: Cloud phase changes induced by co_2 warming - a powerful yet poorly constrained cloud-climate feedback. *Curr. Clim. Change Rep.*, 288–296, doi:10.1007/s40641-015-0026-2.

Stubenrauch, C. J. et al., 2013: Assessment of global cloud datasets from satellites. *Am. Meteorol. Soc.*, doi:10.1175/BAMS-D-12-00117.1.

Thackeray, C. W. and C. G. Fletcher, 2016: Snow albedo feedback: Current knowledge, importance, outstanding issues and future directions. *Prog. Phys. Geog.*, **40**, 392–408, doi:10.1177/0309133315620999.

Trenberth, K. E. and J. T. Fasullo, 2010: Simulation of present-day and twenty-first-century energy budgets of the southern oceans. *J. Climate*, **23**, 440–454, doi:10.1177/0309133315620999.

Trenberth, K. E. et al., 2007: *Climate change 2007: The physical science basis. Contribution of working group I to the fourth assessment report of the intergovernmental panel on climate change*, chap. Observations: Surface and atmospheric climate change. Cambridge University Press, Cambridge, United Kingdom and New York, NY, USA.

Vallis, G. K., 1982: A statistiacal-dynamical climate model with a simple hydrology cycle. *Tellus*, **34**, 211–227.

Van den Dool, H. M., 1980: On the role of cloud amount in an energy balance model of the earth's climate. *J. Atmos. Sci.*, **37**, 939–946.

Vavrus, S., 2004: The impact of cloud feedbacks on arctic climate under greenhouse forcing. *J. Climate*, **17**, 603–615.

Wagner, J. W. and I. Eisenman, 2015: How climate model complexity influences sea ice stability. *Journal of Climate*, **28**, 3998–4014.

Weare, B. C. and F. M. Snell, 1974: A diffusive thin cloud atmospheric structure as a feedback mechanism in global climatic modeling. *J. Atmos. Sci.*, 1,725–1,734.

Wigley, T. M. L., 1993: Balancing the carbon budget. implications for projections of future carbon dioxied concentration changes. *Tellus*, **45B**, 409–425.

Wigley, T. M. L. and S. C. B. Raper, 1987: Thermal expansion of sea water associated with global warming. *Nature*, **330**, 127–131.

Wigley, T. M. L. and S. C. B. Raper, 1992: Implications for climate and sea level of revised ipcc emissions scenarios. *Nature*, **357**, 293–300.

Wigley, T. M. L. and S. C. B. Raper, 2001: Interpretation of high projections for global-mean warming. *Science*, **293**, 451–454.

Wigley, T. M. L. et al., 2009: Uncertainties in climate stabilization. *Climatic Change*, **97**, 85–121.

Wild, M. et al., 2013: The global energy balance from a surface perspective. *Climated Dynamics*, **40**, 3107–3134.

Wild, M. et al., 2015: The energy balance over land and oceans: an assessment based on direct observations and cmip5 climate models. *Clim. Dyn.*, **44**, 3393–3429, doi:10.1007/s00382-014-2430-z.

Winton, M., 2006: Amplified arctic climate change: What does surface albedo feedback have to do with it? *Geophys. Res. Lett.*, **33**, 1725–1734.

Yang, E.-S. et al., 2008: First stage of antarctic ozone recovery. *J. Geophys. Res.*, **113**, D20 308, doi:10.1029/2007JD009675.

Zelinka, M. D. et al., 2017: Clearing clouds of uncertainty. *Nature Climate Change*, **7**, 674–678, doi:10.1038/nclimate3402.